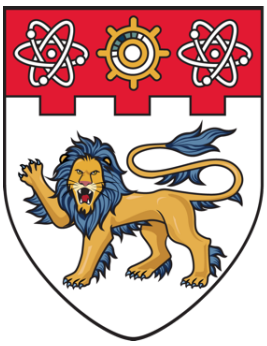

NANYANG TECHNOLOGICAL UNIVERSITY
SINGAPORE

MICROMACHINED TUNABLE DIFFRACTION GRATING FOR DIVERSE IMAGING IN INTEGRAL FIELD SPECTROSCOPY

MUTTIKULANGARA SWAMINATHAN SANATHANAN

SCHOOL OF MECHANICAL AND AEROSPACE ENGINEERING

2019

MICROMACHINED TUNABLE DIFFRACTION GRATING FOR DIVERSE IMAGING IN INTEGRAL FIELD SPECTROSCOPY

MUTTIKULANGARA SWAMINATHAN SANATHANAN

School of Mechanical and Aerospace Engineering

A thesis submitted to the Nanyang Technological University in partial fulfillment of the requirement for the degree of Doctor of Philosophy

2019

Abstract

This report presents the design and development of micro-optical components for a computational imaging spectrometer. The main elements that were involved in the optical design include a microlens array that samples the spatial information and a diffraction grating that provides spectral information. One of the significant drawbacks of scanning based imaging systems is the low light collection efficiency. The new technique proposed in this study used a quasi-snapshot technology that significantly improves the optical throughput. In a quasi-snapshot system, multiple images are captured with the optical system that can tune its optical transfer function (OTF). In this work, tunable micro-optics were investigated for the realization of the OTF modulation.

In snapshot imaging spectrometers, there is a trade-off between spatial sampling (x, y) and the measured wavelength band $(\Delta\lambda)$. This system attempted to overcome this trade-off by using computational methods and measurement diversity. In this technology, a microlens array was tightly packed to improve the spatial resolution. The close packing of the microlens array resulted in cross-talk of spectral information between the neighboring spatial pixels in the image sensor. An inverse algorithm was employed to retrieve the spectral information of the corresponding spatially separated microlenses. Optical diversity was incorporated using

dispersive tuning elements, such as diffraction grating, diffractive optical element, or prism. Multishot images were captured by tuning, which changes the OTF enabling to obtain spectral-spatial data with a small image sensor.

Optical simulations were carried out using ray tracing for a set of wavelengths, obtaining a multiplexed spatial-spectral image. The architecture allowed mixing of the spectral data with the neighboring microlenses, dramatically improved camera pixel utilization. By appropriate mixing and prior knowledge of the signal, information can be extracted. The output of the optical image captured by tuning the diffraction grating changes the mixing that allows measurement diversity.

Tuning the diffraction grating by modulating the pitch was realized using microelectromechanical systems (MEMS) technology. The tuning of the pitch was designed and modeled by MEMS comb drive based electrostatic actuation with silicon beams as the grating grooves. Tuning introduces an angular dependent shift in the dispersion based on diffraction relation. Both, theoretical and finite element method analyses were carried out for the mechanical mass-spring design of the suspended grating structure. The device was fabricated using surface micromachining technology on an silicon-on-insulator (SOI) wafer. The expected performance of the device was compared with the tested results to investigate fabrication tolerance and feasibility. Optical experiments were carried out to observe the shift in diffraction angle with electrostatic actuation. Further, a reliability study was conducted on the device by subjecting it to mechanical vibrations.

An alternative approach of tuning the diffraction grating is by rotation, and was implemented by MEMS technology. The rotation of the diffraction grating introduces changes to the direction of dispersion. To improve the optical perfor-

mance, the rotary actuator and the diffraction grating were fabricated separately. The rotary actuator was realized by SOI technology, and the actuation through electrostatic three-phase stepper motor principle. The rotating actuator works with the move and hold mechanism that allows precise angular movement with high repeatability. The stepping motion mechanism allows the device to work in a non-resonant mode, that benefits the usage of conventional cameras such as CCD/CMOS, where the frame capture speed is limited. Diffraction gratings were fabricated using negative photoresist, SU-8 by replication technique allowed realization of a blazed angle profile, resulted in high diffraction efficiency. Finally, the technology for bonding the replicated diffraction grating onto the electrostatic stepper motor using UV curable glue was proposed.

The multishot imaging technique is a middle ground between scanning technology and snapshot imaging, preserving the advantage of light collection efficiency. The tunable diffraction gratings to implement diversity of optical transfer function in imaging systems opened a new pathway to carve full fledge use of MEMS devices with optics than the traditional scanning based systems.

This page is intentionally left blank.

Acknowledgements

I am much indebted to my Ph.D. supervisor Professor Miao Jianmin for motivating me to explore the fascinating field of microelectromechanical systems (MEMS) to develop new ideas and to implement them. I am grateful to him for his guidance throughout this work and resolving the issues related to the fabrication of microdevices. I am indeed obliged to him for giving me the opportunity to work on this exciting project. I am sure that the way he groomed me during the tenure of my Ph.D. time would help me overcome adverse situations in professional and personal life in the future.

I express my sincere gratitude to my mentor, Dr. Maciej Baranski, who helped me in each and every discussion. His expertise in MEMS and optics had helped in minimizing the errors during the fabrication and conducting experiments. His valuable suggestions made me work harder and gave the confidence to travel in the unexplored path. I have learnt a lot from him during the past three years. His attitude of getting excited when getting strange or negative results helped to move forward to find out the reasoning, rather than getting distressed. I am grateful to him for his care and support.

I am also thankful to Professor George Barbastathis for introducing me to the exciting area of optics. His valuable bits of advice and the regular meetings with

him were an indispensable contribution to this project. I am grateful to him for allowing me to use the lab space in BioSystems and Micromechanics (BioSyM) - Interdisciplinary Research Group (IRG) at Singapore MIT Alliance for Research and Technology (SMART) for the entire duration of the project and beyond that. I was benefited by this, as it minimized a lot of time in building the optical system as it helped in the timely completion of the project.

I would like to thank all my colleagues from Micromachines Lab for sparing a great time all throughout my journey, for their outstanding support. I express my heartfelt gratitude to Dr. Ajay Kottapalli, Elgar Kanhere, and Dr. Wang Nan for their continuous encouragement throughout this journey. I had a great time with you all for the past three years which I will always cherish in my lifetime. I would like to thank Dr. Tao Kai, Dr. Hu Liangxing, Hooi Chee Quen and Rahul Singh for providing a friendly working atmosphere.

I also thank SMART colleagues for spending their valuable time for discussions. I am indebted to Dr. Sharon Ong who spared a lot of time helping me with MEMS integration when I was nearing the deadline for submission of my thesis. Immense gratitude to Dr. Meghali Bora who lent her ears whenever I was down. I extend my gratitude to Dr. Shakil Rehman and Dr. Shubin Li for helping in building optical testing systems. I am indebted to Dr. Krishna Agarwal, Dr. Kalpesh Mehta, Dr. Zhengyun Zhang, Dr. Hoang Xuan, Dr. Wei-Na, Dr. Wensheng Chen and Dr. Chen Zhi for the weekly discussions.

I must also acknowledge my Thesis Advisory Committee members Prof. Zhong Zhaowei, Prof. Zheng Yuanjin and Prof. Low Kay Soon for the healthy and constructive comments. I would like to thank Prof. Holden Li, my examiner for

the qualifying examination, who provided a lot of suggestions in my report, which I believe, have significantly improved the quality of my writings. I would also like to thank Economic Development Board (EDB) Singapore (Grant No: S14-1129-NRF-OSTIn-SRP) and National Research Foundation Singapore (NRF) for funding and supporting this research, without which I would not have been here.

Further, I thank all the technical staff members of Micromachines Lab, Mr. Pek Soo Siong, Mr. Nordin Bin Abdul Kassim, and Mr. Hoong Sinpoh for helping me in the fabrication process. I am thankful to Mr. Cheo Hock Leong of Micro-Systems Laboratory for providing space for MEMS device testing. I also thank Mr. Leong Tuck Weng of Computer Aided Engineering Laboratory for helping in releasing licenses of simulation softwares whenever I was in dire need. I owe my sincere gratitude to Manoj Kumar Chandra Mohan in Temasek Lab, Nanyang Technological University for extending the period of return of the supercritical CO_2 drying equipment till my Ph.D. completion. I also express my sincere thanks to Mr. Ang Kian Siong for considering the request for the extension of CO_2 dryer usage.

I would like to express my sincere compassion to my beloved friend Priyanka Valloly from Indian Institute of Science, who has always been the solace of my life. Tons of gratitude for spending time with me, as without you, this journey would have been impossible. I owe my friends, Anjaly Rajendran from GlobalFoundries and Dr. Aditya Anantharaman for their extensive patience, reading each and every line of my thesis, providing constructive suggestions.

I am conveying my acknowledgment to the open software community for the tools that helped me in my research. Special thanks to the LaTeXdevelopers for the

preparation of presentations, articles, and thesis; Python package distribution especially numpy, mathplotlib; Mendeley for reference managing; Inkscape for vector graphics editor; KLayout for mask designing; and Fiji-ImageJ for image processing and analysis.

I would also like to thank all others, whose direct or indirect help has benefited me during my stay at Nanyang Technological University. I express my gratitude towards all those unseen and unknown people associated with the internet, and the plethora of technical websites, forums, groups and mailing lists which have helped me with study material for my research work. Last but not the least, I would like to thank my parents and family members for their eternal love and extensive support all throughout my career.

Contents

List of Tables

List of Figures

This page is intentionally left blank.

Chapter 1

Introduction

1.1 Background

The determination of physical properties and chemical composition of a substance based on non-contact measurements is of great importance in the scientific community. Spectroscopy is found to be the most successful non-destructive method to study the properties of a substance without being into physical contact. Spectroscopy is the study of light-matter interaction of electromagnetic radiation with the substance to give absorption or emission spectra depending on the optical configuration [1]. It provides the most accurate, reliable and fastest measurement schemes for obtaining material properties.

A spectrometer measures the wavelength distribution of light emitted or reflected from an object for determining different analytes. In general, the spectral content of light scattered from an object has two-dimensional spatial variation. An extension to a point spectrometer is the imaging spectrometer, where the spectral information is measured for a two-dimensional (2D) image, *i.e.* spectroscopy in

imaging mode. Hence, an imaging spectrometer measures spectral distribution within the 2D image of the scene. It measures light intensity in three dimensions: two spatial dimensions (x, y) and a spectral dimension (λ), commonly referred to as the datacube, $I(x, y, \lambda)$ [2]. One of the examples is the commercial R-G-B camera, which measures three spectra (red, green, and blue) of the 2D scene. The three channel spectral information is obtained by separating out the incoming light by means of an array of band pass filters called Bayer's filter [3]. To expand the spectral channels, the most intuitive way is to increase the number of band pass filters on the image sensors. In this regard, each pixel in the sensor is associated with only a single spectral filter. The increase in spectral filters ultimately results in the reduction of spatial resolution. Further, spectral filters block a majority of the incoming light, making it a light inefficient system.

The most commonly used imaging spectrometers use scanning to capture the 3D datacube. The most straightforward scanning approach is the so-called whisk broom scanner, in which the 2D image is raster scanned point-by-point, and the spectrum is captured on a line detector. Another type of scanning is called push broom scanning, that contains a 2D image sensor allowing simultaneous measurement of one spatial dimension of the scene together with spectral information. A third category of scanning systems uses a spectral scanner that sequentially captures 2D images for the desired wavelengths using a tunable spectral filter (such as tunable Fabry-Perot filter) [4]. Another measurement scheme of capturing the datacube is the snapshot technology. Snapshot technology has a notable unique advantage in terms of light efficiency. It does not involve any scanning, and the complete datacube is measured in a single shot. In scanning systems, a majority

of the light is blocked either by the entrance slit (in whisk broom & push broom scanners) or by the spectral filter (in spectral scanner), whereas in the snapshot technique, there is no blockage of incoming light, thus making it a highly light-efficient system.

1.2 Motivation

The distinctive advantage of the snapshot technology of having a high light collection efficiency makes it superior over scanning mechanisms. In addition to that, images do not get affected by motion artifacts, since the image is captured in a single shot. However, the downside of this technique is that the image sensor has to be big enough to capture the complete information at once. Therefore, this technology always has a trade-off between the spectral and spatial information band to consolidate complete information onto the image sensor. In most of the snapshot spectroscopic systems, the number of voxels (elements in the datacube) are set less than the camera pixels to guarantee that spectral information of the individual spatially sampled objects are well separated from each other. It often results in many unused pixels in image sensor. The need for a large detector or sensing camera to accommodate all voxels is one of the main drawbacks of the snapshot technology, despite its distinctive advantages. To the best of knowledge, not much work has been reported to overcome this trade-off. Hence, there is plenty of room to explore for improving the spectral-spatial resolution without employing a big detector. One such possibility is the use of compressive measurements schemes with computational method of analysis.

The computational method of retrieving the object is based on numerical inver-

sion of the indirect measurement and prior information about the observed object. However, in most cases, it is very difficult to compute the exact transfer function, of the optical system due to the aberrations of the lenses. Image retrieval becomes more complex when the signal gets affected by noise. An analogy for this problem is fading in wireless communication systems, where the transmitted signals get distorted at the output [5]. Multipath propagation of the signal makes the data recovery even more complex, as the same signal reaches the output at different instants of time. In case of communication systems, prediction of properties of the channel is difficult, since the transmitting and the receiving systems don't have access to change or modify the properties of the channel. Several data handling/channel assignment schemes are adopted on the transmitter and receiver sides, to retrieve the original information from the signals that are mixed with noise [6].

Diversity techniques are the most commonly used method in standard radio communication systems to overcome the distortions that are caused due to the complexity in channel [7, 8]. The idea of diversity is to transmit the signal in multiple channels instead of a single channel. Hence, each channel experience different kinds of fading. Based on the set of received outputs, most likelihood estimate of the transmitted signal can be calculated. A similar approach can be employed in imaging spectroscopic systems for efficient image reconstruction. It could be achieved by capturing multiple measurements (quasi-snapshot technology) instead of taking a single measurement. One of the techniques in optics is capturing multiple defocused images by positioning the camera at different locations and later processed them using recovery algorithms [9, 10]. Another approach for imple-

menting diversity could be by tuning the optical elements of the architecture.

The use of MEMS technology for tunable optics seems to be promising for such applications because of its highly precise fabrication capabilities. MEMS technology has already been proven successful and well established in scanning based exclusive imaging spectrometers [11, 12]. A drawback of such scanning based devices is its limited tuning range. Hence, tunable optical MEMS fits well for diversity implementation in quasi-snapshot systems. No significant work has been reported in the past with tunable optical MEMS devices for multishot imaging systems. It is worth exploring the possibility of use of MEMS devices for such systems, where tuning of the optical element produces a significant change in the optical transfer function. Hence, considering the aim, a tunable optical device based on MEMS technology is expected to meet the desired performance for such dedicated instruments.

1.3 Objectives

Following are the main objectives expected to be achieved from this project:

1. The first aim is to come up with an optical design and subsequent realization of a highly light efficient imaging spectrometer. It can be attained by either snapshot technology or quasi-snapshot imaging systems.

2. Most of the snapshot imaging spectroscopic images have non-overlapping spectral data because of the low spatial pixels. This leads to poor camera utilization, since most parts of the image sensors are unused. One of the aims in designing the optical configuration is to improve the spatial resolution by

allowing overlapping of signals on the image sensors for effective pixel utilization, which has to be later unmixed by post processing (*i.e.* computational techniques).

3. The hyperspectral dataset (datacube) obtained by the snapshot imaging spectrometer measures spectral irradiance present in the object or scene. The data handling costs will be a challenge when the resolution is critical and high. Hence, technology of compressive measurements might be advantageous in data handling, that needs to be addressed.

4. Diverse measurement enhances the information content within the system, which is beneficial for compressive measurement systems. More information is helpful in obtaining the closest approximation of the object. Hence, it is important to explore the possible ways of achieving diverse measurement schemes in the dedicated optical systems, which would be useful in image retrieval.

5. To investigate the possibilities of employing MEMS technology with optics for optical transfer function diversity implementation. It would allow batch fabrication of low cost miniaturized spectral imaging systems.

6. Development of tunable optical systems involving their design, fabrication, characterization, testing, and performance analysis.

7. Most of the optical elements such as the diffraction grating, fabricated by standard micromachining technology, have relatively low efficiencies due to the limitations in obtaining the desired shape profile. To surpass this, the possibilities of integrating the MEMS device with micro-optical elements are

also need to be investigated.

1.4 Scope: MEMS for imaging spectroscopy

Imaging spectrometry is the methodology that adds imaging capability to spectroscopy. Initially, most of the instruments were installed in satellites or airborne instruments to study the properties of the earth's surface [13] for pollution monitoring [14, 15]. It has important roles in applications such as vegetation [16, 17], agriculture [18], food quality control [19, 20] and oil spill detection [21]. Recently it has become more prevalent in biomedical applications [22] such as ophthalmology [23], and cancer detection [24, 25].

Many researchers have reported successful demonstration of MEMS devices on miniaturized spectrometers [26, 27, 28]. A few MEMS devices were used in spectral scanning covering VIS-NIR wavelengths, in single detector spectroscopy [29, 30]. MEMS devices installed in these spectrometers were designed for either spatial or spectral scanning. As discussed, since scanning based systems have low optical throughput, technology is moving towards snapshot based systems to improve light efficiency. Technology shifted its direction for realizing high resolution scientific grade cameras to incorporate maximum voxels [31, 32]. However, such image sensors are quite expensive.

A middle ground between snapshot and scanning based systems could be a quasi-snapshot technology (or multishot image acquisition) preserving the advantage of being light efficient with small image sensors. The compressive measurement scheme adds the additional benefit of gathering voxels that are larger than the sensor size [33]. For such multishot systems, MEMS devices would be interest-

ing for taking multiple measurements by varying the optical transfer function of the architecture.

1.5 Thesis organization

The thesis is organized into six chapters. Chapter 1 describes the background and motivation of conducting this research. It also details the aim, the outcome that is expected, and it also describes road maps towards project completion.

Chapter 2 reports a relevant literature survey. It describes about classical spectroscopic systems in brief. Then it discusses imaging spectroscopy and their classifications, with an overview of different types of scanning mechanisms to construct the datacube. Further, it is followed by a review of basic inverse problems for image retrieval. Additionally, a detailed report of MEMS based tunable diffraction gratings and rotational actuation mechanisms researched in the past are summarized.

Chapter 3 describes the theoretical modeling of a few optical architectures for integral field spectroscopy based on geometrical optics, using ABCD-EF formalism. Further, an optical ray tracing simulation is carried out for an image using ZEMAX non paraxial software to simulate 3D datacube imaging. This chapter also briefly discusses spectral reconstruction from the overlapped image using computational methods. Further, the influence of tuning the optical element is investigated for implementing optical transfer function diversity for quasi-snapshot imaging systems.

In Chapter 4, an electrostatic actuation based pitch tunable diffraction grating is designed and implemented on a silicon-on-insulator wafer. It includes a com-

prehensive modeling procedure of electrostatic comb-drive based tuning. Detailed fabrication steps followed by characterization and testing are presented.

Chapter 5 discuses the tuning of the diffraction grating employing rotation. It further discusses the fabrication of the electrostatic micro actuator and the polymer diffraction grating, and their complete characterization. Finally, the technological development scheme for integrating the actuator with the polymer optical element is investigated experimentally.

Chapter 6 concludes the report with the summary highlighting the major contributions. It also discusses future perspectives for extension of this work.

Chapter 2

Literature survey

2.1 Spectroscopy

Optical spectroscopy is a means of studying the properties of a material based on how it interacts with electromagnetic radiation. It provides both, quantitative and qualitative pieces of information about the atomic or molecular composition present inside the sample [34]. Properties such as chemical composition and concentration are obtained by observing either transmission or absorption spectra. This is possible due to the change associated with the electrons energy levels when the sample interacts with light. In case of monoatomic substances, interaction with electromagnetic radiation results in transition change from ground state to excited state in the form of discrete energy states called quanta [35]. The molecular interaction with electromagnetic radiation is based on the difference in energy level associated with electronic transitions, vibrations, and rotations [36].

Spectroscopy is a successful tool that provides fast measurements without being physically in contact with the sample. Spectroscopy is therefore used in applica-

tions ranging from remote sensing to microbial identification. The instrument that performs spectroscopy is called a spectrometer. In general, a spectrometer can be divided into three sections: source, filter, and detector. A basic schematic of a spectrometer is depicted in figure 2.1. The light emerging from the source is

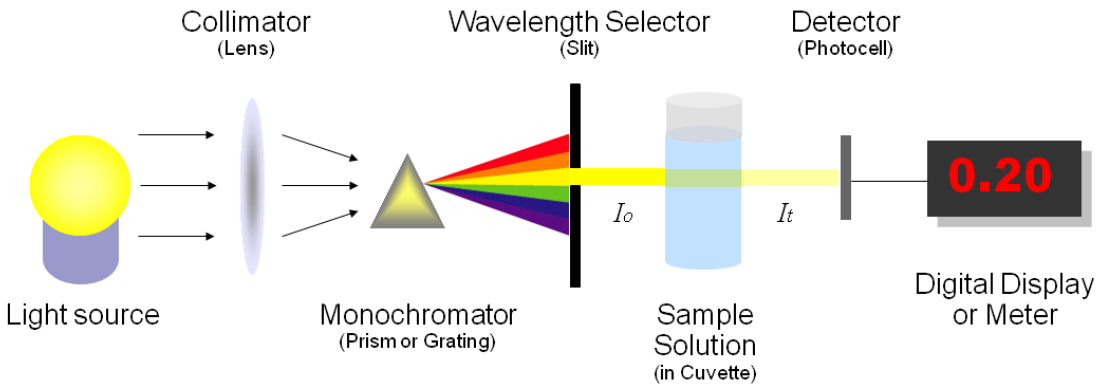

Figure 2.1: Schematic design of a simple spectrometer [37].

passed through the filter, and projected on the detector through the sample under test, to gather information. The filter can either be a prism, a diffraction grating, a holographic elements or any diffractive optical elements that can disperse the broadband light source into its individual wavelengths. The energy level change in the electromagnetic spectrum after interaction with the sample is manifested at the detector output.

2.2 Imaging spectroscopy

Imaging spectroscopy is spectroscopy in imaging mode. The objective of an imaging spectrometer is to obtain spectrum for each spatial pixel of 2D image. The data capture forms the datacube with two space dimensions and the 3^{rd} dimension corresponding to wavelength. This results in 3D datacube representing irradiance

of the sample that takes the form $I(x, y, \lambda)$.

Imaging spectrometers can be categorized based on the number of bands as well as the regions of interest. Initially, most of the imaging spectrometers were installed in imaging satellites and airborne instruments to measure the properties of the atmosphere, land, and water beneath. A schematic representation of the imaging spectrometer to capture a 3D dataset, $I(x, y, \lambda)$ is depicted in figure 2.2.

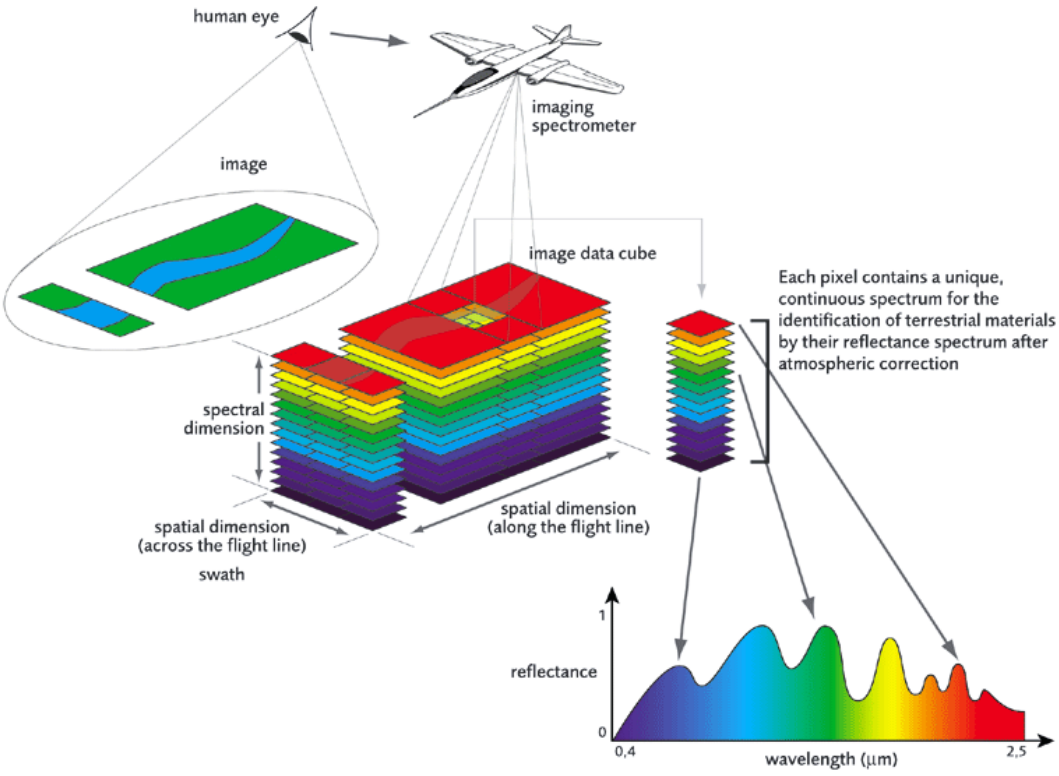

Figure 2.2: Schematic representation of imaging spectrometer capturing 3D information [38].

The first model of the imaging spectrometer was developed by Goetz *et al.* consisting of 192 spectral bands in the 0.4 µm to 2.5 µm wavelength range [39]. It could identify earth's surface features such as rock, soils, vegetations, and suspended particles in water.

The imaging spectrometer is also successful in measuring atmospheric pollutant gas concentrations by making use of unique spectral signatures of gases (figure 2.3). The earliest pollution monitoring instrument installed in the satellite was the

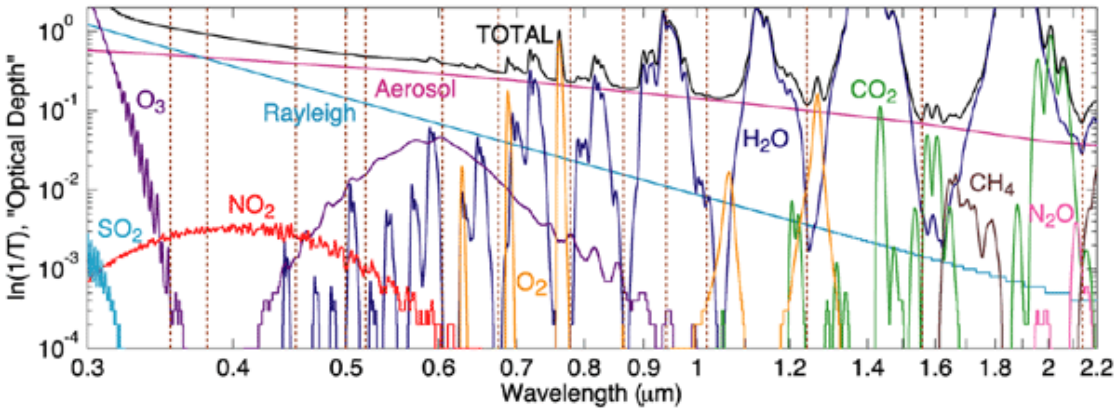

Figure 2.3: Spectrum of atmospheric gases measured by Ames Airborne Tracking Sunphotometer (AATS)-14 [40].

Total Ozone Mapping Spectrometer (TOMS), which was used to measure the ozone column along with the global dust distribution present in the earth's atmosphere [41, 42].

In 1995, the European Space Agency (ESA) launched the second European Remote Sensing Satellite (ERS-2) with a new instrument for pollution monitoring, containing the spectrometer, Global Ozone Monitoring Experiment (GOME). GOME measures the sunlight reflected and scattered from the earth's atmosphere to measure the trace gas responsible for ozone formation. GOME provides vertical distribution of gas concentarions in the visible (VIS) and ultraviolet (UV) wavelength spectrum ranging from 240 nm to 790 nm [43]. GOME has a ground spatial resolution of $40 \times 320\,\mathrm{km}^2$ and a spectral resolution between 0.2 nm to 0.4 nm. To measure this broad spectral range with sub-nanometer resolution, GOME splits light into four spectral bands and measures using four separate channels. After

analyzing the measured spectrum, concentrations in vertical column distributions of NO_x were extracted using differential optical absorption spectroscopy (DOAS) techniques [44].

ESA launched the ENVISAT satellite with the Scanning Imaging Absorption Spectrometer for Atmosphere CHartographY (SCIAMACHY) as atmospheric chemistry payload [45]. The SCIAMACHY also carries out measurements like GOME using DOAS techniques with the spectrum extended to NIR (near-infrared) region. The spectrometer has a spatial resolution of $30 \times 15\,\mathrm{km}^2$ measuring the sunlight transmitted, reflected and scattered by the earth surface. It contains eight spectral channels for wavelengths from 240 nm to 2380 nm with a spectral resolution varying from 0.2 nm to 1.5 nm.

A modern instrument is the Ozone Monitoring Instrument (OMI) flown on the Aura spacecraft on July 15, 2004, as part of NASA's long-term earth observing systems (EOS) mission. GOME and SCIAMACHY can measure the complete spectrum in the UV/VIS/NIR range with high resolution, and with TOMS algorithm, a spatial resolution of $50 \times 50\,\mathrm{km}^2$ can be measured. OMI combines the idea behind GOME and SCIAMACHY to obtain high spectral resolution and uses the TOMS algorithm to achieve high spatial resolution. Thus, OMI measures spectral information in the UV/VIS region with a spatial resolution of $13 \times 24\,\mathrm{km}^2$, providing daily global coverage. The NO_2 concentration map of south-east Asia provided by OMI in May 2015, is shown in figure 2.4. The latest instrument is the TROPOspheric Monitoring Instrument (TROPOMI), successor of OMI, that extend its capability providing better spatial resolution of $7 \times 7\,\mathrm{km}^2$.

In general, all these large-scale instruments installed on satellites are costly

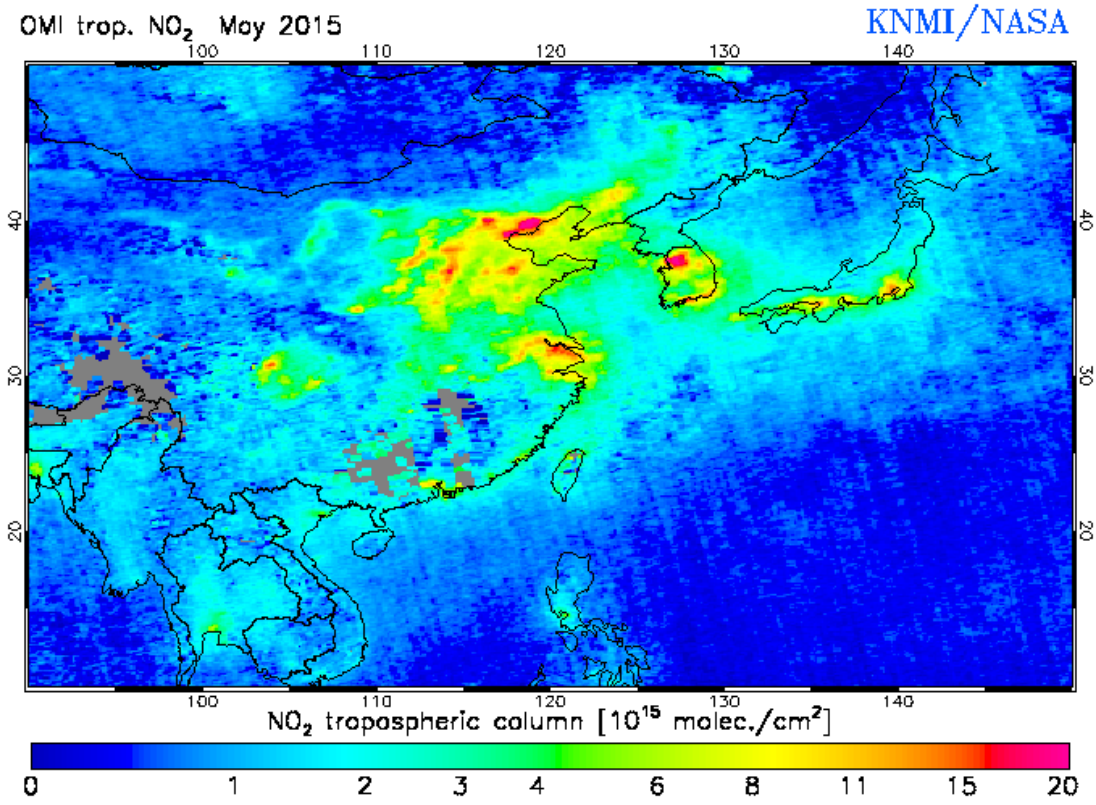

Figure 2.4: NO_2 concentration map of South East Asia provided by OMI in May 2015 [46].

and are designed to provide global measurements, which would make it difficult to quantify the fine details of small countries like Singapore. In other words, these instruments have low spatial resolution even though they provides ultra fine spectral resolution from the UV to IR bands. Improving the spatial resolution in the imaging spectrometer is of great interest for monitoring transboundary pollution so that it can be easily installed in airborne vehicles. This brings out the necessity of a dedicated spectrometer for local coverage with low cost and miniaturized design so that it can widen its applications further.

With the intuitive approach for improving spatial resolution by taking into consideration small footprint low cost systems, imaging spectroscopy expanded its usage in medical imaging [47], food quality control [48, 49, 50, 51], oil leakage [52],

archeological art for pigment determination [53], military target detection [54], and many other applications [55].

2.2.1 MEMS technology in imaging spectrometer

Integration of microelectromechanical systems (MEMS) devices with optics have always been appealing in the spectrometer designs. One of the attempts was with a deformable MEMS grating to effectively scan the desired wavelength of interest. Sagberg *et al.* [56] used a large number of rectangular ribbons with gratings inscribed on the individual strips. The grating was used as a configurable diffractive filter and also as a fast scanning monochromator.

MEMS technology is also used in imaging systems as a spectral scanner. Imaging spectrometer developed by Egloff *et al.* [57] used a micro-opto-electromechanical system (MOEMS) scanning mirror with grating inscribed in it to capture the spectral information in the near infrared region (NIR) regime. The device was capable of obtaining a hyperspectral image in the NIR. It senses a spectral range from 780 nm to 2500 nm with a resolution up to 20 nm to obtain spectral signatures of OH, NH and CH radicals present in the compounds.

The most recent micro-spectrometer developed by VTT Technical Research Centre of Finland, used MEMS Fabry-Perot interferometer (FPI) technology for building a spectrometer and deployed it in the Aalto-1 satellite [58]. The device consists of a tunable filter, where the spacing between the plate was adjusted to acquire the desired wavelength [59]. This dedicated spectrometer was designed to monitor the atmosphere surface covering wavelengths from 400 nm to 1000 nm with a maximum resolution (full-width-half-maximum) of 10 nm.

2.2.2 Scanning mechanisms

The imaging spectrometer has to measure intensity distribution as a function of the region of interest and the wavelength, *i.e.* $I(x, y, \lambda)$ of the scene consisting of $N_x \times N_y \times N_\lambda$ voxels. Imaging spectrometers can be categorized based on the readout scheme adopted on the detector. The measurement scheme is described in the following sections distinguishing their pros and cons related to its light collection efficiency and resolution.

2.2.2.1 Whisk broom scanning

This method is also called point scanning or pixel scanning, where a 2D scene (x, y) is scanned by a point-by-point method (raster scanning). The light coming from each point is dispersed out using either a grating or a prism, and projected onto a linear detector to acquire the desired spectrum. The complete datacube is measured by moving either the object or the optics in the spatial domain (x, y) to cover the complete scene. The light collection efficiency of this scheme is poor, since the system measures only N_λ voxels at an instant. The remaining voxels are blocked by the optical filters in the architecture resulting in a light efficiency drop factor of $1/\left(N_x N_y\right)$.

2.2.2.2 Push broom scanning

Push broom or line scanning is similar to whisk broom scanning, where instead of point scanning, the object is scanned line by line and information is captured on a 2D image sensor $N_x \times N_\lambda$. Here, the detector arrays are aligned perpendicularly to the scanning direction measuring the spectrum of each point of the line. Push

broom and whisk broom scanning have a relatively larger spectral resolution. In terms of light collection efficiency, it has advantage over point scanning; here the light efficiency drop factor is $1/N_y$.

2.2.2.3 Staring

Staring is also called sequential band method, in which only spectral scanning is adopted. Here, a 2D gray scale image is captured for desired set of wavelengths $I_{\lambda_k}(x, y)$. Spectral scanning can be achieved by different methods such as Fabry-Perot interferometer (FPI) [60], acousto-optic tunable filter (AOTF) [61], liquid-crystal tunable filter (LCTF) [62], linear variable filters (LVF), variance interference filter (VIF) etc. This method allows the flexibility to choose the desired wavelength. Principally, the spectral scanning is a function of time *i.e.* at a specific time instant, an image reveals the details of a particular wavelength. The number of voxels measured at an instant is $(N_x \times N_y)$. Hence, for such systems, the efficiency drop factor is $1/N_\lambda$.

2.2.2.4 Snapshot imaging

Single shot acquisition or snapshot imaging doesn't involve scanning. This method directly captures both, the spatial and the spectral information, simultaneously. The main advantage of such a data acquisition scheme is the light collection capacity, since all voxels $(N_x \times N_y \times N_\lambda)$ are collected at once without blockage of light. Such systems have excellent temporal resolution, which avoids motion artifacts in the image quality. Hence, it is mostly suited for a time-varying object/scene. However, for capturing this large data set, there is always a trade-off between spectral and spatial resolution. In other words, the number of voxels to be measured is lim-

ited by the number of camera pixels. The working principles of the four different categories of imaging spectrometers are depicted pictorially in figure 2.5.

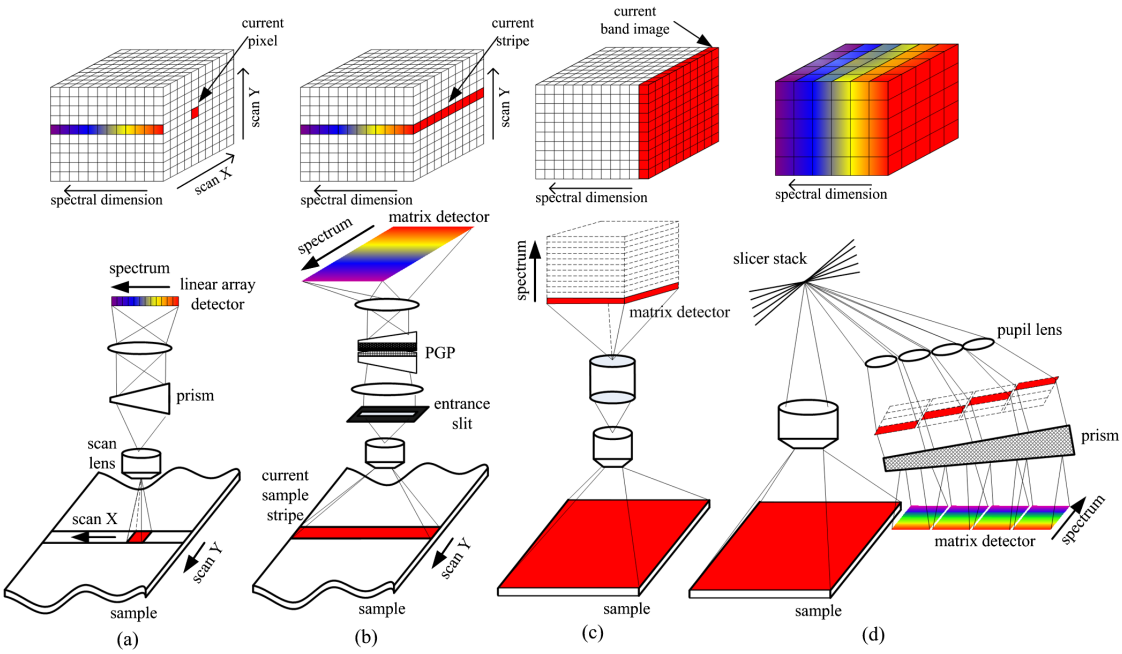

Figure 2.5: Data acquisition schemes adopted in spectrometers to obtain hyperspectral datacube [63]: (a) whisk broom scanning, (b) push broom scanning, (c) staring, and (d) snapshot imaging.

2.3 Integral field imaging

Integral field imaging (also known as light field imaging or Lippmann photography [64]) is a snapshot based system, and has recently become very popular with the advent of the commercial digital light-field camera by companies such as Lytro [65], Pelican Imaging [66], and Adobe [67]. The main idea of integral-field imaging is to place a lenslet array at the focal plane of the main lens. The CCD sensor chip is positioned at the focal plane of the microlenses. With such an arrangement, images that are not in focus can still be analyzed, thereby extracting the depth

information of the scene [68]. The light-field camera developed by Lytro, is able to refocus the image virtually on a computer after the picture is taken. This is achieved by a microlens array that captures the angular distribution of light. Thus, each camera pixel receives light from a narrow range of angles only from the spatial location specified by its corresponding lenslet. In other words, the image is both spatially and angularly resolved [69]. Finally, the image is retrieved by a computational method. This property can be used to build spectrometers to capture both spectral and spatial information with a single shot acquisition. C*ôté et al.* [70] have built a Fourier transform spectrometer with a light field camera by observing shear and tilt fringes.

Hence, light field computational imaging (or computational photography) combines optics with post-processing providing a new insight in gathering more information, thereby overcoming the traditional limitations of standard photography. It is a promising research area and can be expanded for object detection, depth information, motion sensing, etc. Unlike conventional imaging systems, here the raw images were taken and the angular data was processed to refocus the image.

2.4 Inverse problems in imaging

The inverse problem is an important part of a computational imaging system, when general information of a scene is gathered instead a direct image. Hence, the output image does not manifest the object or scene as in traditional imaging techniques. The forward model of the general linear optical system can be represented by

$$g = \mathcal{H}s + n \tag{2.1}$$

where, s is the input/object, $\mathcal{H}$ is forward operator, g is the measurement, and n is the noise. If $\mathcal{H}^{-1}$ exists, the signal can be calculated using simple algebraic inversion by:

$$\hat{s} = \mathcal{H}^{-1} g \tag{2.2}$$

However, in practical cases such inversion is often largely affected by noise present in the measurement leading to the erroneous signal inversions. One of the algorithms considering inversion instability due to additive noise is Wiener deconvolution, that can be applied if the optical system operator $\mathcal{H}$ represent a mathematical convolution operation.

2.4.1 Wiener deconvolution

Inverse filtering is not a good choice for signal retrieval as it is highly sensitive to additive noise. Wiener deconvolution is a better option for removing the additive noise, at the same time minimizing the mean square error. The Wiener deconvolution is performed by Eq. (2.3) [71]

$$\hat{s} = \mathcal{F}^{-1} \left\{ \frac{1}{\mathcal{H}_{(u,v)}} \left[\frac{|\mathcal{H}_{(u,v)}|^2}{|\mathcal{H}_{(u,v)}|^2 + \frac{1}{SNR}} \right] \mathcal{G}_{(u,v)} \right\} \tag{2.3}$$

where, $\hat{s}$ is the estimate of the input signal, $\mathcal{H}_{(u,v)}$ is the Fourier transform of the point spread function (PSF), $\mathcal{G}_{(u,v)}$ is the measured signal, and SNR is the Signal-to-Noise Ratio.

2.4.2 Tikhonov inversion

Tikhonov inversion is another method to estimate the signal based on the regularization principle [72]. The proposition is to minimize the energy difference between

the estimate and the measured data, represented by Eq. (2.4) [71]

$$\phi(s) = min\left\{||g - \mathcal{H}s||^2 + \alpha||s||^2\right\} \tag{2.4}$$

where, α is the regularization parameter. The basis is to obtain a solution for s by minimizing $\phi(s)$ with a suitable selection of the regularization parameter. However, as discussed, in all these systems, the resolution ultimately depends on the size of the PSF.

2.4.3 Compressive sensing

Compressive sensing or compressive sampling (CS) is a technique to extract signal information with a fewer number of samples, less than those given by the Nyquist sampling criteria [73]. The two principles: sparsity and incoherence are used in the theory of CS to retrieve data with fewer samples, that go against the conventional wisdom. This is because many naturally occurring images are sparse or compressible and they can be represented concisely when defined with a proper basis. Incoherence deals with the duality principle like frequency and time: the image that is sparse will have it dense form in the measured signal domain.

The crucial part of sensing is the design of a sampling protocol to capture useful information contained in the sparse signal and to compress it. CS is an efficient protocol, in which the signal can efficiently be computed with a slower rate and can be later efficiently reconstructed using a computational algorithm. Brady *et al.* [74] used compressive sensing to design spectrometers using coded aperture. A similar version of such a system was also developed for sparse objects by capturing multishot measurements [75]. Rice's single pixel camera used this technology to generate different code patterns, and captured the intensity by a

single pixel camera. With a set of code patterns, the image was reconstructed reasonably well [76]. An adequate reconstruction of the image from fewer samples depends on the code pattern and the invertible algorithm. The collection of light from the object (photon efficiency) in coded aperture would be sufficiently higher than the traditional single slit dispersive element. Using a similar technology, Wagadarikar *et al.* [77] captured scenes of two balls which were illuminated by two different light sources and extracted the spectral information with a 3.6 nm resolution.

However, in such systems, reconstruction fails if a sufficient numbers of measurements is not present. Signal reconstruction quality is proportional to the number of frames captured, which is not a good choice for a time varying object. Moreover, in such architectures, a good portion of light is blocked by the coded aperture, thus compromising the light collection efficiency. In this regard, the diversity technique could be a better choice to minimize the number of frames to be captured and at the same time to obtain more information.

In the next section, tunable dispersive elements realized by micro-fabrication techniques in past are discussed, which might be useful in diversity implementation in constructing a spectrometer. There were attempts to use MEMS technology in the imaging spectrometer, as described in section 2.2.1. With the introduction of tunability in optical elements for quasi-snapshot imaging systems, a more efficient estimate of the signal is expected.

2.5 Tunable dispersive elements

The most commonly used dispersive elements in spectrometers are diffraction grating, prism, and diffractive optical element (DOE) [78]. The aim of the dispersive element is to splits the white light to its individual components, and the tuning provides the selection of the desired wavelength. To introduce tuning in the dispersive elements, the diffraction grating was mostly chosen since it has been found to be relatively successful [79, 80] when compared with other elements. Commercially available diffraction gratings are defined by fixed lines/mm. Initially, such diffraction gratings were fabricated by highly precise ruling engines [81, 82]. Later it was moved to micromachining technology for batch production [83, 84].

Tunable diffraction grating also could be realized by micromachining technology. Such a device could be employed in spectrometers for separating the desired wavelength information. Highly precise MEMS fabrication techniques with the design incorporating actuation mechanisms, tunable diffraction gratings have become a reality. Tuning can be achieved by different methods such as varying the pitch, rotation, or by changing the index of the grating. The subsequent sections describe the means of attaining tuning and also discuss different actuation mechanism which could be employed for tuning diffraction gratings.

2.6 Tuning mechanisms for diffraction gratings

The ways of achieving tunability in diffraction gratings are listed as follows:

- Elastomeric microfluidic devices
- Dielectric elastomer actuation

- Piezoelectric driven actuation
- Grating light valve (GLV)
- Thermal actuation
- Electrostatic comb-drive actuation

2.6.1 Elastomeric microfluidic devices

The first model of tunability in a grating was demonstrated with microfluidic channels for phase gratings. Schueller *et al.* [85] fabricated a series of the periodic patterns of micro-channels on polydimethylsiloxane (PDMS). An array of micro-channel trenches was filled with fluids of a known refractive index. The difference in refractive index between the micro-beams and micro-channels forms the grating pattern. The phase of the light was modulated by changing the index of refraction of fluids. The device was developed with 20 parallel lines 50 µm wide, 20 µm thick and separated by 50 µm. The 2.5 cm long device was connected to reservoir pads, where flits were stored. The fabricated reconfigurable microfluidic-based phase diffractive grating is shown in figure 2.6.

The microfluidic channels can be filled with different types of fluids: if the liquid is transparent to the incident light, the device works as a phase grating. The phase variation is proportional to the thickness of the micro-channel and given by the Eq. (2.5) [85]:

$$\delta\phi = \frac{2\pi}{\lambda} d\Delta n \tag{2.5}$$

where, d is the thickness of the micro-channel, Δn is the difference in index of refraction between the device (here PDMS) and micro-fluid and λ is the incident

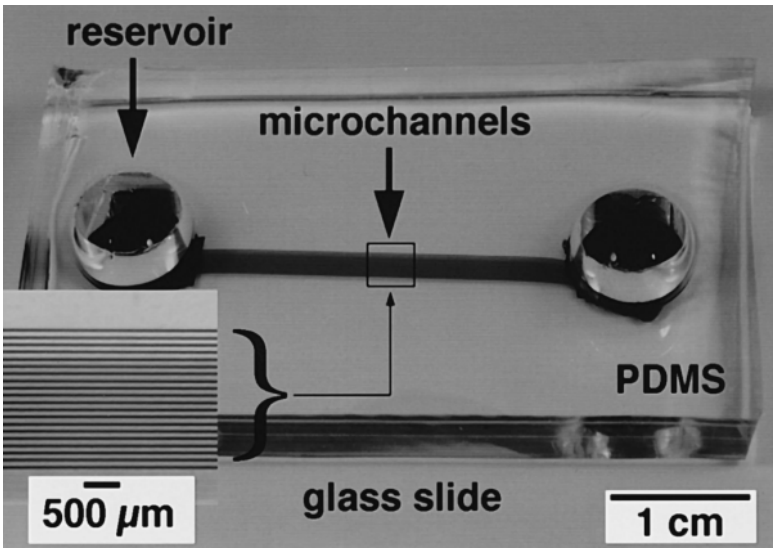

Figure 2.6: Reconfigurable microfluidic-based diffraction grating [85].

wavelength. Likewise, if the micro-channel is filled with a die-like substance that can absorb light, the device works as an amplitude grating.

The property of a changing diffraction angle with the variation of refractive index can be utilized to make the tunable grating work as a sensor. The switching time of the device (microfluidic channel filling time) was in the range of 50 ms, which can be further improved by scaling down the device dimensions.

2.6.2 Dielectric elastomer actuation

Another class of sinusoidal phase diffraction gratings is based on soft materials [86]. Aschwanden *et al.* used a dielectric elastomer with a carbon black electrode (CB) to generate strain for tuning. The device was developed by stretching a thin membrane of dielectric elastomer, which was then attached to a PMMA membrane. Further, a soft material, CB, was imprinted on top of the elastomer. A diffractive grating was replicated by PDMS with the master grating mold and was placed on top of the elastomer. PDMS molding process was carried out in a vacuum

chamber to avoid bubble formation between the layers. The fabrication method of the device is illustrated in figure 2.7. The application of voltage to the electrode

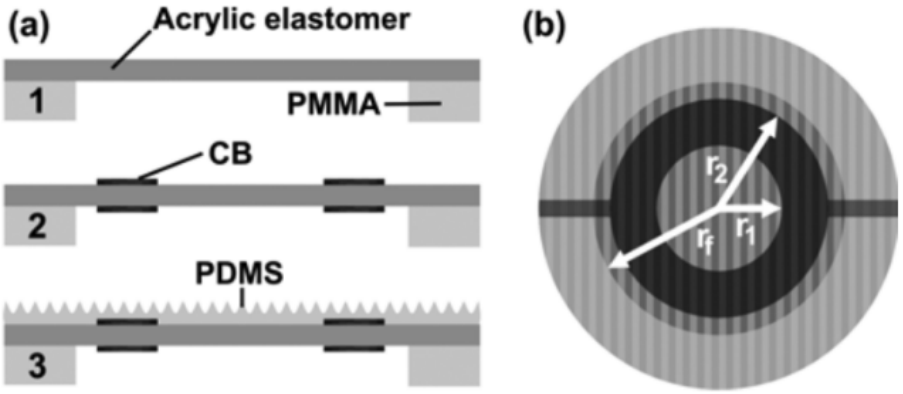

Figure 2.7: (a) Schematic of the set-up for the fabrication of the electrically tunable transmissive grating using acrylic elastomer actuator, (b) top-view of the device [87].

induces Maxwell stress resulting in the stretching of the electrode. This leads to compression in the middle-transmissive region, which varies the grating pitch. It resulted in a pitch change of 7.5 % with an actuation voltage of 4.5 kV. Compression of the grating that occurred by tuning, increased the height profile of the grating led to the enhancement in 1^{st} order diffraction efficiency by 6.4 %.

2.6.3 Piezoelectric microelectromechanical actuators

Piezoelectric membrane deforms its shape when a voltage is applied. Piezoelectric actuation is suitable most of the times when the device has to be actuated with nanometer precision. Wong *et al.* [88] fabricated a strain-tuned grating structure via MEMS technology utilizing both bulk and surface machining technology. The device consisted of a thin silicon membrane, developed with potassium hydroxide (KOH) wet etching, and the grating pattern was inscribed on the membrane by

patterning platinum metal. The piezoelectric material used in the developed device was lead zirconate titanate oxide (PZT), located at both ends of a thin diaphragm, thereby inducing strain in the diaphragm. The schematic of the device is depicted figure 2.8. It reported an actuation of 0.21 % in the membrane resulted in a grating

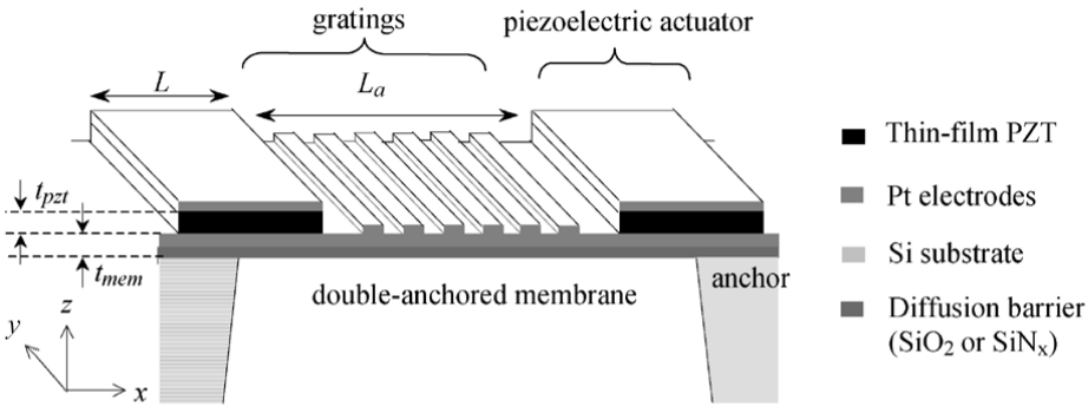

Figure 2.8: Schematic of the analog tunable amplitude diffraction grating actuated by piezoelectric mechanism [88].

pitch change of 8.3 nm for 10 V. This induces a change in the first order diffraction angle by 486 µrad [89].

2.6.4 Grating light valve

By mixing optics and MEMS (MOEMS), Senturia *et al.* [90] fabricated an electrically programmable grating light valve (GLV) for spectroscopic applications. The GLV has a set of reflective ribbons that were deflected by the application of voltage, causing the grating pitch to digitally vary by multiples of 2. Resolution on this device suffers, since fine tuning of pitch was not possible.

2.6.5 Thermal actuation

An efficient way of achieving large displacement is by thermal actuation. Yang *et al.* [91] reported a displacement of 300 µm by thermal actuation with an operating voltage of 19 V, thereby varying the pitch by 25 %. This is the highest reported actuation of a diffraction grating till date. However, the main drawback of this device is its low switching speed with the application of actuation voltage and low recovery time when the actuation is released.

2.6.6 Electrostatic comb-drive actuation

Shih *et al.* [92] fabricated an electrostatic comb-drive based analog tunable grating with a single mask offering the advantage of achieving good optical flatness and relative ease of fabrication. A schematic design of the fabricated device is shown in figure 2.9. The device has a grating pitch of 12 µm (6 µm width and 6 µm spacing)

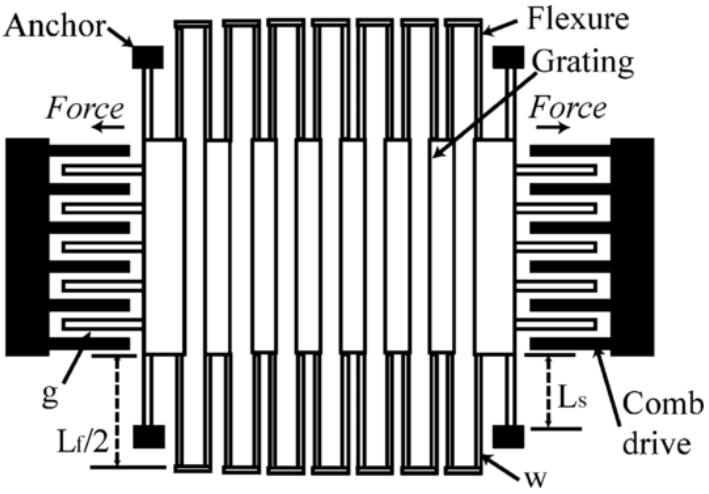

Figure 2.9: Schematic depicting the working principle of analog tunable amplitude diffraction grating [92].

with 17 grating beams. An experimental analysis reported comb-drive movement

of 0.459 µm, resulted in a pitch change of 57.4 nm, with an actuation voltage of 10 V. Yu *et al.* [93] extended this model to operate the device in both transmissive and reflective modes. The device was fabricated on a silicon membrane and bonded to a glass base using anodic bonding. To increase the dynamic range of the device, tilted supporting beams were used for actuation to attain larger displacement. The device was characterized via an optical method by capturing the diffracted light with a CCD camera. The pitch change in the grating induced a shift in the diffraction spot in the camera pixel. The pitch change of the structure was back-calculated by a trigonometric triangular relation.

In conclusion, based on the working feasibility, fabrication and integration, electrostatic comb-drive based actuation is the best choice for the considered application, due to its unique features such as low power consumption, relative ease in manufacturing, fast response and relatively broad actuation range. Another category of tuning diffraction grating is by rotation.

2.7 Rotational actuation

Magnetically coupled rotating motors are extensively studied in the area of mechanics at the macro level. However, as the devices shrink to micro dimensions, electrostatic control of motion profound over the magnetic actuator. The principle is based on the static electric charge developed between plates generating the electrostatic force. One such design is the comb drive fingers actuation employed in micromachining technology. The force generated due to the application of a voltage between the capacitive plates results in the generation of a mechanical force to nullify the effect of the electrostatic force.

Rotational based grating tuning is not widely prevalent in MEMS technology, which could either be due to its fabrication challenges, or due to its limited angular tuning range. The subsequent sections describe the rotational actuation schemes realized by previous research.

2.7.1 Rotation based on gear mechanism

A few research groups have worked on rotary motors based on gear systems at the micro-dimensions. Scanning electron microscope (SEM) images of some of the micro-motors fabricated by Sandia National Laboratories are depicted in figure 2.10. These types of micro motors work with contact gear mechanism. The ad-

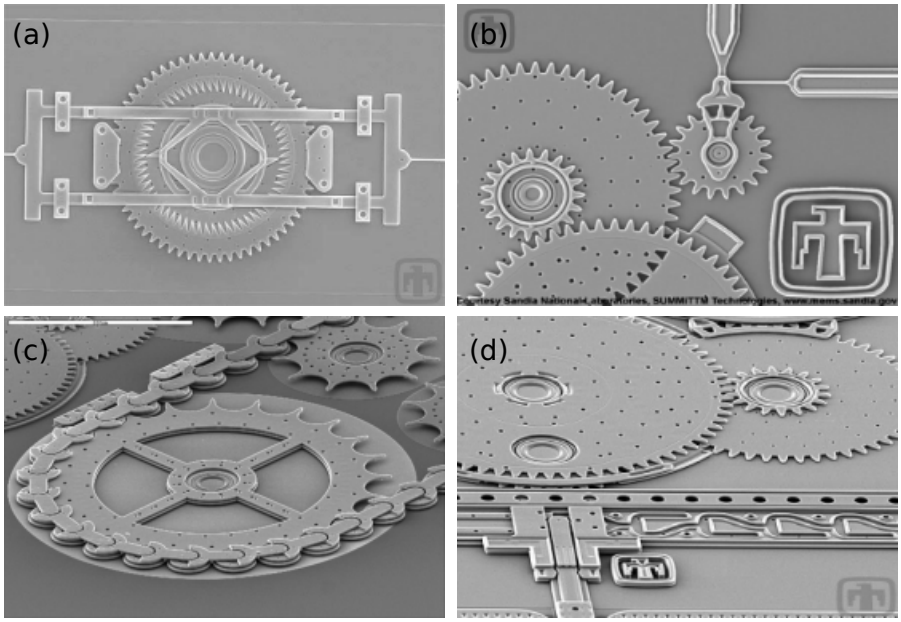

Figure 2.10: SEM images of micro motors fabricated by Sandia National Laboratories [94].

vantage that these devices offer is that, they can achieve complete 360° rotation. The main drawback of such friction based devices is that, they are highly prone to wear and tear with ageing. Another class is of non-contact, frictionless, flexure

based devices, with limited rotation range.

2.7.2 Comb-drive pair based actuation

Lim *et al.* [95] used an electrostatic rotary comb-drive based actuator for driving a folded mirror, which was connected to the optical attenuator. An SEM image of the fabricated rotary comb-drive based device is depicted in figure 2.11. The

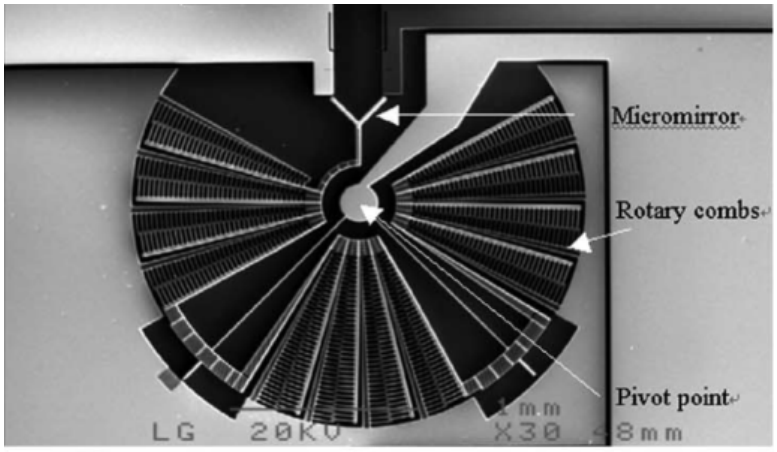

Figure 2.11: SEM image of the rotary comb-drive based actuator for moving the micro folded mirror [95].

structure was fabricated using a single mask fabrication process. The combs of the structure were connected by a beam of length 1200 µm and the structure was suspended on two cantilever-type beams of length 1000 µm and width 2.5 µm. The device reported an angular deflection of 2.4° with an actuation voltage of 21 V.

Yeh *et.al* [96] increased the angular range deflection by 18° (± 9° bidirectional rotational movement) on a similar structure (figure 2.12) by modifying the supporting cantilever-type beam into a serpentine structure. The performance summary of varying the length of the serpentine spring from 500 µm to 900 µm and the flexure opening dimension from 7 µm to 13 µm, with a span length of 35 µm were presented

in [96]. The device performed best with a spring length of 600 µm, and a flexure opening of 7 µm for an applied voltage of approximately 80 V. The resonant frequency of the device was calculated to be 445 Hz. A similar performance was also achieved with a flexure opening of 10 µm and spring length of 900 µm by lowering the spring constant (resonant frequency = 340 Hz).

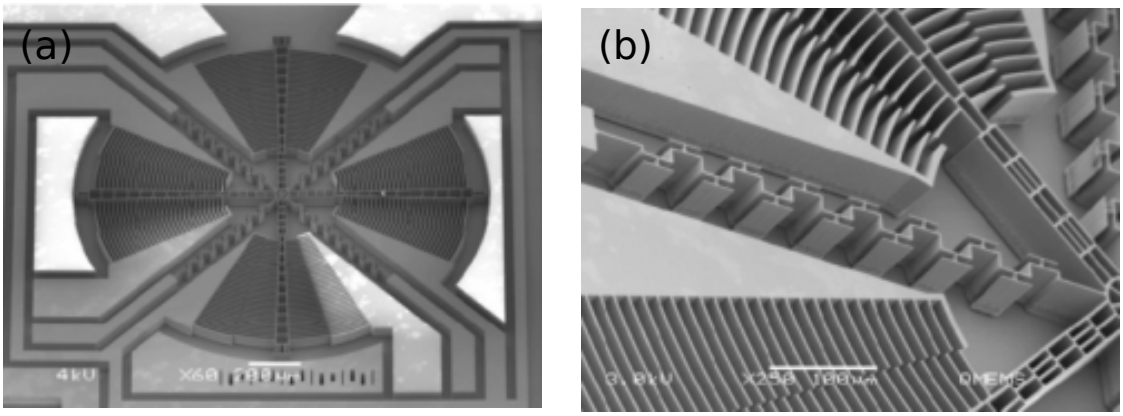

Figure 2.12: (a) SEM image of the rotary comb-drive based actuator; (b) close-up view of the serpentine spring connecting the structure [96].

Yeh *et al.* [97] extended this by employing a similar structure for making variable optical attenuator. The device showed an angular deflection even at low voltage. An SEM image of the fabricated structure is depicted in figure 2.13. The device has a 1000 µm radius with a resonant frequency of 400 Hz and a rotation angle of 2.6° for an applied voltage of 5 V. The minimum feature dimension of the device was 4 µm comb-finger with a spacing separation of 4 µm.

Yu *et al.* [98] realized rotational tuning of diffraction grating using comb-drive actuation method. The grating was inscribed on a rotational disc that is connected by two cantilever beams on either side. Cantilever flexure beams were attached with comb-drive based devices for actuation. An SEM image of the device is shown in figure 2.14. This device was operated to work in resonance mode, which is one of

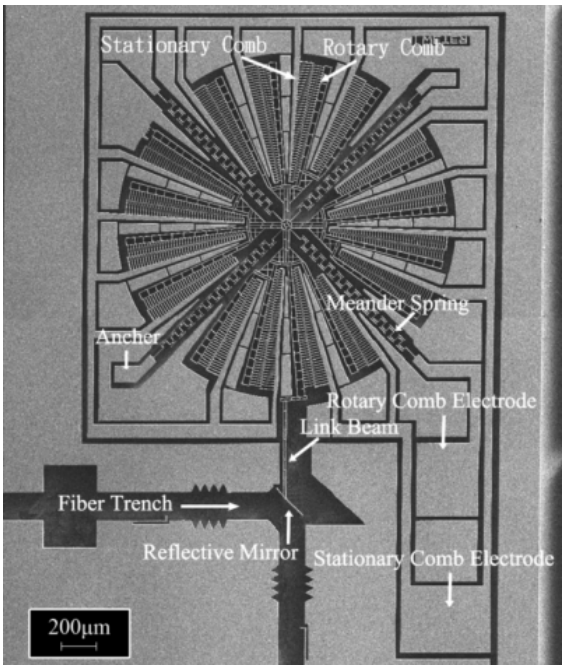

Figure 2.13: SEM image of a variable optical attenuator using rotary comb drive actuator [97].

the drawbacks to employ it in imaging systems with normal CCD cameras, where the read out time is slow.

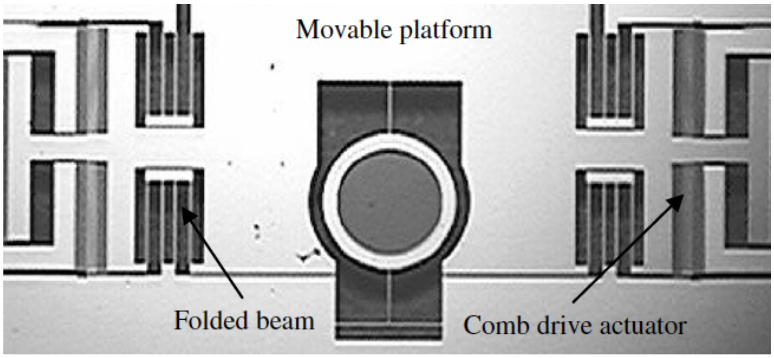

Figure 2.14: SEM image of the rotational grating design to operate in resonance mode [98].

2.7.3 Stepper motor based actuation

The working principle of the micro stepper motor is similar to that of macro stepper motor, except the difference in the driving mechanism. In MEMS devices, the stator poles are activated by electrostatic force than by magnetic force. A schematic of the working principle of the stepper motor is presented in figure 2.15. During the first phase, (1/3) of the poles are activated and the rotor aligns its poles to balance the electrostatic force generated. In the next cycle, the poles that are adjacent to the activated stator poles are excited such that the rotor moves to the next stable position to counterbalance the electrostatic force. This continues in the 3^{rd} phase and the cycle repeats.

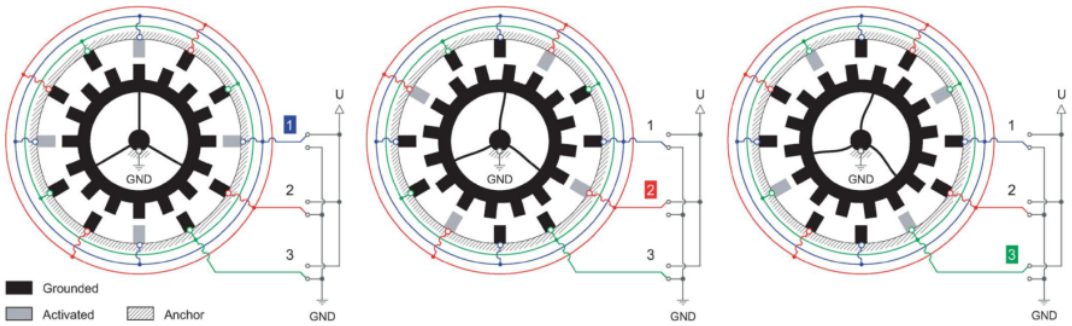

Figure 2.15: Schematic of the working mechanism of stepper motor [99].

Based on the electrostatic stepper motor principle, Yaseen *et al.* [100] realized a rotational diffraction grating with polysilicon micro motors. The schematic and fabricated structures are shown in figure 2.16. The motor was fabricated using a polysilicon layer of 5 µm thickness on top of a silicon wafer. The axle was connected to a bearing mechanism of the same material, and the rotary part was patterned for making the diffraction grating. The main advantage of this design is that it allows complete 360° rotation. However, the drawback of this type of friction based

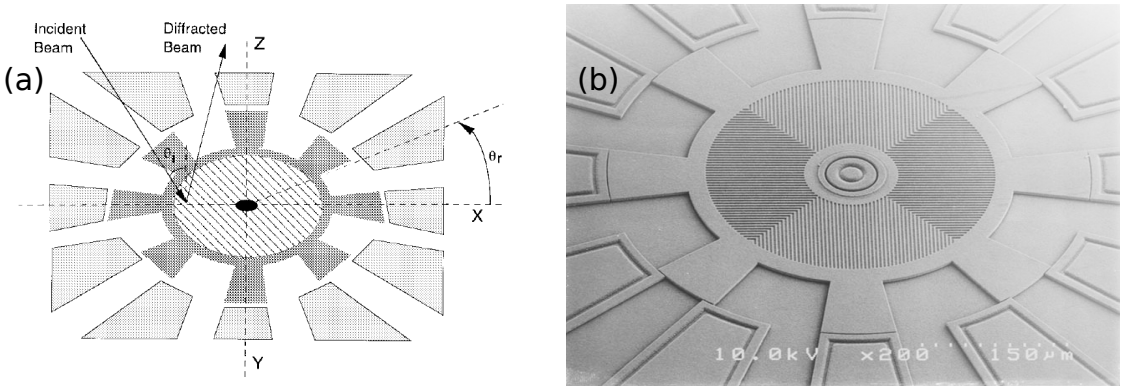

Figure 2.16: (a) Schematic of the electrostatic rotary diffraction grating scanner, (b) SEM image of the realized structure [100].

device is the difficulty in fabrication and often possess low life expectancy.

Flexure based bearing mechanism is another category, initially proposed by Sarajlic *et.al* [99], used to drive the motor that works with the principle of electrostatic actuation with a limited actuation range. Implementation was based on stepping motion actuation on a butterfly pivot structure [101] using MEMS technology. The schematic representation of the frictionless butterfly pivot structure and an SEM image of the micro stepper motor fabricated using MEMS technology is depicted in figure 2.17. The structure was fabricated on an SOI wafer and the device has a diameter of 1.2 mm, allowing a rotation angle of $4.2°(\pm 2.1°)$ for 45 V. A single-mask fabrication process was employed to fabricate this structure.

A much-improved design was attained by Sarajlic *et al.* [102] by increasing the rotation angle by 26° at an actuation voltage of 75 V. SEM images of the fabricated structure are depicted in figure 2.18. This structure was fabricated on a silicon wafer by selective control of etching from the back side. Insulation was provided between the electrodes with vertical trench isolation technique. The device has a radius of ∼700 µm and a resonant frequency of 280 Hz. The fabrication was

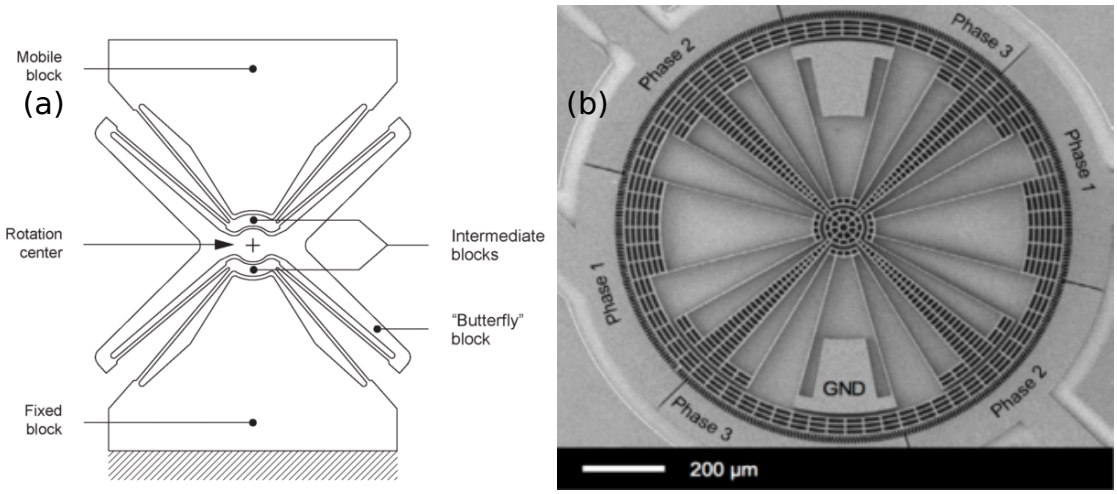

Figure 2.17: (a) Schematic representation of butterfly pivot structure that allows rotational movement, (b) SEM image of the fabricated micromotor actuated by stepper motor working principle [99].

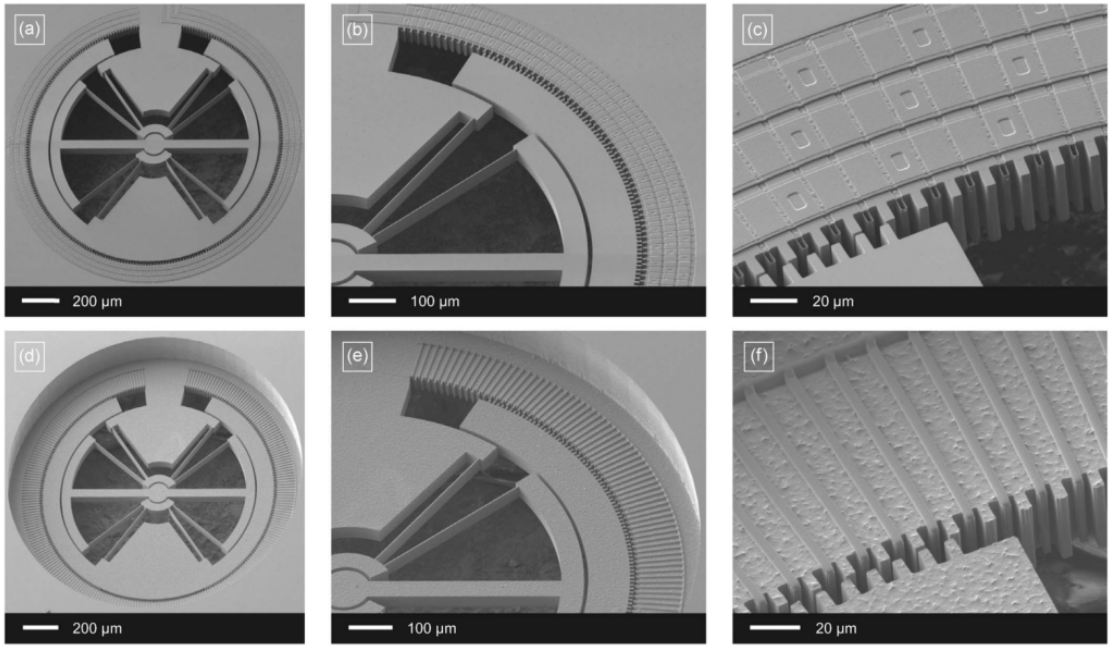

Figure 2.18: The top view and bottom view of electrostatic rotary stepper motor fabricated by the vertical trench isolation process [102].

performed with five masks and the fabrication process is found to be challenging.

In the updated model, the complex five mask fabrication process was made simpler with two sets of models: one with a single mask process and the other

with two mask process [103]. The devices were fabricated on a 50 µm SOI wafer using surface micromachining. SEM images of the fabricated device are depicted in figure 2.19. The device attained an angular rotation of 30° (±15° bidirectional) on

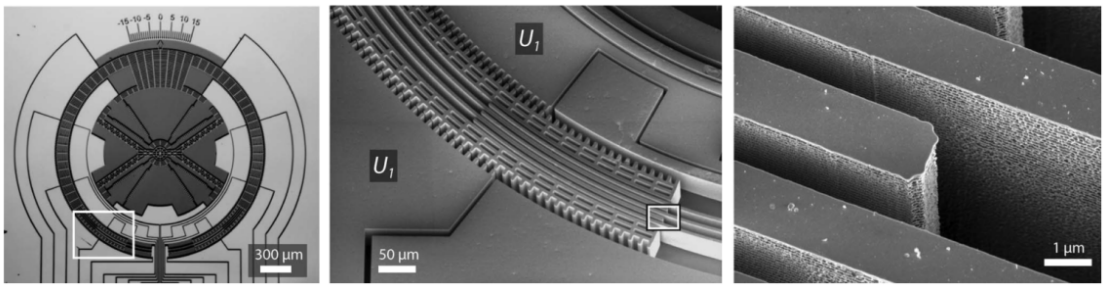

Figure 2.19: SEM image of the fabricated micro stepper motor using single mask fabrication process [103].

both types of motors. The resonant frequencies of both the motors were ∼150 Hz.

A brief summary of flexure based rotary actuator devices is described in table 2.1 showing the design parameters with performance. It is clear from table 2.1 that, stepper motor based butterfly pivot rotary design is the best choice for achieving large angular rotation.

Table 2.1: Summary of different flexure type rotary actuator.

Reference	**Actuator mechanism**	**r** (µm)	**t** (µm)	$\mathbf{K}_\theta$ (N m rad^{-1})	$\mathcal{T}_e$ (nN m)	**V** (V)	$\mathbf{f}_0$ (Hz)	θ_0
Lim *et al.* [95]	comb drive	1200	80			21		2.4°
Yeh *et al.* (D1) [96]	comb drive	900	60			60	340	± 9°
Yeh *et al.* (D2) [96]	comb drive	600	60			80	445	± 9°
Yeh *et al.* [97]	comb drive	800	85	1.8×10^{-8}	0.8	5	350	2.6°
Sarajlic *et al.* [99]	stepper motor	600	25	3.1×10^{-7}	11.34	45		± 2.1°
Sarajlic *et al.* [102]	stepper motor	700	40	1.4×10^{-7}	32.55	75	280	± 13°
Stranczl *et al.* (M1) [103]	stepper motor	700	50	1.67×10^{-8}	4.2	130Vpp	163	± 15°
Stranczl *et al.* (M2) [103]	stepper motor	900	50	1.67×10^{-8}	4.08	46Vpp	150	± 15°

$\mathbf{r} \rightarrow$ radius,

$\mathbf{t} \rightarrow$ thickness,

$\mathbf{K}_\theta \rightarrow$ Angular stiffness,

$\mathcal{T}_e \rightarrow$ torque,

$V \rightarrow$ actuation voltage,

$\mathbf{f}_0 \rightarrow$ resonant frequency,

$\theta_0 \rightarrow$ Angular deflection.

2.8 Summary

The literature survey briefly covered an overview of the spectrometric devices and tools used to measure material properties. Compared with point, line, and spectral scanning systems, the snapshot data acquisition system is a promising area, which needs to be further investigated to capture simultaneously, spatial and spectral data with higher resolution. A lot more work has to be done in the miniaturization of the optical design, for which the use of MEMS technology is appealing. Although the concept of pitch tuning by MEMS diffraction grating has been demonstrated by the previous researchers, an in-depth analysis has not yet been carried out to the application level. Tuning of the diffraction grating using rotation is not well explored, but it has the potential use in optical modulation, scanning, display technologies and spectrometers. The drawbacks of the rotational diffraction grating attempted in the past has low fill factor, limited actuation range, low diffraction efficiency and were operated in the resonant frequency. These limitations could be addressed by integrating highly efficient diffraction grating with flexure bearing motors, that transcends the state-of-the-art challenges.

Chapter 3

Integral field spectroscopy architectures

3.1 Introduction

The imaging spectrometer has been used over two decades to obtain three-dimensional information of light emitted from an object or scene. The three-dimensional image is the intensity distribution of two spatial and one spectral informations, $I(x, y, \lambda)$ referred to as datacube. This chapter discusses the optical configurations of imaging spectrometers along with ray tracing analysis and possible diversity implementation schemes. As discussed in section 2.2.2, the scanning-based imaging spectrometers are inherently slow and light inefficient due to a sequential data acquisition practice [104]. Snapshot imaging is introduced to overcome the limitations of scanning systems for fast datacube acquisition. It helps in overcoming motion artifacts and enables system miniaturization by removing complex mechanical scanning systems.

Snapshot systems are divided into two categories: direct and indirect (or computational). Direct methods divide the image sensor (CCD/CMOS) into separate parts responsible for sensing different wavelengths. In indirect procedure, spectral signals impinging on the camera pixels may not be well defined. Hence, for such cases, spectral retrieval is connected with computational algorithms. The most straightforward example of a direct system is the RGB sensor employed in commercial cameras. Inside the architecture, each pixel is divided into different areas covered with desired spectral filters (Bayer filter) for parallel sensing of three colors within an image [3]. As this approach is widely used for tricolor imagers, it can also be extended to multispectral imaging devices [105]. The inherent limitation of such a method is the trade-off between spectral and spatial resolution. An increase in the number of spectral channels rapidly degrades spatial resolution.

A novel integral field spectrometer (IFS) was designed by taking advantage of plenoptic imaging architecture [106], with close spacing of the microlens array (MLA) for good spatial resolution along with the computational methods for image reconstruction. This close spacing of microlens leads to spectral crosstalk in the image sensor. Algorithms such as Wiener inversion [107] or Tikhonov regularization matrix inversion [72], or compressive sensing approach [108] are the possible methods to retrieve back the information [109]. The inversion algorithm mostly depends on the type of the object and becomes even complex if it is affected by noise. In such a scenario, a single measurement scheme may not be sufficient to retrieve back the complete hypercube dataset. Hence, quasi-snapshot imaging schemes are employed to address this problem. Multiple diverse measurements is a strategy to capture more information which results in improved reconstruction quality [110].

A tunable optical element for optical transfer function diversity could be a possible choice for making multiple measurements.

Light field imaging or plenoptic imaging provides 4D information by capturing the two spatial dimensions (x, y) and angular information (α_x, α_y). A dispersive element in the optical systems is the diffraction grating to capture spectral information (λ). Proper positioning of the diffraction grating in the optical system helps in resolving spatial or angular (or a combination of both) wavelength-dependent shifts based on the light field distribution. The following sections investigate light field distribution with ray tracing analysis.

3.2 Design tools

In general, optical analysis is carried out analytically based on ray transfer ABCD matrices given by Eq. (3.1).

$$\begin{bmatrix} x_{out} \\ \alpha_{out} \end{bmatrix} = M \begin{bmatrix} x_{in} \\ \alpha_{in} \end{bmatrix} \tag{3.1a}$$

$$M = \begin{bmatrix} A & B \\ C & D \end{bmatrix} \tag{3.1b}$$

This is valid under paraxial approximation where the rays are assumed to be incident on the optical elements in small angles so that $\sin\theta$ can be approximated to θ; also called as small angle approximation.

A, B, C, and D are the system parameters of the optical system, providing the ray height and the ray angle emerging from the output optical system. The overall optical system matrix, M_{sys} (in figure 3.1) is computed by matrix multiplication of

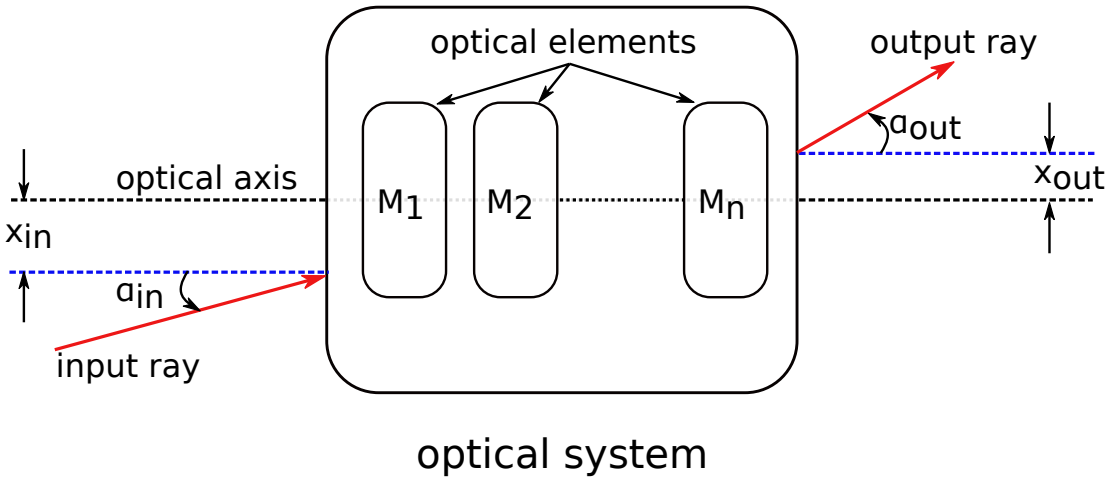

Figure 3.1: Ray propagation formalism using ABCD matrix with input coordinates: height (x_{in}), angle (α_{in}) and output coordinates: height (x_{out}), angle (α_{out}).

the individual ABCD matrices (Eq. (3.2)) of the optical components, performed from output to input.

$$M_{sys} = M_n \dots M_2 M_1 \tag{3.2}$$

In the case of an optical system with dispersive elements (diffraction grating) or decentered optical elements (MLA) standard 2×2 matrices cannot be used. The dispersive elements introduce wavelength dependent tilt, and the microlens array (MLA) causes a shift in the centre optical axis (off-centre). The extended formalism employing 3×3 matrices is used to describe ray transformation, allowing computing the system response which has tilt and off-center [111, 112]. Eq. (3.3) represents the extended formalism *i.e* ABCD-EF matrix for such a system:

$$\begin{bmatrix} x_{out} \\ \alpha_{out} \\ 1 \end{bmatrix} = \underbrace{\begin{bmatrix} A & B & E \\ C & D & F \\ 0 & 0 & 1 \end{bmatrix}}_{M} \begin{bmatrix} x_{in} \\ \alpha_{in} \\ 1 \end{bmatrix} \tag{3.3}$$

Here, the diffraction grating introduces wavelength dependent shift to the incident rays. Assuming that the system is aligned along the diffracted beam with centre wavelength (λ_0), the ray tilt (γ) introduced by the grating for wavelength (λ) is given by Eq. (3.4):

$$\sin\gamma = \gamma = m\frac{\lambda_0 - \lambda}{\Lambda} \tag{3.4}$$

where, Λ is the grating period and m is diffraction order. The MLA is treated as a set of single lenses laterally displaced from the optical axis. The MLA can be analyzed by ray tracing method on a one-by-one basis. The matrix for each lenslet in the array is parametrized by its centre position x_0.

3.3 Optical design

Here, imaging spectroscopy with a combination of the diffraction grating and the microlens array is considered to generate an intensity pattern on the detector plane. This type of optical system is a so-called computational imaging technique and requires a specific design that is strictly connected to the reconstruction algorithms to calculate the desired spectrum. A few optical configurations are investigated in the following sections.

3.3.1 2F-G-2F-MLA configuration

2F-G-2F-MLA is similar to a classical spectroscopic arrangement, where the diffraction grating is placed at the Fourier plane of the 4-F imaging configuration. The response of the system is analyzed by placing the MLA before the camera/detector plane as depicted in figure 3.2. The purpose of this approach is to investigate

the spatial dependence present in the output plane due to the angular shift in the diffraction grating.

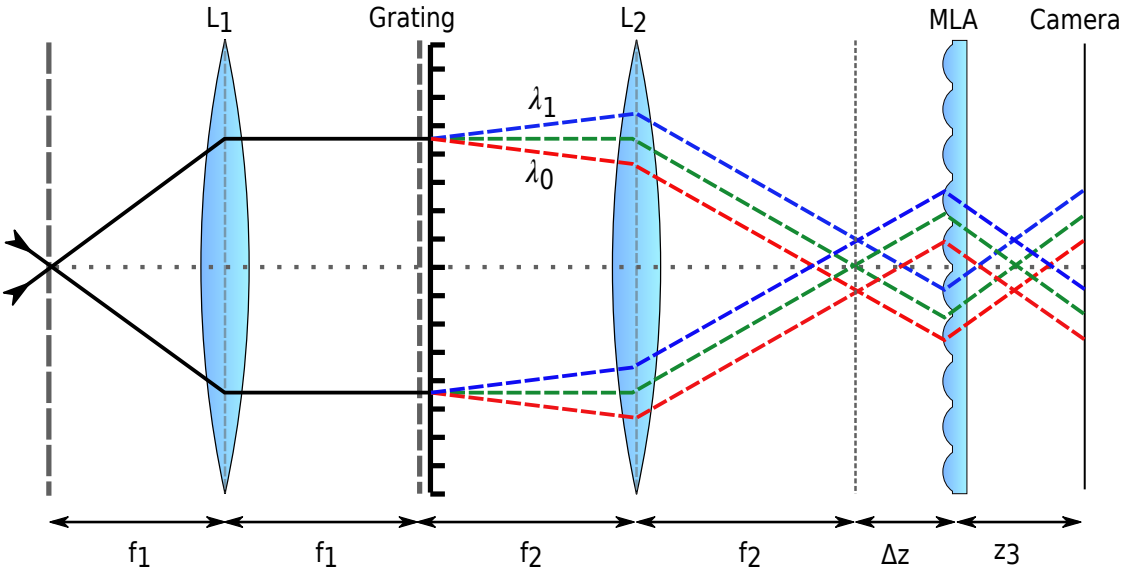

Figure 3.2: Schematic representation of IFS optical design when the diffraction grating is placed at the Fourier plane.

The microlens array placed in front of the image sensor can be treated as a Shack-Hartmann sensor that can be utilized to calculate the wavefront of the light emitted from the object [113, 114]. The optical configuration is analyzed by ray tracing with the paraxial approximation, which uses ABCD-EF formalism [112]. The optical system behavior of its individual elements or interfaces is described in detail in appendix A. The following notations are used in deriving the forward model of the optical configuration.

- $P_{(z)}$ → free space propagation matrix with distance 'z'
- $L_{(f)}$ → lens matrix for focal length 'f' (assuming thin lens in this case)
- $T_{(\gamma)}$ → tilt operator by the dispersive element (diffraction grating) with the tilt angle 'γ'

- $M(f_{mla}, x_0) \rightarrow$ system matrix of MLA with shifted position 'x_0' and focal length 'f_{mla}'

The system transfer matrix for this optical configuration can be written as:

$$M_{2F-G-2F-MLA} = P_{(z_3)}.M(f_{mla}, x_0).P_{(\Delta z)}.P_{(f_2)}.L_{(f_2)}.P_{(f_2)}.T_{(\gamma)}.P_{(f_1)}.L_{(f_1)}.P_{(f_1)} \tag{3.5}$$

Computing the matrix multiplication for the Eq. (3.5) gives the system response matrix given by Eq. (3.6)

$$M_{2F-G-2F-MLA} = \begin{pmatrix} -\frac{f_2\,(f_{mla}-z_3)}{f_1\,f_{mla}} & -\frac{f_1\,(\Delta z\,f_{mla}-\Delta z\,z_3+f_{mla}\,z_3)}{f_2\,f_{mla}} & \frac{x_0\,z_3+f_2\,f_{mla}\,\gamma-f_2\,\gamma\,z_3}{f_{mla}} \\ \frac{f_2}{f_1\,f_{mla}} & \frac{f_1\,(\Delta z-f_{mla})}{f_2\,f_{mla}} & \frac{x_0-f_2\,\gamma}{f_{mla}} \\ 0 & 0 & 1 \end{pmatrix} \tag{3.6}$$

The system matrix takes a simpler form in the light field imaging configuration by setting:

- $z_3 = f_{mla}$ - image plane is at the focus plane of the MLA
- $\Delta z = 0$ - object is imaged at the MLA with 4F configuration.

Then matrix $M_{2F-G-2F-MLA}$ takes the form (3.7):

$$M_{2F-G-2F-MLA} = \begin{pmatrix} 0 & -\frac{f_1\,f_{mla}}{f_2} & x_0 \\ \frac{f_2}{f_1\,f_{mla}} & \frac{f_1\,(\Delta z-f_{mla})}{f_2\,f_{mla}} & \frac{x_0-f_2\,\gamma}{f_{mla}} \\ 0 & 0 & 1 \end{pmatrix} \tag{3.7}$$

Substituting $M_{2F-G-2F-MLA}$ in Eq. (3.3) provides output ray height (Eq. (3.8)) as well as the output ray angle.

$$x_{out} = -\frac{f_1 f_{mla}}{f_2}\alpha_{in} + x_0 \tag{3.8}$$

It is clear from Eq. (3.8) that ray height (address in the spatial dimension) in the detector plane (x_{out}) is independent of the dispersion (as γ is absent in the term). Hence, this configuration is not suitable for the imaging spectrometer.

3.3.2 MLA-2F-G-2F configuration

Another architecture of interest is by placing the microlens array on the object plane in the classical spectrometer as depicted in figure 3.3. The object is imaged on to the microlens array that samples out the spatial data and the focusing plane of the microlens is re-imaged onto the detector (with a defocus) by 4-F imaging condition. The diffraction grating at the Fourier plane of this system produces a wavelength dependent shift that is manifested at the detector.

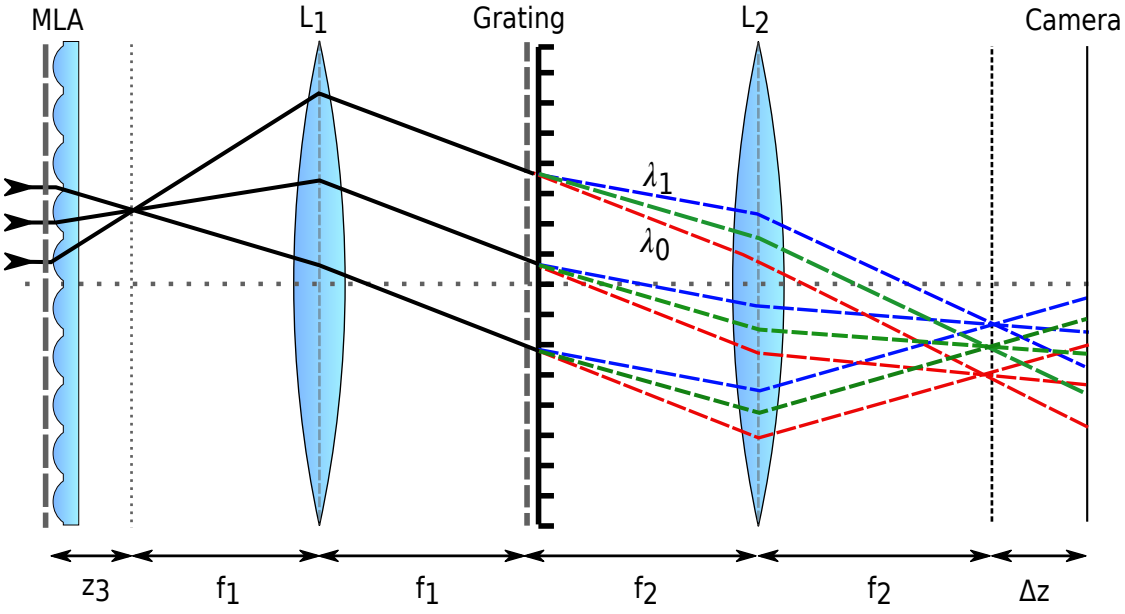

Figure 3.3: Schematic illustration of integral field spectroscopy with the microlens array placed in the object plane to sample spatial information.

The ray transformation matrix of the system represented by the ABCD-EF

matrix can be given by

$$M_{2F-G-2F-MLA} = P_{(\Delta z)}.P_{(f_2)}.L_{(f_2)}.P_{(f_2)}.T_{(\gamma)}.P_{(f_1)}.L_{(f_1)}.P_{(f_1)}.P_{(z_3)}.M(f_{mla}, x_0) \tag{3.9}$$

The system matrix obtained by solving the above matrix is:

$$M_{MLA-2F-G-2F} = \begin{pmatrix} \frac{\Delta z\, {f_1}^2 - {f_2}^2\, f_3 + {f_2}^2\, z_3}{f_1\, f_2\, f_3} & -\frac{\Delta z\, {f_1}^2 + z_3\, {f_2}^2}{f_1\, f_2} & -\frac{\Delta z\, x_0\, {f_1}^2 - 1\, f_3\, \gamma\, f_1\, {f_2}^2 + x_0\, z_3\, {f_2}^2}{f_1\, f_2\, f_3} \\ \frac{f_1}{f_2\, f_3} & -\frac{f_1}{f_2} & -\frac{f_1\, x_0}{f_2\, f_3} \\ 0 & 0 & 1 \end{pmatrix} \tag{3.10}$$

The above general architecture can be further simplified by setting $z_3 = f_{mla}$ and $\Delta z = 0$:

$$M_{MLA-2F-G-2F} = \begin{pmatrix} 0 & -\frac{f_2\, f_{mla}}{f_1} & -\frac{f_2\, (x_0 - f_1\, \gamma)}{f_1} \\ \frac{f_1}{f_2\, f_{mla}} & -\frac{f_1}{f_2} & -\frac{f_1\, x_0}{f_2\, f_{mla}} \\ 0 & 0 & 1 \end{pmatrix} \tag{3.11}$$

In this condition, the object is projected on to the microlens. The sampling of the microlens determines the spatial resolution of the datacube. Each microlens produces an individual focus in the plane where $z_3 = f_{mla}$. The focal plane is re-imaged on to the camera provided it captures the spectral dependant spot at the image plane. The output dependent relation is obtained by substituting $M_{MLA-2F-G-2F}$ in Eq. (3.3) which gives:

$$x_{out} = -\frac{f_2 f_{mla}}{f_1}\alpha_{in} + \gamma - \left(\frac{f_2}{f_1}\right) x_0 \tag{3.12}$$

From Eq. (3.12), it can be seen that the output position has clear dependence on the wavelength (grating angular tilt). Hence this architecture is suitable to acquiring spectral-spatial information of the the object.

3.3.3 G-4F-MLA Configuration

An alternative architecture could be a one slightly deviating from the classical spectroscopic systems, where a diffraction grating is placed at the object plane as depicted in figure 3.4. It results in the encoding of the spectrum in ray angles instead of ray shift as in classical spectrometers (where the grating is located at the Fourier plane). The object imaged onto the diffraction grating is imaged again onto the microlens array. Wavelength dependent shift caused by the diffraction grating is projected on the MLA.

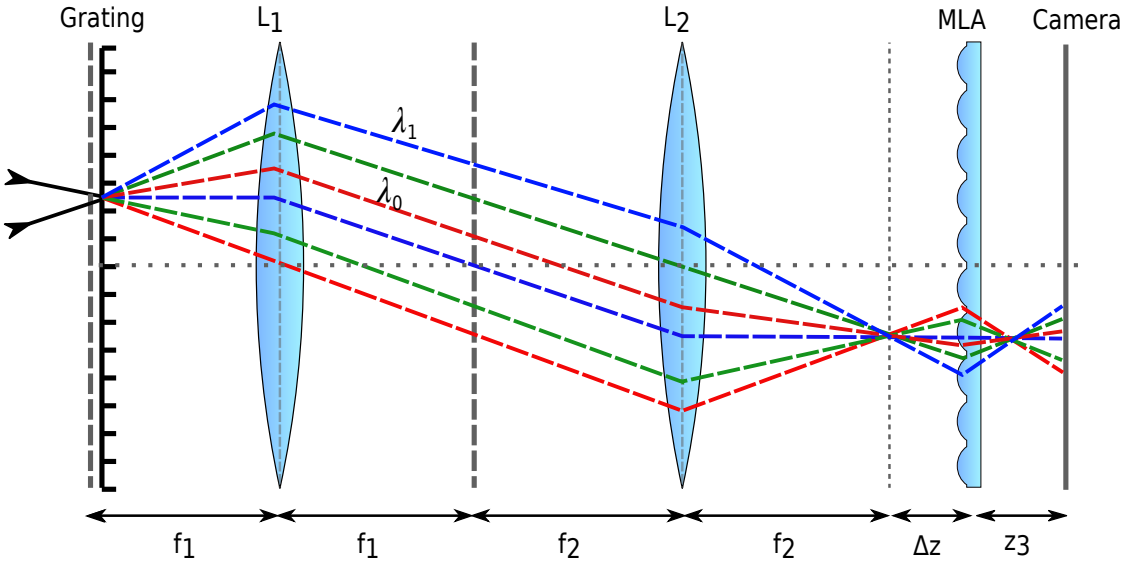

Figure 3.4: Schematic illustration of IFS optical design when diffraction grating is placed at the object plane.

To conserve the imaging properties of the optical system, paraxial approximation has to be fulfilled, and then diffractive grating can be treated as a linear element. Microlens array, together with an image sensor, forms a light field imaging subsystem allowing measurement of the image intensity as a function of angles and position.

The system transfer matrix for this configuration is given by Eq. (3.13)

$$M_{G-4F-MLA} = P_{(z_3)}.M(f_{mla}, x_0).P_{(\Delta z)}.P_{(f_2)}.L_{(f_2)}.P_{(f_2+f_1)}.L_{(f_1)}.P_{(f_1)}.T_{(\gamma)} \quad (3.13)$$

Computing the above system matrix leads to Eq. (3.14):

$$M_{G-4F-MLA} = \begin{pmatrix} -\frac{f_2\,(f_{mla}-z_3)}{f_1\,f_{mla}} & -\frac{f_1\,(\Delta z\,f_{mla}-\Delta z\,z_3+f_{mla}\,z_3)}{f_2\,f_{mla}} & \frac{f_2\,x_0\,z_3-f_1\,f_{mla}\,\gamma\,z_3-\Delta z\,f_1\,f_{mla}\,\gamma+\Delta z\,f_1\,\gamma\,z_3}{f_2\,f_{mla}} \\ \frac{f_2}{f_1\,f_{mla}} & \frac{f_1\,(\Delta z-f_{mla})}{f_2\,f_{mla}} & \frac{f_2\,x_0+\Delta z\,f_1\,\gamma-f_1\,f_{mla}\,\gamma}{f_2\,f_{mla}} \\ 0 & 0 & 1 \end{pmatrix} \quad (3.14)$$

The configuration is made simpler by setting:

- $z_3 = f_{mla}$ - image plane is at the focus plane of MLA
- $\Delta z = 0$ - object is imaged at MLA with 4F configuration.

Incorporating this condition simplifies $M_{G-4F-MLA}$ to Eq. (3.15):

$$M_{G-4F-MLA} = \begin{pmatrix} 0 & -\frac{f_1\,f_{mla}}{f_2} & \frac{f_2\,x_0-f_1\,f_{mla}\,\gamma}{f_2} \\ \frac{f_2}{f_1\,f_{mla}} & -\frac{f_1}{f_2} & \frac{f_2\,x_0-f_1\,f_{mla}\,\gamma}{f_2\,f_{mla}} \\ 0 & 0 & 1 \end{pmatrix} \quad (3.15)$$

The output ray height is obtained by substituting the simplified system matrix, $M_{G-4F-MLA}$ in Eq. (3.3) leads to:

$$x_{out} = -\frac{f_1 f_{mla}}{f_2}\alpha_{in} + \gamma\frac{f_1 f_{mla}}{f_2} + x_0 \quad (3.16)$$

In this configuration, the ray position in the image plane depends on the input ray angle (α_{in}) and the tilt introduced by the grating (γ). This system directly images the angles of rays impinging the lenslet. The dispersion term introduced by the grating adds a shift to the angle distribution. This results in ray shift proportional to γ. Similar systems are commonly used for measurement of a 4D

light field: each lenslet images the angular distribution (α_x, α_y) while different lenslets in the array sample the spatial distribution (x, y).

The aim is to obtain information about the spectrum within the 2D spatial image. In this specific system, spatial sampling is directly made by each lenslet (each lenslet is a spatial pixel): the area beneath each lenslet samples the (ray) angles impinging the particular lenslet surface. The diffraction grating interacting with the beam introduces a wavelength-dependent tilt that is manifested on this angle-image, and as visible from Eq. (3.16), the wavelength-dependent part produces a ray shift in the plane of the lenslet image. In the case of monochromatic light, the lenslet image corresponds to the angle distribution function of the illumination. When more wavelengths are present in the object, the picture is the sum (or overlap) of the shifted angle distribution function.

It can be concluded from the above discussion that MLA-2F-G-2F and G-4F-MLA can be employed for realizing integral field spectroscopy to compute the spectral data that are obtained from the discrete spatially separated microlens. The two configurations generate similar images, and the only difference is in the magnification of the output image.

3.4 Ray tracing analysis

The optical design of the G-4F-MLA configuration was further analyzed using ray tracing with Zemax [115]. The MLA-2F-G-2F configuration also generated same results in the simulations except for the magnification factor. To project the object onto the grating, an additional 4-F imaging system was added before the diffraction grating. The schematic layout of the analysis carried out in Zemax is depicted in

figure 3.5.

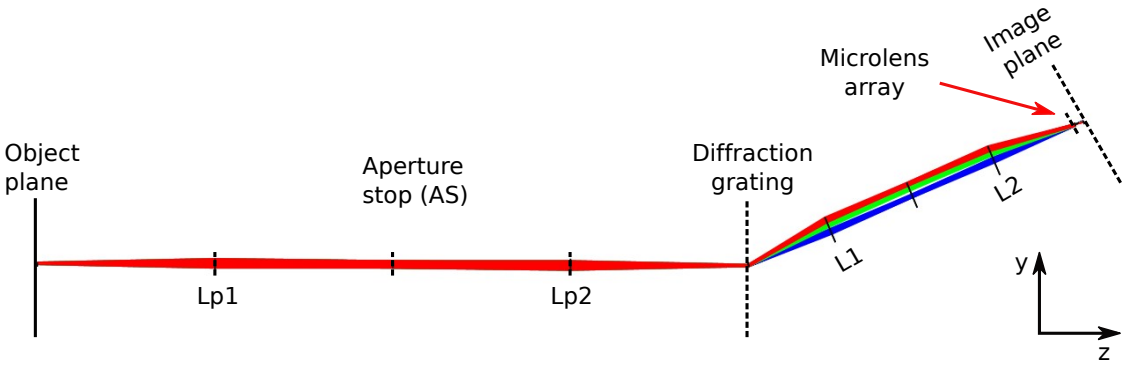

Figure 3.5: Ray diagrams of G-4F-MLA configuration simulated with Zemax.

The aperture was defined by an in-built "float by stop size" model. Three closely spaced sets of wavelengths, 540 nm, 550 nm and 560 nm with 10 nm separation were investigated in the analysis. Spot diagram analysis and image simulations were carried out for this optical system. To guarantee paraxial approximation, the lenses were defined by focal length. Lenses, 'Lp1' and 'Lp2' form the 4-F configuration mapping the object onto the grating. Diffraction grating disperses out the wavelengths, based on the diffraction relation, which were again mapped onto the microlens array with the 2^{nd} 4-F imaging configuration (L1 and L2). All the lenses were defined by a fixed focal length of 50 mm, thereby having a magnification of unity. The first order diffraction grating with 830 lines/mm was used to disperse the wavelength of the field. The centre wavelength (550 nm) creates an angular shift of 27.16° based on the diffraction relation. To compensate this shift, all the elements after the diffraction grating were tilted along with the same angle. The MLA was defined individually by the multi-configuration editor.

The image formed on the microlens focuses onto the detector plane which, appears as a spot of individual wavelengths in that field [113]. Nine fields were

selected with a weighing factor of unity to produce uniform intensity distribution, and the positioning of fields were defined in such way that rays of each fields fall on a single microlens (figure 3.6a). The spots generated by all the fields in the image plane by increasing the size of the aperture stop (AS) as depicted in figure 3.6b. It implies that the AS should be selectively chosen to avoid overlap between the fields. There need to be an optimization between the camera pixel size, AS size and magnification. The image obtained from a single microlens was an overlap of the different wavelength spots depicted in figure 3.6c, where the three colors correspond to 540 nm, 550 nm, and 560 nm, respectively. In the experiments, these spots appeared as the overlap of intensities of the wavelengths.

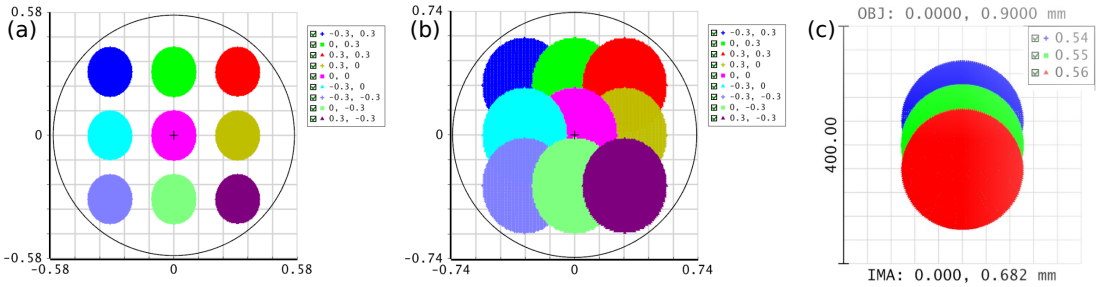

Figure 3.6: (a) Spot-diagram obtained at the image plane by 9 different sets of fields, (b) spots overlapping each other by increasing size of the aperture stop, and (c) spot-diagram obtained by a single microlens for 3 sets of wavelengths.

Geometric bitmap image analysis by ray tracing of a 2D image scene of size 640 × 480 pixels was carried out with a fixed aperture, by removing the vignetting factors. The pixel size was set to 5 µm×5 µm and 100 rays were set to be incident per pixel. The increase in ray density per pixel improves the quality of the image. The images obtained at different positions of the optical elements were analyzed

and depicted in figure 3.7. The object mapped onto the diffraction grating gets dispersed and projected again onto the MLA using two 4-F configurations, resulting in even parity. The dispersed image was spatially sampled by the MLA and projected onto an image plane.

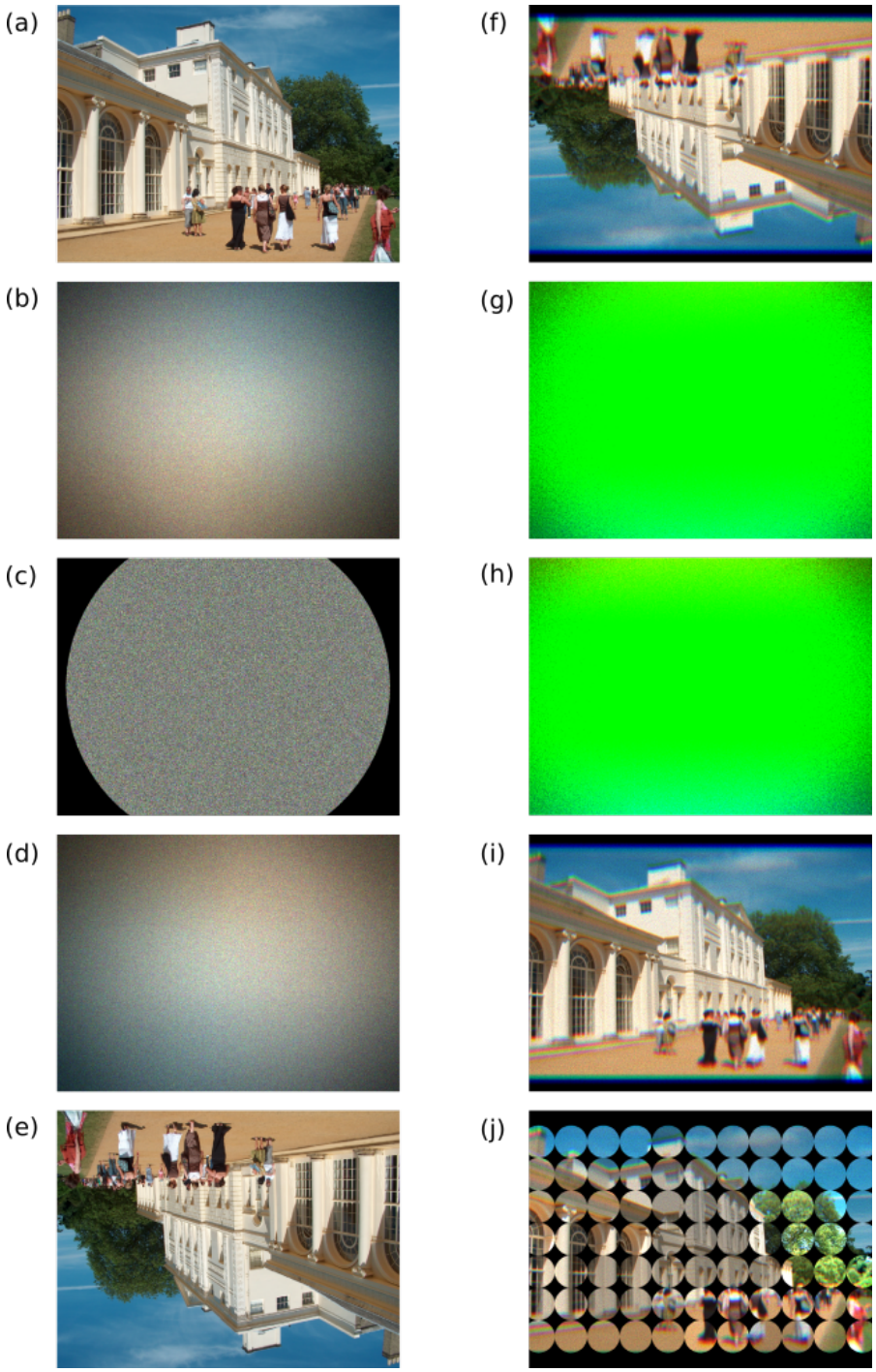

Figure 3.7: Geometric image ray tracing analysis: Image obtained at (a) object (source image), (b) Lp1, (c) aperture stop, (d) Lp2, (e) before diffraction grating, (f) after diffraction grating, (g) L1, (h) L2, (i) before MLA, and (j) sampling at MLA.

The spectrally resolvable wavelength is the overlap of the intensity distribution of the respective wavelengths, as depicted in figure 3.8a. The estimate of the original spectrum can be extracted by de-convolving the measured image with the point-spread function (PSF) of the optical system (figure 3.8b). The PSF was computed by projecting the image obtained by the central wavelength (550 nm) used in the simulation. A thresholding operation was performed for the calculated PSF to get the right kernel.

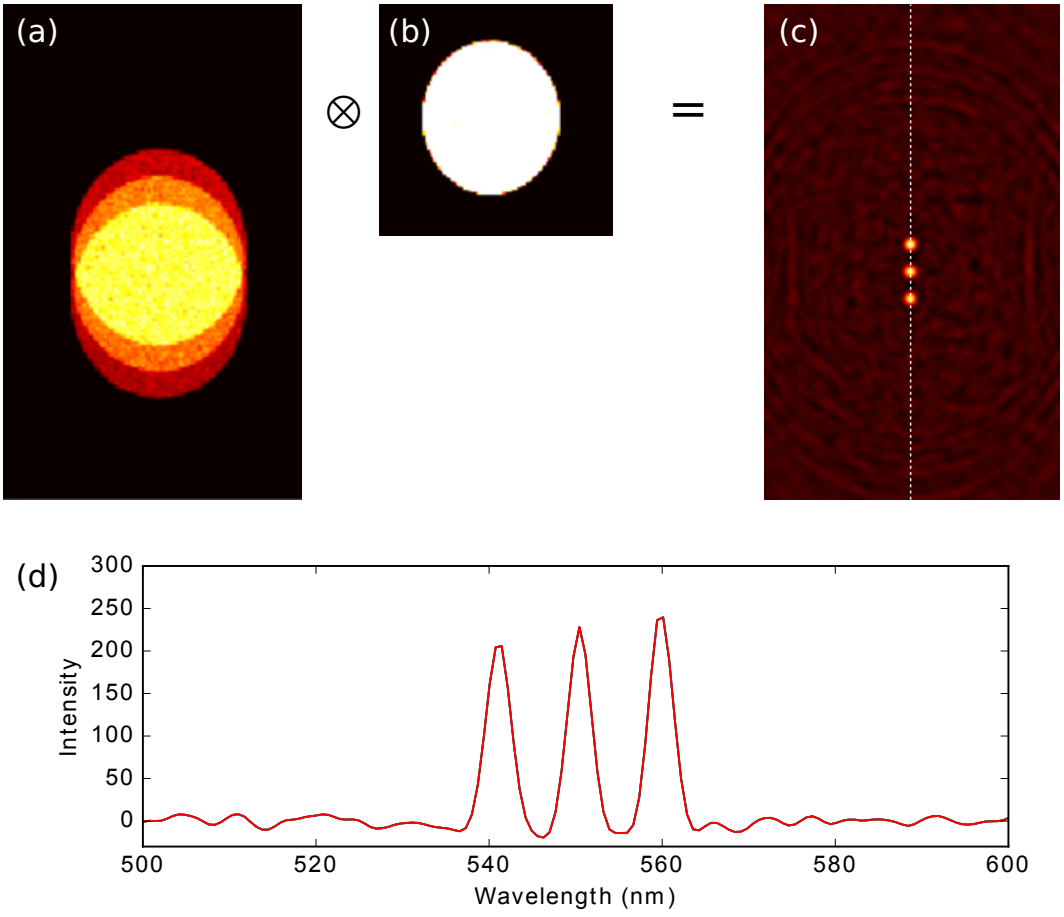

Figure 3.8: (a) Intensity distribution of wavelength measured by a single microlens, (b) PSF obtained by projecting the center wavelength, (c) the image retrieved by Wiener deconvolution, and (d) spectral line profile from the recovered image.

There are various inverse algorithms to retrieve the original data. The most commonly used algorithms are Wiener deconvolution, Tikhonov inversion, and compressive sensing approach which is discussed in section 2.4. For the above image, Wiener deconvolution was employed to extract wavelength information. Deconvolution by means of the Wiener filter can be computed by Eq. (3.17) [71]:

$$\hat{s} = \mathcal{F}^{-1}\left\{\frac{1}{\mathcal{H}_{(u,v)}}\left[\frac{|\mathcal{H}_{(u,v)}|^2}{|\mathcal{H}_{(u,v)}|^2 + \frac{1}{SNR}}\right]\mathcal{G}_{(u,v)}\right\} \tag{3.17}$$

where, $\hat{s}$ is estimate of the input signal, $\mathcal{H}_{(u,v)}$ is the Fourier transform of the point spread function, $\mathcal{G}_{(u,v)}$ is the Fourier transform of the measured signal, and SNR is the signal-to-noise ratio. The inverse filtering is implemented in Python (code is described in appendix C.1), and the spectral line profile obtained is depicted in figure 3.8d.

3.5 Spatial resolution improvement

The optical system produces an image that is composed of a set of lines corresponding to the total spectrum impinging on each lenslet in the MLA. This set of sub-images follows the arrangement of the lenslet, and the spectral lines are oriented along the dispersion direction defined by the diffraction grating (figure 3.9a). The concept of image splitting by microlenses suffers from the problem of crosstalk, *i.e.*, overlapping of spectra corresponding to different spatial pixels (figure 3.9b). In the standard configuration, crosstalk has to be minimized by considering the best arrangement of microlenses and dispersion direction [116]. However, this approach always leads to unused pixels in the camera. Hence, large sensors are needed if high spatial and spectral resolutions are required.

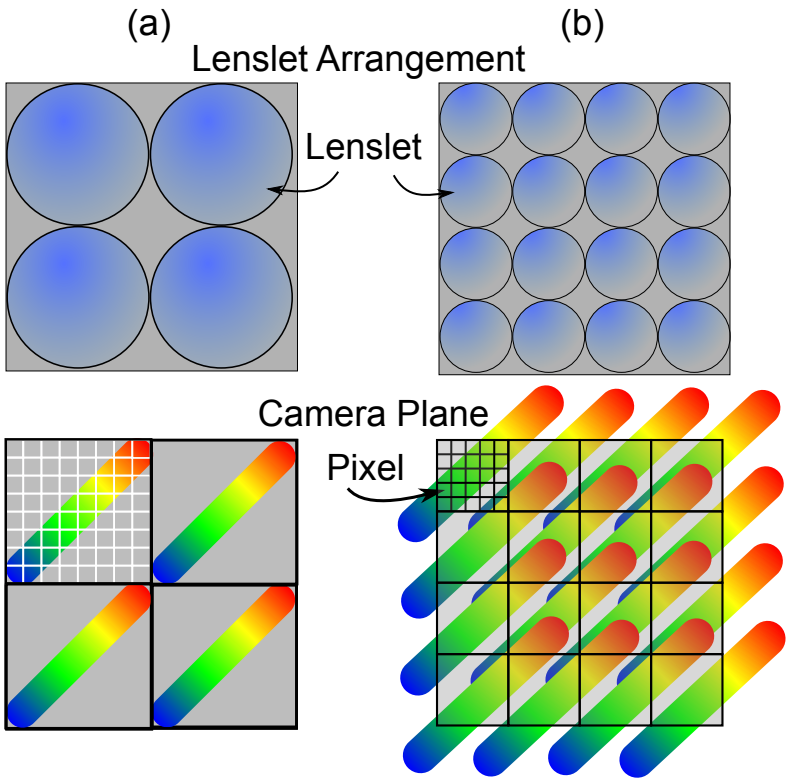

Figure 3.9: Schematic representation of the image generated at the camera. The upper row presents the lenslet size and position, while the bottom row shows the image formed on the camera. Two cases are considered: (a) with no cross talk and (b) with high cross talk.

In a configuration where crosstalk is allowed, the observed datacube cannot be read directly, since pixels contain a mixture of signals from different lenslets. Numerical inversion has to be used to recover the datacube from this mixed measurement. The advantage of background analysis is the possibility of performing a compressive measurement if prior knowledge about the measured object is available. In the case of ordinary hyperspectral datacubes, general or more specific prior information is often available. For example, similar to 2D images, spectral scenes often exhibit a piecewise-smooth structure. In addition, a diversity approach might further improve the fidelity of the reconstructions. In general, diversity refers to the

repetition of the same measurement with several systems having different impulse responses.

3.6 Diversity implementation schemes

3.6.1 Influence on aperture stop

In this section, spot-diagram simulations were carried out on the optical design to investigate the tuning of the aperture stop. Since the image plane and aperture stop were also separated by two 4-F configurations (Lp2-L1 and L2-MLA), the output directly manifests the shape of the AS. The output was inspected by an array of a 3×3 microlens to examine the impact of spot shape and spectrum. A smaller AS results in an image spot in which all the three wavelengths are completely separable. However, in this case, a high-resolution camera is necessary for precisely resolving the spectrum, which is well evident from figure 3.10(a). Setting a very big AS is also not preferred since, apart from mixing the wavelength, the neighboring spatial fields also get overlapped, resulting in multiple crosstalk (figure 3.10e,f), that will lead to complexity in the spectral retrieval. Large AS results in big PSF, that block the large coverage of spectrum. To cover a broader range of wavelengths, the AS has to be made smaller so that camera pixels can have the intensity distribution of more closely spaced wavelengths per pixel.

3.6.2 Influence on tunable grating

This section discusses how the tuning of the diffraction grating can impact the response of the image plane by keeping other parameters constant. Two methods

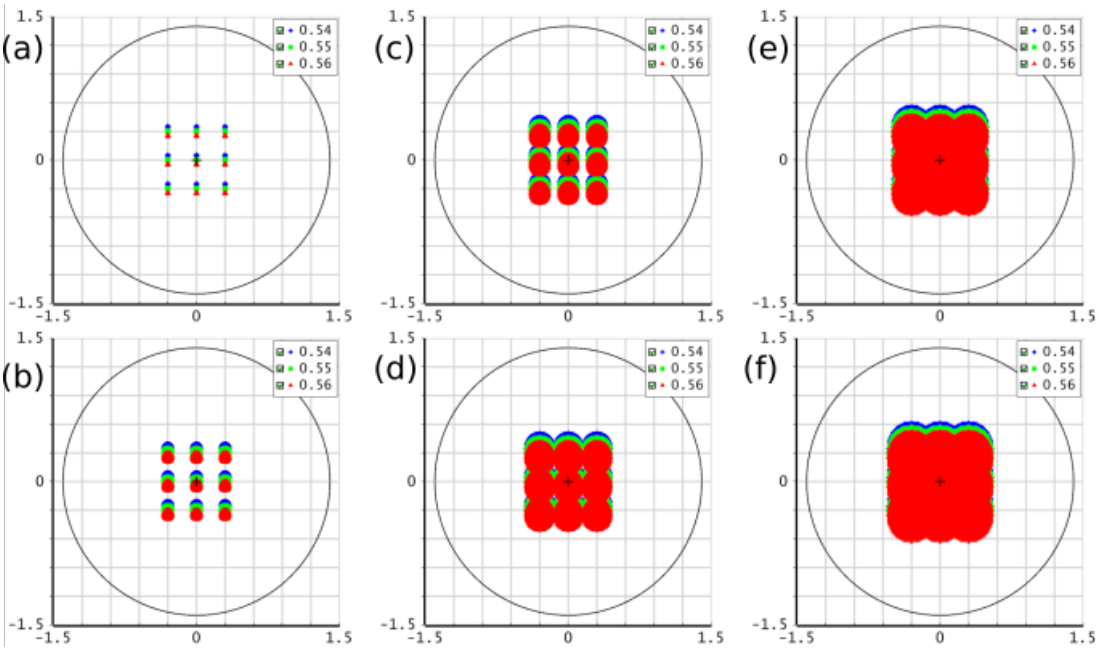

Figure 3.10: Simulated response of the IFS by varying the semi-diameter of aperture stop: (a) 0.1 mm, (b) 0.5 mm, (c) 1 mm, (d) 1.5 mm, (e) 2 mm, and (f) 2.5 mm.

were investigated for tuning: tuning by pitch and tuning by rotation. Pitch tuning was executed by changing the grating pitch. Rotation was introduced by changing the direction of dispersion.

3.6.2.1 Tuning by pitch changing

In this simulation, the detector plane was fixed at a size of 3 mm×3 mm and diffraction grating groove density was varied. The results obtained by varying the diffraction grating groove density from 500 lines/mm to 1100 lines/mm are depicted in figure 3.11. Based on the diffraction relation (Eq. (3.4)), individual wavelengths are shifted by a different amount with the grating pitch. Hence by knowing the tuning range, the shift of individual wavelength can be estimated.

Moreover, it is evident from figure 3.11 (a) and (f) that a smaller pitch (more

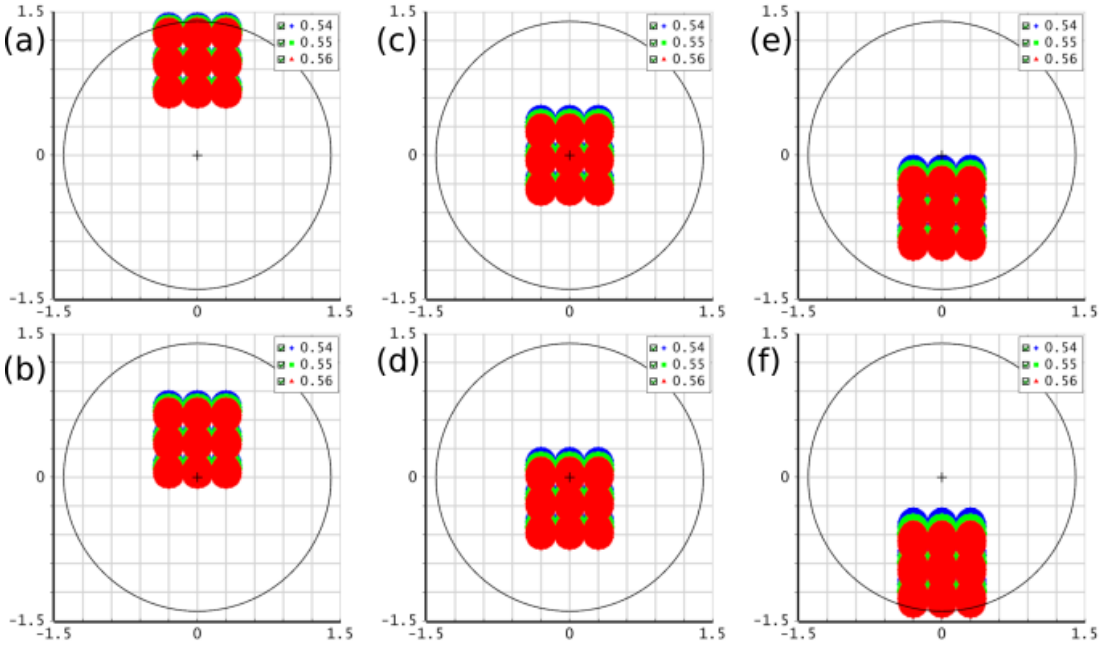

Figure 3.11: Simulated response of the IFS by varying the pitch of diffraction gratings: (a) 500 lines/mm, (b) 700 lines/mm, (c) 830 lines/mm, (d) 900 lines/mm, (e) 1000 lines/mm, and (f) 1100 lines/mm.

number of grating lines/mm) imparts more significant separation of wavelengths and vice versa. Hence, grove density changes the diffraction angle and thus results in different mixing of spectrum of individual lenslet. Since the variation in groove density (grating pitch) changes the mixing of spectral signals, it can be concluded that pitch tuning of diffraction grating is one of the choices for diversity implementation in IFS.

3.6.2.2 Tuning by rotation

In this section tuning of the diffraction grating by changing the orientation along a different axis (figure 3.5) is investigated. Impact on the image caused by rotation for 5 angles (from $-20°$ to $20°$) is depicted in figure 3.12. For rotation about

the x-axis, the dispersion spread is achieved in positive angles, which can be used to analyze the spectrum. However, along with the dispersion shift, the shape of the spot is elongated, which is caused due to the defocusing of the image on the grating. Hence for each microlens, the point-spread function differs at different angles. It might lead to complexity in the reconstruction algorithm, since each microlens produces a non-unique shaped PSF. For negative angles, it is interesting to note that there is no positional shift in the camera, which is advantageous; nevertheless, it is observed that no additional information is obtained as there is no significant change in the dispersion shift or direction. Rotation about the y-axis gives an intriguing result, where the dispersion spot is overlapped with the adjacent microlens in the desired way. Again, as mentioned in the previous case, the shape of the spot is gets affected by the defocus in fields.

Another scenario is the rotation about the optical axis (about the z-axis), which provides promising results. With a slight tuning in the z-direction, a directional change in the dispersion orientations is produced resulting in mixing of wavelength spots. Hence, tuning produces different mixing (overlapping) of signals with adjacent microlens, providing more information. In this case, the shape of the spot remains the same, which would be advantageous for reconstruction or unmixing, since the PSF remains consistent for all the microlenses. Based on Fourier optics, rotation introduces a positional shift in the angular tuning about the optical axis, which is evident in figure 3.12; while for larger tuning, it might lead to vignetting. Nevertheless, this hurdle could be solved by three shot or multi-shot measurements by tuning it in reverse angle.

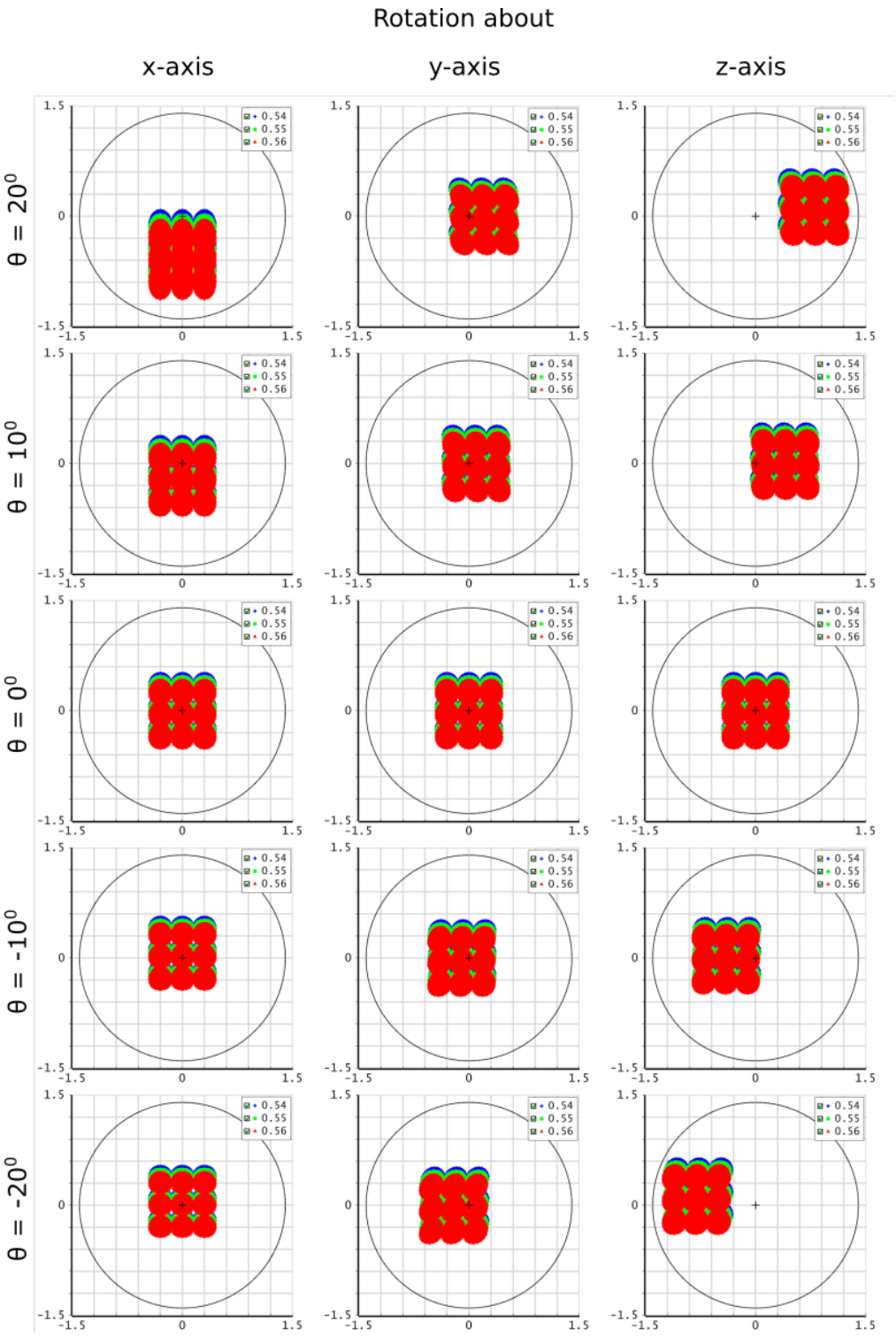

Figure 3.12: Simulated IFS response of the spot-diagrams by rotating the diffraction grating.

3.7 Summary

With the ABCD-EF formalism, an IFS is theoretically devised by the MLA-2F-G-2F and G-4F-MLA optical architectures. These designs realize the construction of the IFS by simultaneously obtaining both, spatial and spectral information. To verify the proof of concept, the design was simulated by Zemax ray tracing analysis. Geometrical bitmap image analysis was carried out with the design for three closely spaced wavelengths with 10 nm gaps. The point spread function was obtained by ray tracing of the centered wavelength, which was used in deconvolution to estimate the spectral distribution. Reconstruction with Wiener deconvolution gave promising results by retrieving the desired spectrum.

In the present approach, an attempt was made to improve the spatial resolution by a close spacing of microlens, which goes against conventional wisdom, where the spacing between the lenslets in large enough to accommodate the spectral range without causing overlap in the spectra of neighboring pixels to avoid crosstalk. In the current architecture, the densely packed microlens that results in crosstalk can be handled by reconstruction algorithms and optical diversity.

We investigated the influence of different optical elements regarding how they impacted the PSF of the image. Tuning of diffraction grating by pitch adds additional flexibility by mixing dispersion with neighboring microlens, which is one of the choices of diversity implementation. Another way to incorporate diversity is by rotating the diffraction grating along the z-axis. For future deployment of such systems, MEMS technology is a promising approach for achieving fine tuning. Design, fabrication, performance analysis and challenges of tunable diffraction gratings by micromachining technology are discussed in the subsequent chapters.

Chapter 4

Pitch tunable diffraction grating

4.1 Introduction

This chapter describes the design and development of a microelectromechanical systems based tunable diffractive element that could be deployed in the quasi-snapshot imaging spectrometer for diversity implementation. One candidate device for diversity implementation in the integral field spectrometer that is discussed in section 3.6.2.1 is a pitch tunable diffraction grating (PTG). Earlier approaches for tuning gratings have been by means of grating light valve [90], microfluidic actuation [85], piezoelectric actuation [88], electrostatic actuation [92, 93, 117], thermal actuation [91], and elastomeric actuation [87]. In the present work, electrostatic actuation is chosen, as it can work in a wide range of temperatures and pressures with low power, and can provide sufficient actuation range for the considered application.

The most common MEMS electrostatic actuators are limited by small displacement to a few micrometers. This is because an electrostatic comb-drive based actuator encounters pull-in instability when sufficiently high actuation voltages

are attempted [118]. This limits the maximum size of an electrostatic pitch tunable diffraction grating to about a few millimeters. Hence, more than scanning, the device is found to be useful in integrated computational imaging spectroscopy by making use of optical diversity techniques [119]. In such optical systems, several measurements with different optical transfer functions can be obtained by varying the pitch of the diffraction grating. Computational algorithms together with multiple distinct under-sampled images can be used to obtain a super-resolution image [120]. The desired resolution that needs to be achieved is related to reconstruction algorithms and the number of frames to be captured [121]. For such spectroscopic systems, large resolving power diffraction gratings with high fill factors are found to be advantageous.

The physical realization and analysis of the MEMS-based analog pitch tunable diffraction grating using silicon-on-insulator (SOI) technology are discussed in detail. The following sections describe the design, modeling, fabrication, and testing of the tunable grating. Further, the feasibility and mechanical robustness of the silicon micromachined PTG are investigated by subjecting it to mechanical vibrations.

4.2 Tuning mechanism principle

Light incident on the diffraction grating is dispersed according to the diffraction relation given by [122]:

$$\sin\theta^m + \sin\theta = \frac{m\lambda}{\Lambda} \tag{4.1}$$

where, θ is the incident angle, θ^m is the diffracted angle of order m, λ is the incident wavelength, and Λ is the pitch of the diffraction grating. The values of diffraction

order (m) are the set of integers and $m = 0$ gives the non-dispersive condition. The schematic working principle of a PTG is depicted in figure 4.1.

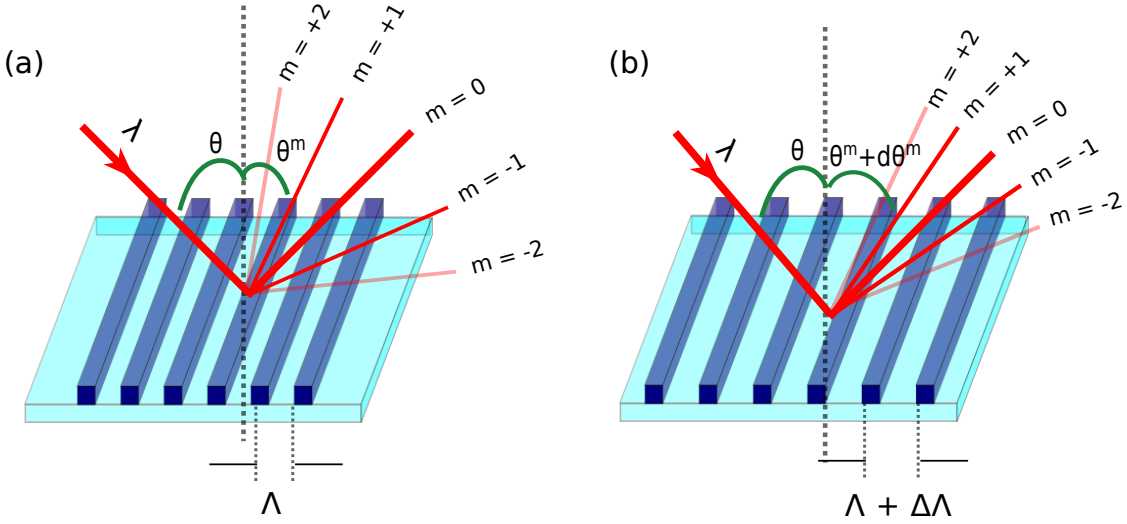

Figure 4.1: Schematic representation of the basic working principle of an analog pitch tunable diffraction grating: (a) before tuning, (b) after tuning.

Tuning can be incorporated by elongating or compressing the pitch, thereby changing the diffraction angle (θ^m). The pitch change of the diffraction grating from Λ to $\Lambda + d\Lambda$ leads to a change in diffraction angle, $d\theta^m$, which is given by

$$d\theta^m = \frac{m\lambda}{\Lambda^2} d\Lambda \tag{4.2}$$

where, $d\Lambda = (x/N)$ is the pitch change, x is the displacement achieved by actuation and N is the number of grating lines. It is evident that larger deflection provides better tuning range. However, larger deflection also leads to change in the duty cycle (DC), and a significant drop in diffraction efficiency (η), [123] expressed as

$$\eta = \left(\frac{\sin(2m\pi\ DC)}{2m\pi}\right)^2 + \left(\frac{1-\cos(2m\pi\ DC)}{2m\pi}\right)^2 \tag{4.3}$$

The DC in this context is defined as the ratio of beam width to the pitch.

Maximum efficiency of about 10 % is obtained when duty cycle is 50 %.

4.2.1 Micromechanical implementation

In the current design, the in-plane electrostatic comb-drive pair actuation mechanism was employed for its simplicity and relative ease of fabrication [124, 125, 126]. The schematic of the electrostatic actuation based PTG is depicted in figure 4.2. The grating grooves are implemented as a set of beams, which are supported by holding springs. The grating beams together with the holding springs are suspended by the actuating springs, which are connected to the anchors. The actuating springs are equipped with a comb-drive fingers structure that generates electrostatic force on application of voltage.

The electrostatic force generated by the comb-drive pairs can be modeled by a planar parallel plate capacitor [127]. This generated force is balanced by mechanical force, thereby effectively increasing the overlap area. The net electrostatic force generated by the comb-drive pairs consists of a combination of a pull-in force by the parallel plates, fringing fields (edge effects) and a ground-plane levitation force (between the suspended structure and the substrate). Neglecting the fringing fields and ground-plane levitation force, the capacitive force generated between the comb-drive pairs is given by [128]:

$$F_e = \frac{n\epsilon_0 t}{g} V^2 = F_m = k_{eff} x, \tag{4.4}$$

where, F_e is the electrostatic force, n is the number of comb fingers, ϵ_0 is the permittivity of free space, t is the thickness of the device, g is the separation between the parallel plates, V is the applied voltage, F_m is the mechanical force generated, k_{eff} is the effective spring constant of the structure, and x is the displacement ob-

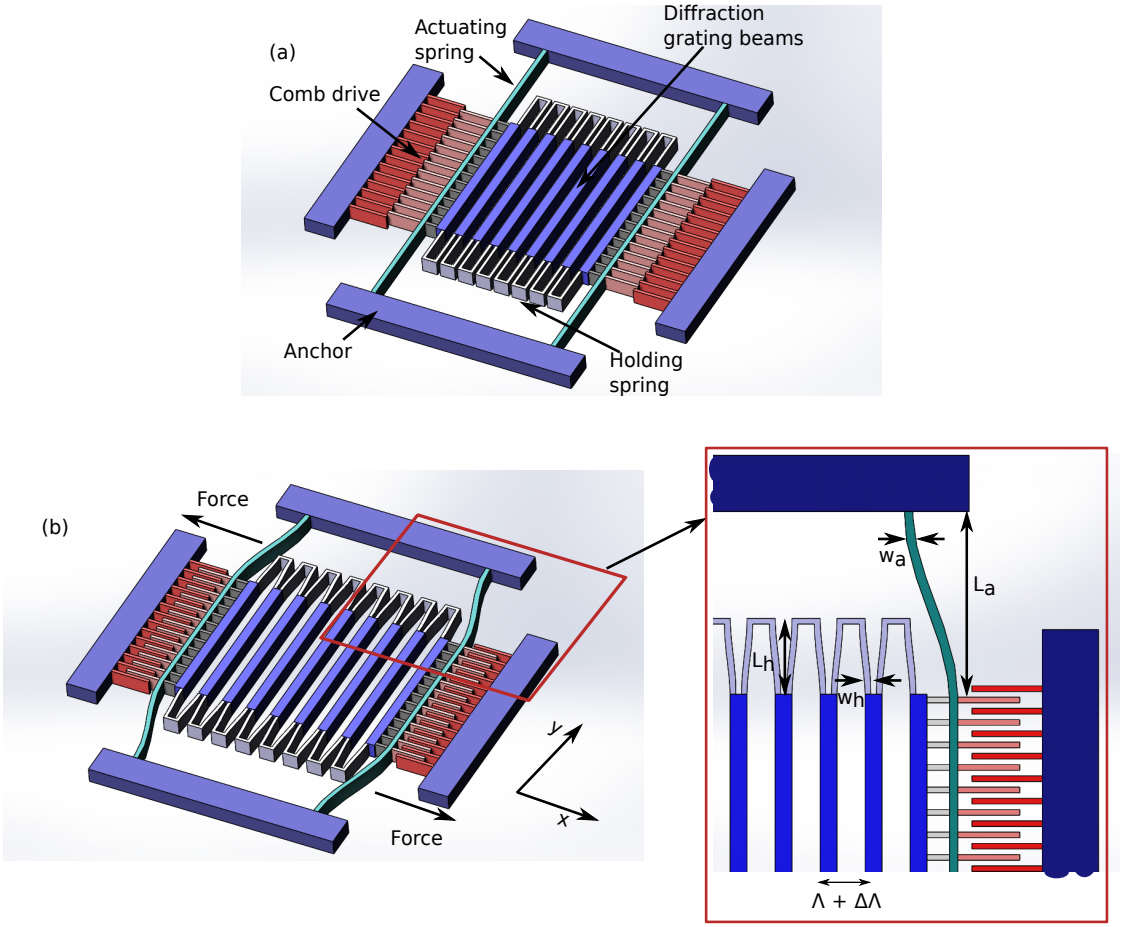

Figure 4.2: Schematic of tunable diffraction grating with electrostatic actuation: (a) before actuation; (b) after actuation.

tained. This force, in turn, pulls the actuating spring in the x direction to balance the electrostatic force. A larger tuning range can be achieved by increasing the actuation voltage.

4.2.2 Optical design

The intensity profile of a diffraction grating when N slits are illuminated by a collimated beam with normal incidence, can be obtained by [129]:

$$I = I_0 \frac{sin^2\left(\frac{N\pi\Lambda}{\lambda} sin\theta^m\right)}{sin^2\left(\frac{\pi\Lambda}{\lambda} sin\theta^m\right)} \frac{sin^2\left(\frac{\pi\Lambda}{2\lambda} sin\theta^m\right)}{\left(\frac{\pi\Lambda}{2\lambda} sin\theta^m\right)^2} \tag{4.5}$$

An important parameter that needs to be considered while designing the diffrac-

tion grating is the resolving power (R), defined as the number of grating lines (N) (*i.e.* for the first order diffraction). The resolving power of the diffraction grating for two wavelengths (λ_1 , λ_2) that are closely spaced is given by [129]:

$$R = \frac{1}{2}\frac{\lambda_1 + \lambda_2}{\lambda_1 - \lambda_2} = mN \tag{4.6}$$

The full width half maximum (FWHM) of the diffraction profile depends on N. Figure 4.3a shows the first order diffraction profile when a wavelength of 488 nm is incident on N slits. It is evident from the plot that FWHM reduces, *i.e.* resolution increases with an increase in N. The resolution also depends on the wavelength regime, which is depicted in figure 4.3b, where the number of grating lines is plotted against resolution for three wavelengths. Here the center wavelength and wavelength spacing are taken as $(\lambda_1 + \lambda_2)/2$ and $(\lambda_1 - \lambda_2)$, respectively. Further, it is evident that to obtain a spectral resolution less than 10 nm for a 632 nm wavelength in 1st order diffraction, there need to be a minimum of 64 grating lines.

4.2.3 Micromechanical design

The stiffness constant of the holding flexure can be derived by treating the flexure as a four guided cantilever structure. The expression for computing the stiffness value for a single holding spring with thickness t is obtained as [128]:

$$k_h^x = 12\frac{EI_h^x}{L_h^3}, I_h^x = \frac{1}{12}tw_h^3 \tag{4.7}$$

where, k_h^x is the holding spring stiffness in the x direction, E is Young's modulus, I_h^x is the moment of inertia of the holding spring, and $w_h(L_h)$ is the width (length) of the holding springs. The spring constant of the actuating spring can be treated

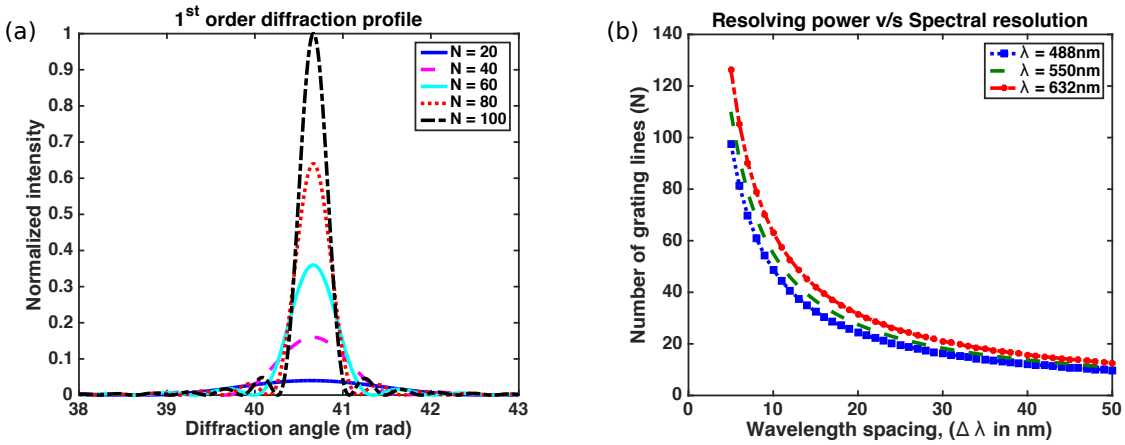

Figure 4.3: (a) Variation of the first order diffraction profile with the number of grating lines illuminated; (b) Plot depicting minimum number of grating lines for closely separated wavelengths in different wavelength regimes.

as a two guided beam structure connected in parallel. Accordingly, the spring stiffness value of the actuating arm in the lateral direction (k_a^x) for one-side is given by [128]:

$$k_a^x = 12\frac{EI_a^x}{L_a^3}, I_a^x = \frac{1}{12}tw_a^3 \tag{4.8}$$

where, k_a^x is the actuating spring stiffness in the x direction, I_a^x is the moment of inertia of the actuating spring and $w_a(L_a)$ is the width (length) of the actuating springs. The spring stiffness of the actuating arm in the y direction is computed as [128]:

$$k_a^y = \frac{Ew_at}{L_a} \tag{4.9}$$

where, k_a^y is the actuating spring stiffness in the y direction. The springs of the actuating arm are designed to provide maximum tangential displacement (minimum tangential stiffness, k_a^x) and minimum normal displacement (maximum normal stiffness, k_a^y). The stiffness ratio has to be large enough to avoid lateral pull-in

instability, which limits the actuation range of the device. It is derived from Eq. (4.8) and Eq. (4.9):

$$\frac{k_a^y}{k_a^x} = \left(\frac{L_a}{w_a}\right)^2 \tag{4.10}$$

For design considerations, the effective spring constant (k_{eff}) has to be computed first, followed by the evaluation of the other parameters. Yu *et al.* reported that the displacement of the comb-drive fingers drops significantly when the grating beams are connected with the actuating spring [130]. This discrepancy can be explained by a detailed analysis of the effective spring constant. The effective stiffness of the structure can be derived from the mass-spring model, which solely depends on actuating spring stiffness (k_a), holding spring stiffness (k_h), and the number of grating periods (N).

4.2.3.1 Mass-spring model

To compute the unknown effective spring constant (k_{eff} in Eq. (4.4)), the structure in figure 4.2 can be modeled as a mass-spring system portrayed in figure 4.4. The equivalent spring constant between two grating beams (k_{eq}) is the parallel

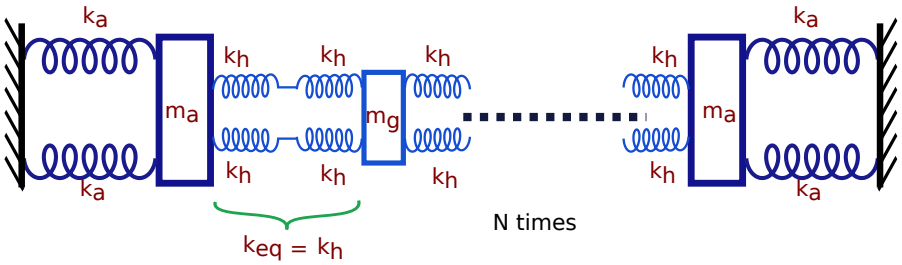

Figure 4.4: Schematic representation of equivalent mass-spring model of tunable diffraction grating structure.

combination of springs connected in series. The stiffness of a spring connected to

N beams can be computed as a combination of N springs of individual stiffness k_{eq} $(= k_h)$ connected in series. The force generated from the comb-drives on either side of the device pulls the first $(N/2)$ grating beams in one direction and the remaining beams in the other direction to obtain maximum tuning range. The effective spring constant of the structure when electrostatic force is applied in both directions can be computed as

$$k_{eff} = 2k_a + \left(\frac{2}{N}\right) k_h \tag{4.11}$$

After obtaining k_{eff}, the remaining parameters (L_h, L_a, w_h, w_a) are chosen based on the fabrication constraints. The length of the grating beams is chosen to have an effective diffraction area of 1 mm × 1 mm. The minimum feature size of the structure is selected as 2 µm, which is the critical dimension for photolithography. The design values are summarized in table 4.1.

4.2.3.2 In-plane modal analysis

The in-plane mechanical resonant frequencies of the PTG are computed using a mass-spring model for stability analysis. The natural frequencies of the mass-spring system can be derived by equations of motion for an undamped linear system using

$$\mathbf{M}\frac{d^2x}{dt^2} + \mathbf{K}x = 0, \tag{4.12}$$

where, x is the time dependent vector that describes the motion, $\mathbf{M}$ is the mass matrix and $\mathbf{K}$ is the stiffness matrix given respectively by

$$\mathbf{M} = \begin{bmatrix} m_a & 0 & 0 & \dots & 0 & 0 \\ 0 & m_g & 0 & \dots & 0 & 0 \\ 0 & 0 & m_g & \dots & 0 & 0 \\ \vdots & \vdots & \vdots & \ddots & \vdots & \vdots \\ 0 & 0 & 0 & \dots & m_g & 0 \\ 0 & 0 & 0 & \dots & 0 & m_a \end{bmatrix}$$

$$\mathbf{K} = \begin{bmatrix} 2k_a + k_h & -k_h & 0 & \dots & 0 & 0 \\ -k_h & 2k_h & -k_h & \dots & 0 & 0 \\ 0 & -k_h & 2k_h & \dots & 0 & 0 \\ \vdots & \vdots & \vdots & \ddots & \vdots & \vdots \\ 0 & 0 & 0 & \dots & 2k_h & -k_h \\ 0 & 0 & 0 & \dots & -k_h & k_h + 2k_a \end{bmatrix}$$

where, m_a is the sum of the mass of the actuating arm and the mass of comb fingers attached to it, m_g is the sum of the mass of the grating beam and the four supporting holding beams, k_a ($=k_a^x$) is the actuating spring stiffness along the x direction, and k_h ($=k_h^x$) is the holding spring stiffness along the x direction. The theoretical values calculated to be m_a $=5.728 \times 10^{-10}\,\mathrm{kg}$, m_g $=1.635 \times 10^{-10}\,\mathrm{kg}$, k_a $=0.266\,\mathrm{N\,m^{-1}}$ and k_h $=5.084\,\mathrm{N\,m^{-1}}$ respectively. To find the harmonic solution, it is assumed that x takes the from $X\sin(\omega t)$, which results in

$$-\mathbf{M}X\omega^2 \sin\omega t + \mathbf{K}X \sin\omega t = 0 \tag{4.13}$$

On further simplification, the above equation gives $\mathbf{K}X = \omega^2\mathbf{M}X$. The generalized eigenvectors are given by substituting vector v and λ in the above equation, giving $\mathbf{K}v = \lambda\mathbf{M}v$. The eigenvalue solution, λ, is computed by MATLAB for $\mathbf{M}$ and $\mathbf{K}$ (code described in appendix C.2). The natural frequency of the system for

the i^{th} eigenvalue is then

$$f_i = \frac{1}{2\pi}\sqrt{\lambda_i} \tag{4.14}$$

The analytical model for structural analysis and resonant frequency is validated by 3D finite element method (FEM) simulations (ANSYS). The simulated result is depicted in the figure 4.5. It is found that the in-plane resonant frequency simulated with FEM is in agreement with the theoretical value of 889 Hz. FEM structural analysis is also carried out to make sure that stress distribution is far less than the yield strength of Si, before proceeding to the fabrication.

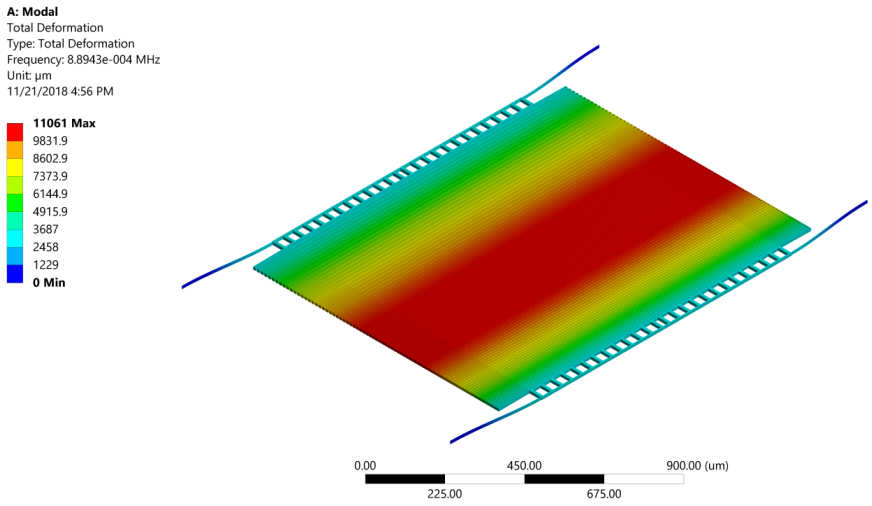

Figure 4.5: FEM modal analysis performed to calculate the resonant frequency of the structure

4.3 Microfabrication

The fabrication of the device was performed using surface micromachining technology on a 100 mm diameter SOI wafer with 10 µm device layer thickness, 2 µm buried oxide, 450 µm handle layer, <100> crystal orientation, boron doping and a resistivity between 1 Ω cm to 20 Ω cm. The wafer was initially cleaned with piranha

solution for 20 min at 120 °C and rinsed using de-ionized (DI) water. The wafer was spin-dried and then placed on a hot plate at 110 °C for 30 min to make the surface dehydrated. Before performing the spin coating, the wafer was treated with hexamethyldisilizane (HMDS) primer for 120 s to make the surface hydrophilic, thus improving the adhesion of photoresist with the wafer. A brief schematic representation of the fabrication process is depicted in figure 4.6.

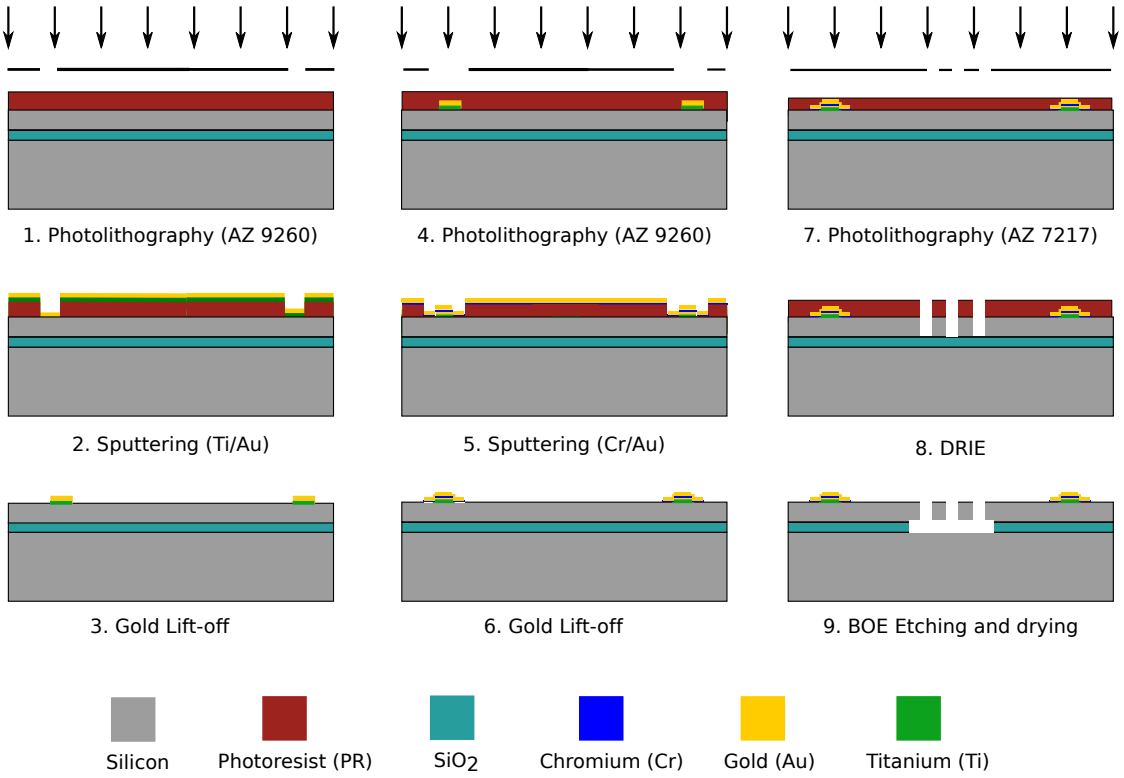

Figure 4.6: Schematic representation of the fabrication of tunable amplitude diffraction grating.

In the first step, the wafer was spin coated with AZ-9260 photoresist (MicroChem) at 5000 rpm for 30 seconds to obtain a uniform thickness of 4.2 µm. The wafer was soft baked for 4 min at 110 °C on a leveled hotplate. Subsequently, photolithography was performed using mask aligner (Karl Suss MA-6) with contact mask exposure. After exposure to UV light (365 nm), the exposed part was

removed by 400 MIF (Metal-Ion-Free) developer solution and dried with a nitrogen gun. Afterwards, the wafer was sputtered with Titanium (Ti)/ Gold (Au) (20 nm/50 nm), followed by lift-off by immersing the wafer in acetone (steps 1-3 in figure 4.6). Ti serves as the adhesion layer between Si and Au.

To protect the Ti from buffered oxide etchant (BOE) [131] in the later steps of fabrication, photolithography was continued with the same process parameters with a mask having a bigger pad-size. Subsequently, it was sputtered with Chromium (Cr)/ Gold (Au) (20 nm/400 nm) on top of the existing pads, thereby, ultimately covering the Ti layer, and after that, lift-off was performed (steps 4-6 in figure 4.6). Cr/Au acts as the contact pads for external electrical connection for providing voltage.

With the third mask, photolithography for the PTG structure was carried out with a low viscosity photoresist AZ-7217 (MicroChem). The photoresist was spin coated at 5000 rpm for 30 s obtaining a layer of 1.1 µm thickness, which was followed by soft baking at 100 °C for 90 s. After cooling down the resist, photolithography was performed in vacuum mode for 3.4 s. After exposure, the wafer was post baked for 2 min at 110 °C and allowed to cool down to room temperature. The exposed regions were removed by 300 MIF (MicroChem) developer solution. After drying the wafer, hard baking of another 2 min was carried out at 110 °C, followed by Deep Reactive Ion Etching (DRIE), Bosch process to obtain nearly vertical walls. Etching was continued till it reaches the SiO_2 layer. Finally, the sacrificial oxide layer beneath the structure was removed by BOE solution (steps 7-9 in figure 4.6).

The primary challenge during drying after oxide etching was the stiction between adjacent grating beams and also in the holding springs due to the surface

tension between water and the device. This resulted in damage to the devices. Figure 4.7 shows the damaged devices that arised due to stiction.

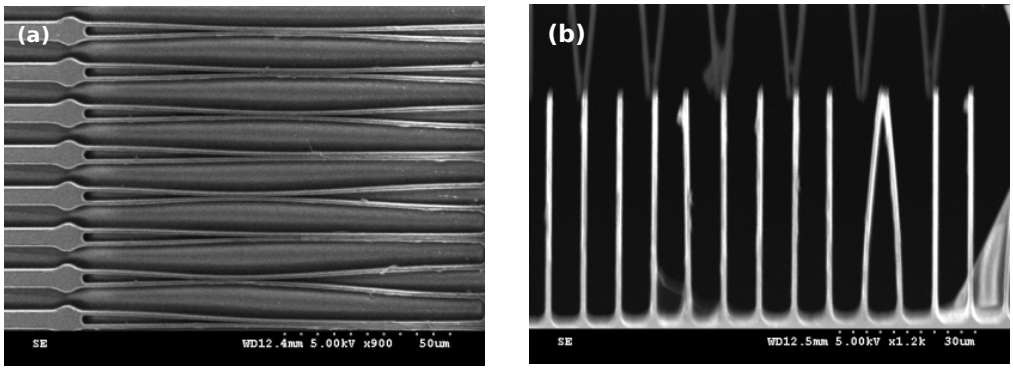

Figure 4.7: SEM images of the damaged device caused due to stiction in (a) holding springs; (b) comb fingers.

To overcome this problem, super critical CO_2 drying process was adopted (Automegasamdri Model: 915B). The wafer was kept inside isopropanol solution (IPA), and during the process, IPA was replaced by liquid CO_2. By this method, the wafer was dried with liquid CO_2 under critical point temperature and pressure, by which the physical properties of gaseous and liquid states remain unchanged. The SEM images of the fabricated device are depicted in figure 4.8.

4.4 Device characterization and testing

It was observed that device performance was dependent on microfabrication tolerances. With the conditions of the DRIE system that was employed, etching produces a negatively sloped profile in the beams where the trench space was large and a positive profile where trenches were closely spaced. This resulted in a negative etching profile near the comb-fingers (figure 4.9a) and a positive etching profile near actuating springs (figure 4.9b).

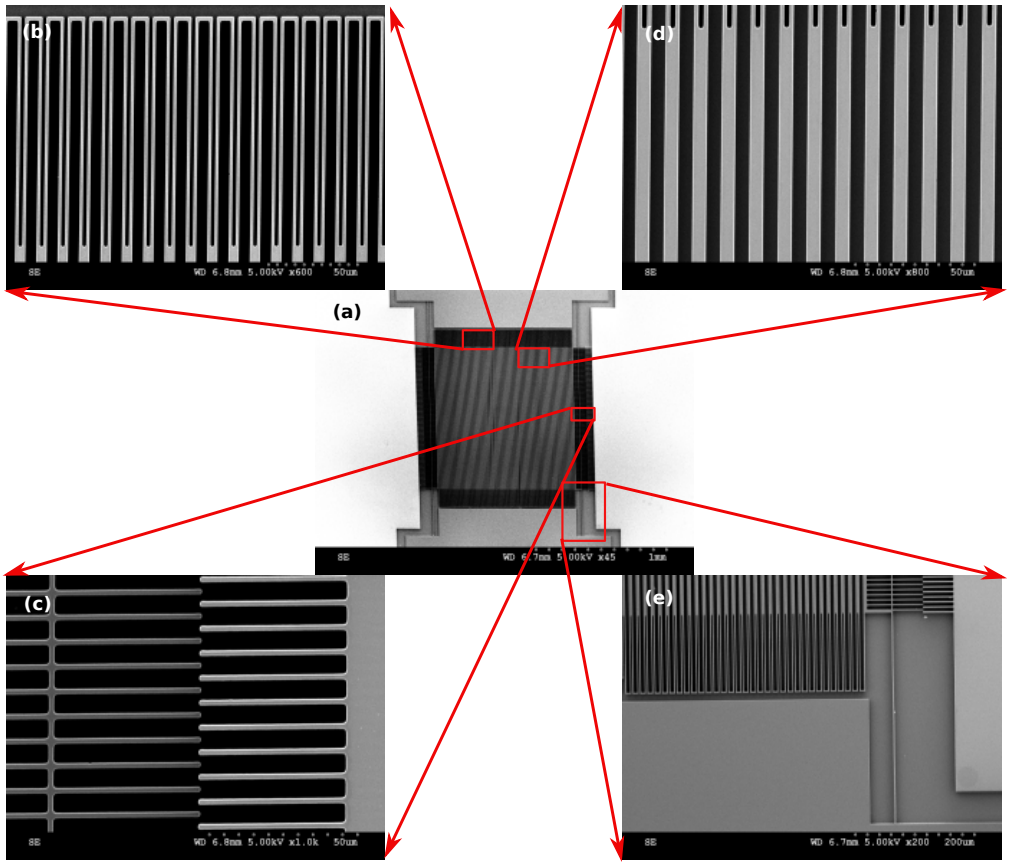

Figure 4.8: SEM images of the fabricated MEMS diffraction grating (a) device; (b) holding springs; (c) comb-drive fingers; (d) grating beams; and (e) actuating spring.

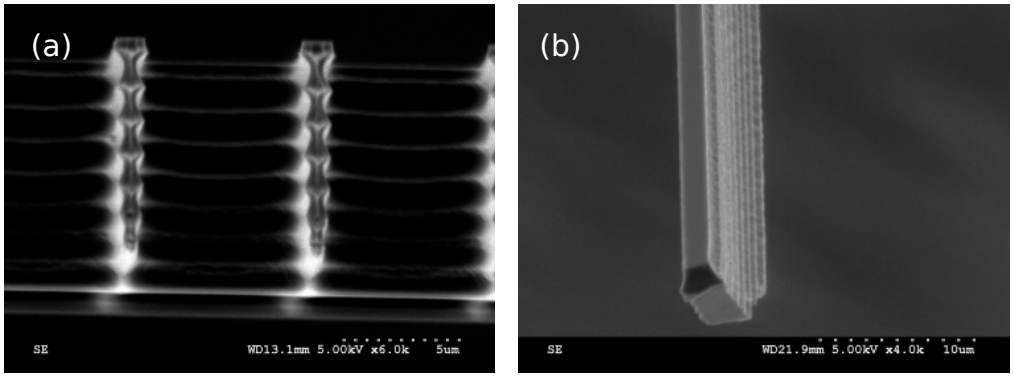

Figure 4.9: (a) Negative tapered profile on comb-fingers, (b) positive tapered profile of the actuating spring.

A similar trend was also reported by other researchers [132, 133, 134]. This non-uniformity in the etching profile might result in relatively considerable variation in the expected device performance [135]. A comparison between the designed values from the analytical modeling and the fabricated values is shown in table 4.1.

Table 4.1: Comparison of designed and measured values of parameters of the microelectromechanical system (MEMS) pitch tunable diffraction grating.

Device Parameters	**Symbol**	**Designed** (µm)	**Measured** (µm)
grating beam length	L_g	1000	1000
grating beam width	w_g	6	5.9
grating pitch	Λ	12	12
device thickness	t	10	10
holding spring length	L_h	122	122
actuating spring length	L_a	333	333
comb finger length	L_c	50	50
holding spring width	w_h	2	1.9 (top)
			2 (bottom)
actuating spring width	w_a	2	1.7 (top)
			2.7 (bottom)
comb finger width	w_c	2	1.4 (top)
			0.8 (bottom)
initial overlap distance	x_0	2	1.8
Device Parameters	**Symbol**	**Designed**	
No. of grating beams	N	84	
No. of comb fingers	n	125	

An attempt to evaluate the performance analysis of such etching profiles has been carried out in [136]. Hence, based on the fabricated structure, we modified the analytical modeling to predict the expected performance. This is due to the change in the electrostatic force and the spring stiffness. The expected changes in the performance parameters based on the etching profile are analyzed and described in appendix B. Based on the modified design, the displacement of the actuator can be computed from Eq. (B.2) and Eq. (B.6) and given by:

$$x = \frac{F_{(new)}}{k_{eff(new)}} = \frac{n\epsilon_0 V^2}{2Et\tan\theta} \frac{\log\left(1 + 2\frac{t}{g}\tan\theta\right)}{\frac{2}{L_a^3}\left(w_a + t\tan\phi\right)^3 + \frac{2}{NL_h^3}\left(w_h + t\tan\psi\right)^3} \tag{4.15}$$

where, θ, ϕ and ψ are the etching profile angles in comb-drive fingers, actuating springs and holding springs, respectively. The spring stiffness with the modified design is calculated to be $1.56\,\mathrm{N\,m^{-1}}$, against the initially designed value of $0.94\,\mathrm{N\,m^{-1}}$. Further, the negatively tapered etching profile in the comb-drives leads to a reduction in the electrostatic force from 8.8 µN to 4.6 µN for a driving voltage of 40 V.

4.4.1 Static measurements

The fabricated PTG was tested in a probe station by observing the deflection of the grating beams with the applied voltage. Figure 4.10a,b depict the tuning of PTG without and with the driving voltage, along with the difference between the two images. The inset in figure 4.10c shows a line profile along the white dashed line in the two images of the grating.

Stretching of the grating beams was achieved by moving the comb fingers during actuation. The displacement obtained in the comb fingers is plotted with respect

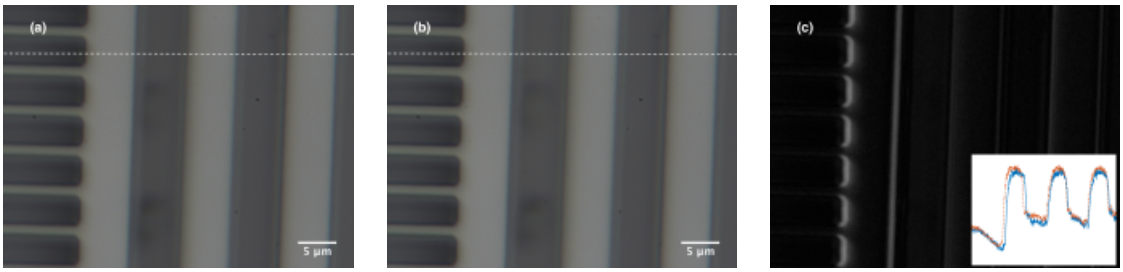

Figure 4.10: Optical microscope images of the grating beams (a) before the application of voltage; (b) during the application of voltage; and (c) difference between the two images (the inset shows a line plot along the dashed line in (a, b)).

to the voltage in figure 4.11. The plot shows that displacement follows a quadratic relation with the applied voltage and also that the measured values match with the modified design.

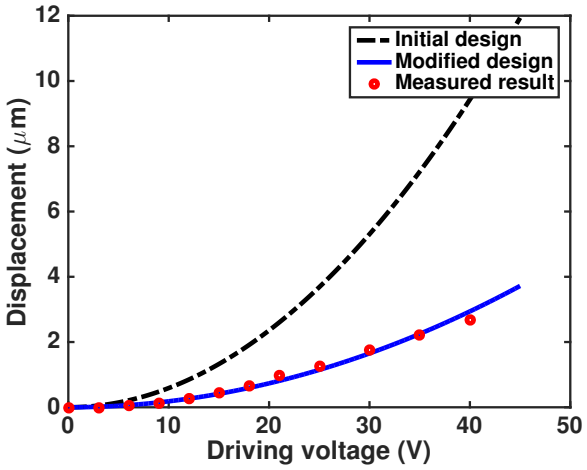

Figure 4.11: Displacement obtained in pitch tunable diffraction grating (PTG) plotted against voltage.

For safe working of the device, the driving voltage has to be less than the pull-in instability voltage [127], which is given by:

$$V_{PI} = \frac{g^2 k_a^x}{2\epsilon_0 w_a n}\left(\sqrt{2\frac{k_a^y}{k_a^x} + \frac{x_0^2}{g^2}} - \frac{x_0}{g}\right) \tag{4.16}$$

Since the design has higher stiffness ratio (k_a^y/k_a^x in Eq. (4.10)), and the operating voltage was far less than the pull-in voltage, the device does not face any lateral pull-in instability. However, it was observed that the device get sticked to the handle layer of the wafer when higher driving voltages were attempted. This can be rectified by modifying the fabrication steps by incorporating additional photolithography on the handle layer followed by etching.

4.4.2 Optical characterization

The fabricated grating was also tested optically. The PTG was illuminated with a laser beam of wavelength 488 nm, and the diffraction pattern was observed on a dark screen that is shown in figure 4.12a.

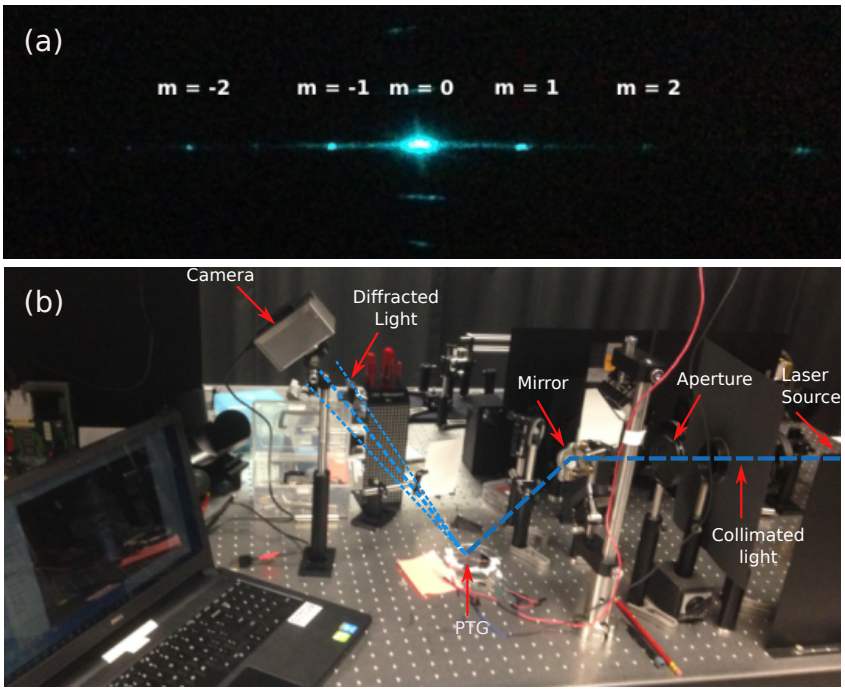

Figure 4.12: (a) Diffraction pattern obtained with a 488 nm laser beam incident on the PTG; (b) Experimental set-up to calculate the shift in diffraction order with tuning.

To validate the shift in the diffracted angle, the 1^{st} order diffraction spot (m = +1) was detected on a camera. The experimental set-up is depicted in figure 4.12b. Further, a voltage of 40 V was applied through the contact pads; and the resulting shift in the first order diffraction was measured to be four pixels. The shift in the camera pixels were calculated by centre of mass method. This corresponds to a change of 218 µrad in the diffraction angle.

A comparison of our PTG with those of other research works is shown in table 4.2.

Table 4.2: Performance analysis of the PTG with those of other works.

Reference	**Actuation mechanism**	**Resolving power**	**Fill factor**	**Actuation voltage**	**Displacement**
Author (year)		$(\frac{\lambda_0}{\delta\lambda})$	(Effective area/Total area)(%)	(V)	(µm)
Shih *et al.* (2006) [92]	Electrostatic	17	20	10	0.46
Yu *et al.* (2010) [93]	Electrostatic	30	22	70	10.4
Yu *et al.* (2010) [130]	Electrostatic	29	≈10	100	21
Tormen *et al.* (2006) [117]	Electrostatic	33	≈ 30	100	2
Yang *et al.*(2008) [91]	Thermal	54	≈ 21	19	300
Wong *et al.* (2003) [89]	Piezoelectric	-	-	10	≈ 0.28
this work	Electrostatic	84	52	40	2.7

4.4.3 Mechanical vibration test

MEMS devices are more susceptible to mechanical shock and vibrations. To measure the level of shock, a transient structural FEM simulation was performed with different shock levels. The simulations were carried out with the same geometry and designed values given in table 4.1. Anisotropic silicon was chosen as the material for all the simulations. In one simulation, a shock of 5 G was applied along the weakest out-of-plane direction of the PTG. The value 5 G is chosen because it is the maximum level of shock experienced in most of the satellite based missions [137, 138]. The simulation result showed that maximum stress was concentrated on the actuating springs and there was no significant stress in the optical grating region (figure 4.13). The result also showed that maximum principal stress was 4.15 MPa, far less than the fracture strength of silicon (7000 MPa).

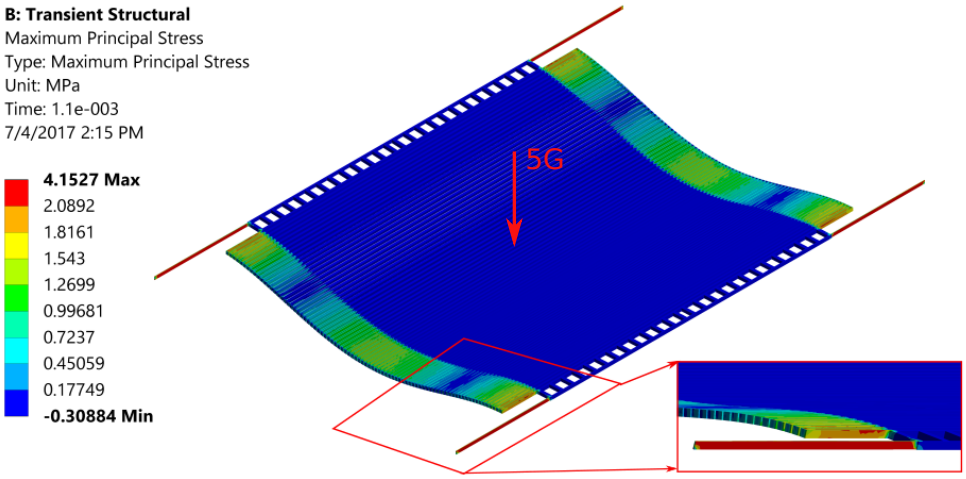

Figure 4.13: Stress distribution in the structure when subjected to a shock of 5 G.

Mechanical strength of the device was also studied by subjecting it to mechanical vibrations. The first out of plane resonant frequency obtained from the

simulations was found to be 230 Hz. Hence, it is important to make sure that the natural frequency of the device does not fall within the range of this value, leading to fracture of the device. To verify that the PTG is not susceptible to vibrations; vibration test using a mini-shaker was carried out by varying its frequency using a function generator. The amplitude of excitation was controlled by increasing the voltage in the function generator. It was also observed that the amplitude of excitation reduces with an increase in frequency. The vibration response of the mini shaker was measured by a laser displacement sensor, and the corresponding amplitude-frequency plot is shown in figure 4.14a. In-plane vibrations and out-of-

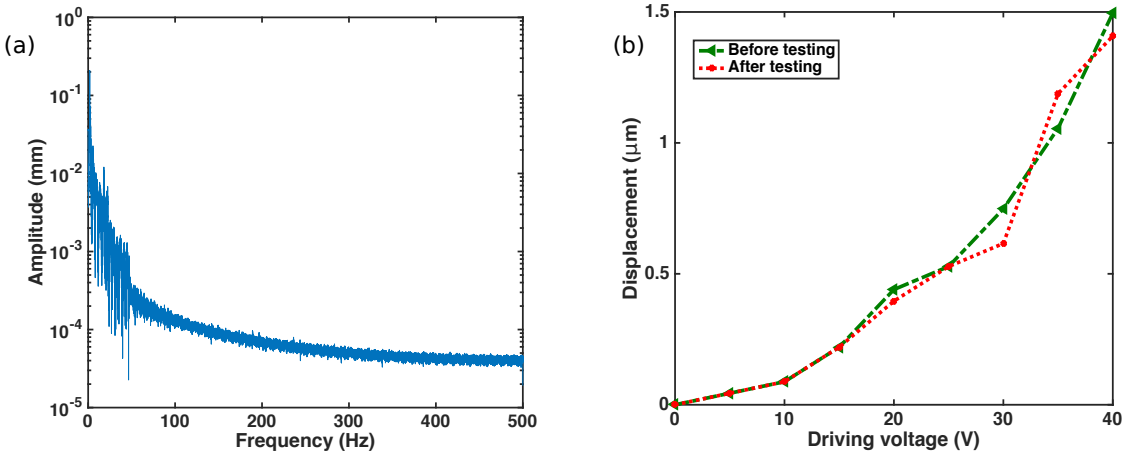

Figure 4.14: Vibration test analysis of the PTG with (a) frequency response of vibrations, measured using laser displacement sensor; (b) Performance of our device measured experimentally before and after the vibration test.

plane vibrations were performed by placing the device in different orientations. A different device was used for vibration testing to avoid damaging the best device. The process runs for 1 h and no mechanical failure of the structure is observed. After undergoing the vibration test, the device was evaluated in a probe station.

Figure 4.14b shows the displacement-voltage relation of the device before and after the test.

4.5 Summary

A silicon-based pitch tunable diffraction grating was designed and fabricated using micromachining technology. Detailed analytical modeling was carried out for the PTG using a mass-spring model. The device was built with a 10 µm thick SOI wafer. Micro-mechanical performance of the fabricated structure with the modified design was analyzed. The tuning produced a displacement of 2.7 µm for an actuation voltage of 40 V. With the application of different voltages, displacement was found to follow the expected quadratic law, in good agreement with the nominal parameters. The diffraction grating was tested on an optical bench by applying actuation voltage to observe the positional shift in the diffraction orders. Finally, the device was subjected to vibration tests to study its reliability.

Chapter 5

Rotary diffraction grating

5.1 Introduction

Tuning by means of changing the grating pitch was investigated in chapter 4. However, the main limitation of pitch tunable grating using silicon micromachining is the fabrication difficulties to achieve small grating pitch. Another challenge is to make a big device with large dynamic range. Further, fabrication of bigger device results in increase in mass of the structure, which leads to drop in resonant frequency. In addition to that, for pitch tunable grating, majority of the space is utilized for the actuation springs resulting in reduced fill factor. In terms of optical performance, a shift in the dispersion angle by electrostatic tuning has a dynamic range of only a few hundreds of micro-radians. Finally, the maximum theoretical diffraction efficiency possible for such binary amplitude grating is less than 10 %. To overcome these hurdles, a new method of tuning the grating is proposed by means of rotation.

Fabrication of a good in-plane rotational actuator together with a highly effi-

cient diffraction grating would overcome these problems. The optical element will be integrated with the actuator thus preserving the advantages/performance of the actuator as well as the optical quality. The rotary actuator is fabricated by silicon micromachining technology and diffraction grating by replication techniques. Since the diffraction grating is to be bonded on top of the actuator covering the flexures, the fill factor would be significantly enhanced.

The micromachined rotary motor is designed with 3-phase electrostatic stepper motor principle. Stepping motion allows move and hold precise motion that enables use in imaging applications with conventional CCD or CMOS cameras, where the frame rates are slow. The electrostatic micromotor is fabricated by a frictionless bearing mechanism to avoid contacts that result in wear and tear. The diffraction grating is fabricated on top of SU-8, a negative photoresist, using replication technique followed by photolithography to obtain the desired shape and to bond with the microactuator. Diffraction grating realization with replication could fabricate blazed angle grating, that significantly improves its diffraction efficiency [139, 140, 141]. Micro-scaled blazed diffraction grating can be made on SU-8 with master mold. The replicated diffraction grating is later bonded with the microactuator using UV curable optical glue. This structure would serve as one of the possible ways of achieving optical transfer function diversity in quasi-snapshot imaging spectrometer.

5.2 Tuning of grating by rotation

5.2.1 Working principle

Rotation of diffraction grating introduces change in the dispersion orientation. When a broadband light is illuminated onto a diffraction grating, the light splits into individual wavelength based on the grating period and grooves inclination. Smaller period (large number of grating-lines/mm) of the diffraction grating results in larger angular dispersion and vice versa. In case of rotation, dispersion direction will change, resulting in different mixing of overlap signals, as mentioned in section 3.6.2.2. Effect of dispersion by diffraction grating rotation is schematically presented in figure 5.1.

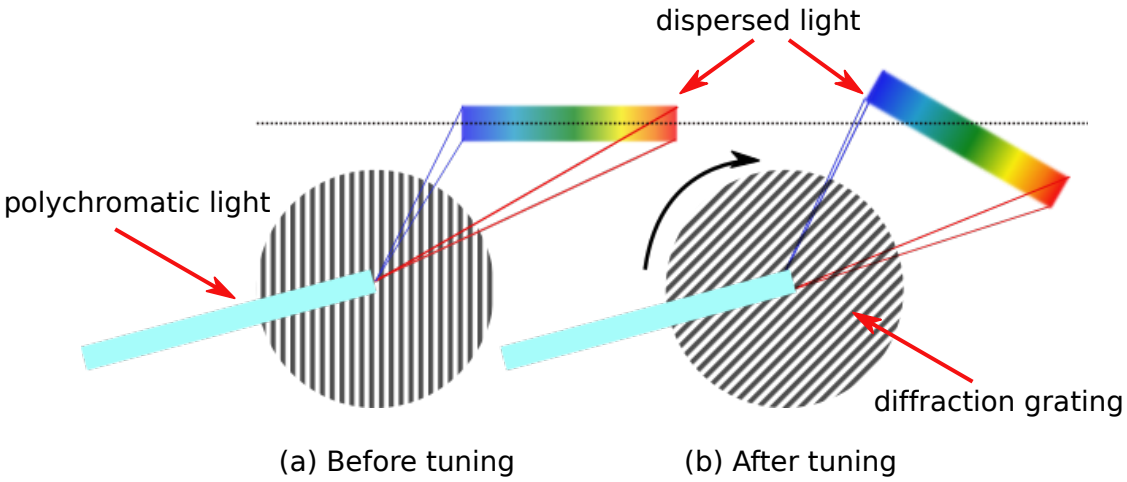

Figure 5.1: Schematic working principle of the rotational diffraction grating to change the direction of dispersion when illuminated by a broadband light source.

5.3 Electrostatic rotary stepper motor

The design of rotational actuator for driving optical elements is inspired by butterfly flexural pivot invented by the Swiss Center for Electronics and Microtechnology (CSEM) (figure 5.2) [142]. The structure has a nearly perfect combination of a

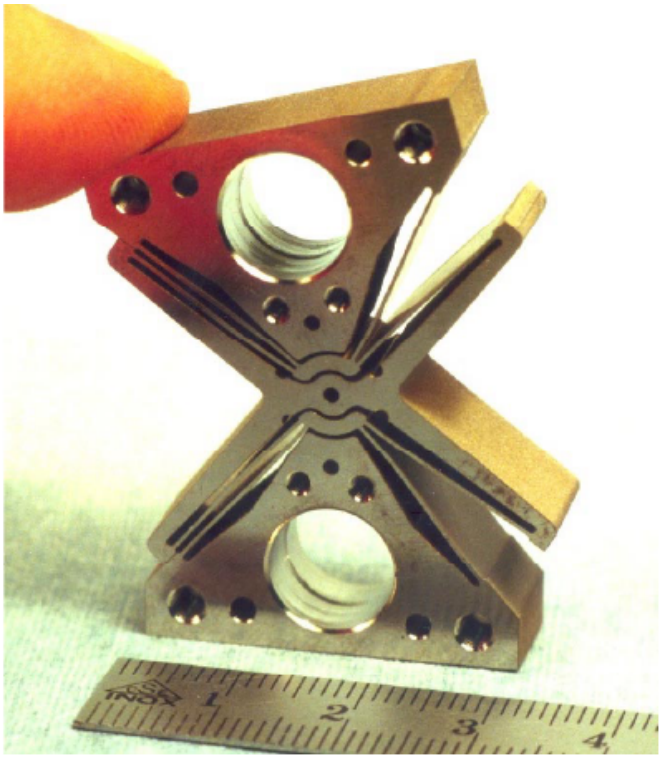

Figure 5.2: Butterfly pivot structure designed by CSEM [101].

large deflection angle and a high precision. The butterfly pivot structure is found to possess lateral stiffness, thereby providing very small center shift [143]. Planar design allows monolithic manufacturing, and can be easily implemented on silicon micromachining technology. Folded architecture provides larger angular rotation, resulting in wide tunability. The structure posses a mechanical end stop that limits angular rotation. Apart from all these features, the structure has high radial, axial and angular transverse stiffness.

Previously, there were some similar attempts to fabricate MEMS device drawing

inspiration from flexural pivot structure [144, 103]. In this work, the design is modified to incorporate the diffraction grating on to the microstructure as depicted in figure 5.3.

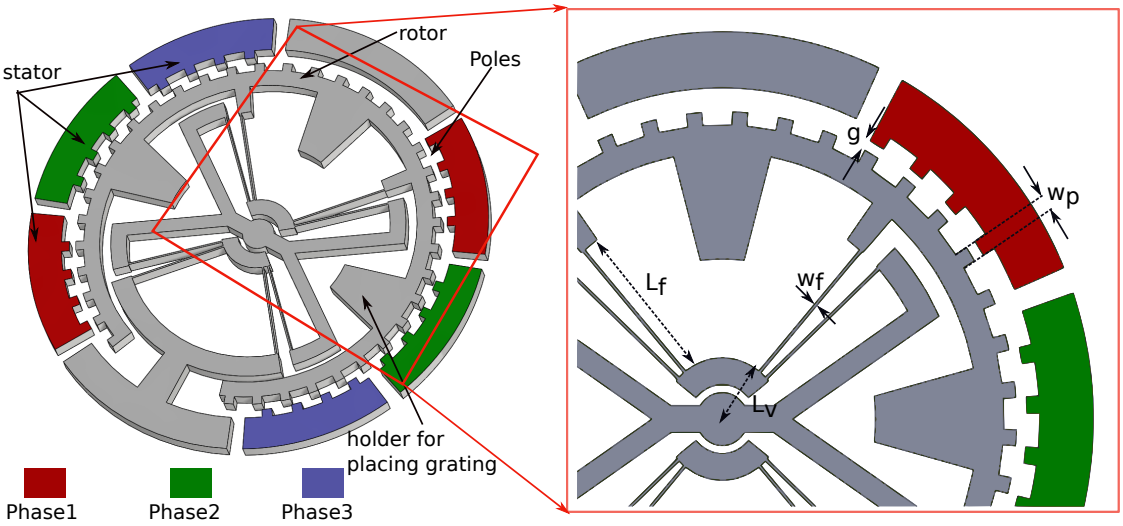

Figure 5.3: Schematic depiction of electrostatic 3-phase rotary actuator.

The schematic of stepper motor based microactuator with the integrated diffraction grating is depicted in figure 5.4. The structure works on the principle of 3-phase stepper motor mechanism by exciting rotor and stator poles. The device is designed with flexure mechanism having two four-beam pivot structures connected in series. The advantage of having frictionless flexure allows going back to the reference position when the signal is removed, which is advantageous in imaging spectrometer design. The four-beam pivot structure attached to the rotor provides a maximum angular rotation of 30° (±15°). In total, the structure consists of three pairs of stators and the grounded rotor. Each pair of the stator phase is placed diametrically opposite to each other to avoid pull-in instability. The poles of phase-1 are perfectly aligned with rotor poles. The poles of phase-2 and phase-3

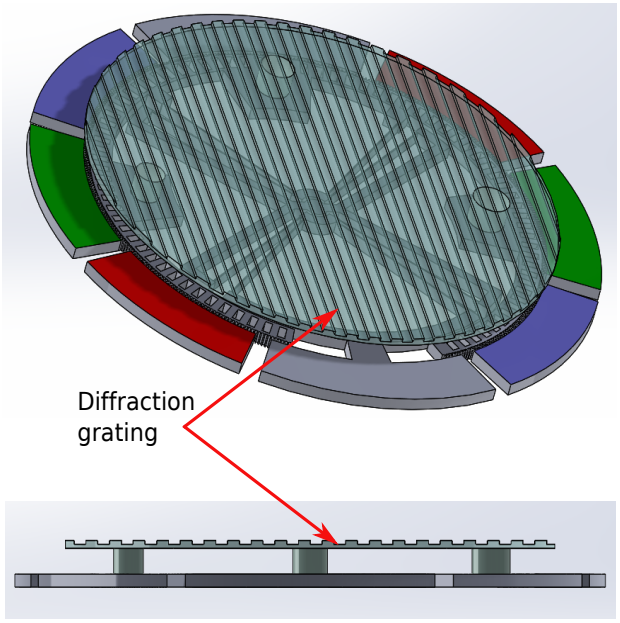

Figure 5.4: Schematic of diffraction grating integrated on top of the actuator device for rotational tuning.

are misaligned by $(1/3)^{rd}$ and $(2/3)^{rd}$ of the rotary pitch, respectively.

The stator phases are independently excited by voltage waveform, thereby generating torque to achieve the desired rotation. Applying a voltage to the three phases generates an electrostatic force between the stator and the rotor poles. This will re-align the rotor poles with the stator poles to compensate the generated electric field. At the next time instant, the adjacent phase is excited and the rotor will again re-align its poles to the corresponding excited stator-poles. Hence, at each time instants, only one-third of the rotor poles are aligned with the stator poles. To obtain sub-steps, half-stepping or micro-stepping voltage sequence can be employed. Micro-stepping provides a gradual transition in switching voltage levels and leads to the smooth running of the motor with better positioning resolution.

5.3.1 Micromechanical design

The electrostatic actuation of the rotor can be treated similar to a force between parallel plate capacitor. In this regard, the angular displacement is produced by the tangential force (or electrostatic torque) acting on the electrode poles. The expression for computing electrostatic torque ($\mathcal{T}_e$) is given by [99]:

$$\mathcal{T}_e = \frac{n\epsilon_0 rt}{2g} V^2 \tag{5.1}$$

where, n is the number of active poles in a phase, ϵ_0 is the permittivity of free space, r is the radius of the rotor, t is the thickness of the rotor, g is the separation between the rotor and the stator electrodes, and V is the actuation voltage. The electrostatic torque is proportional to the rotation angle (θ) defined by the angular stiffness

$$\mathcal{K}_\theta = \frac{\mathcal{T}_e}{\theta} \tag{5.2}$$

The expression for rotational stiffness of the butterfly pivot structure is derived in [145], and the final expression obtained is

$$\mathcal{K}_\theta = 2\frac{EI}{L_f}\left(1 + 3\frac{L_v}{L_f} + 3\frac{L_v^2}{L_f^2}\right), \qquad I = \frac{1}{12} t w_f^3 \tag{5.3}$$

where, E is the Young's modulus of the material, I is the moment of inertia, w_f is the width of the flexure beam, L_f is the length of the flexure, and L_v (illustrated in figure 5.4) is the virtual length from centre of the flexure bearing to the flexure beam. Multiple designs are incorporated in the masks by varying the these parameter values as described in table 5.1 for the micro stepper motor fabrication.

Table 5.1: Design values of the rotary actuator used in mask drawing.

Device Parameters	**Symbol**	**D-1**	**D-2**	**D-3**	**D-4**
radius	r (µm)	700	800	900	1000
flexure length	L_f (µm)	400	500	600	700
flexure width	w_f (µm)	3	4	4	5
pole width	w_p (µm)	5	4	5.15	5
number of active poles	n	60	76	76	88
device thickness	t (µm)	50	50	50	50
gap separation	g (µm)	3	3	3	3

5.3.2 Finite element analysis

Before proceeding to the microfabrication, finite element analysis (FEA) based Ansys simulation was performed to confirm that the maximum principal stress is far below the yield strength of silicon. The static structural analysis was performed for the designed micormotors by applying tangential force (24.9 µN) to obtain the stress distribution. The stress distribution profile is depicted in figure 5.5a. The maximum principle stress was found to be 79 MPa which is fas less than the fracture strength of the Si.

Modal analysis was also carried out, which shows that the first resonant frequency was in the range of a few hundred Hertz, and the first and second resonant modes were in in-plane directions. The modal analysis performed in Ansys for the first resonant mode is depicted in figure 5.5b. One of the greatest advantages of this structure, when compared to other rotational based actuator realized with MEMS technology is that the first resonant mode is not in the out of plane direction, which

is not desirable for the optical imaging design.

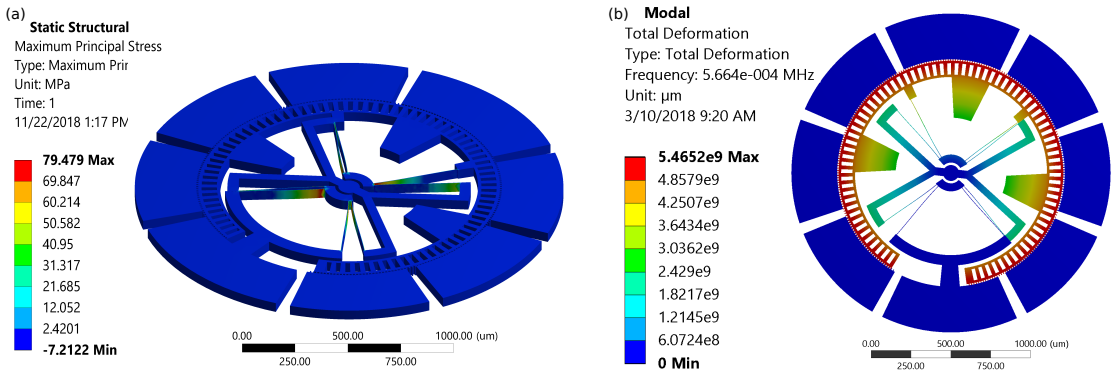

Figure 5.5: FEM analysis of the butterfly pivot structure showing the (a) stress profile; (b) modal analysis for determining resonant frequency.

5.3.3 Microfabrication

Microfabrication of the device involved two processes: fabrication of the actuator and fabrication of the diffraction grating. The schematic representation of fabrication of the microactuator is shown in figure 5.6. The device was fabricated on an SOI wafer with device layer thickness 50 µm, $< 100 >$ orientation, p-doped, 0.01 Ω cm to 0.1 Ω cm resistivity, the oxide thickness of 3 µm and a handle layer thickness of 450 µm. The wafer was initially cleaned with piranha at 120 °C for 20 min followed by multiple rounds of rinsing with de-ionized (DI) water. Soon after, the wafer was dipped in buffered oxide etchant (BOE) solution for 2 min to remove the thin surface oxide layer which might have formed by piranha, which is a strong oxidizer. Cleaning with BOE enhance good ohmic contact of Cr/Au on Si. Further, wafer was again rinsed with DI water and baked on a hot plate at 120 °C for 30 min to dehydrate it. Then the wafer was treated with hexamethyldisilizane (HMDS) primer to improve adhesion of photoresist and wafer.

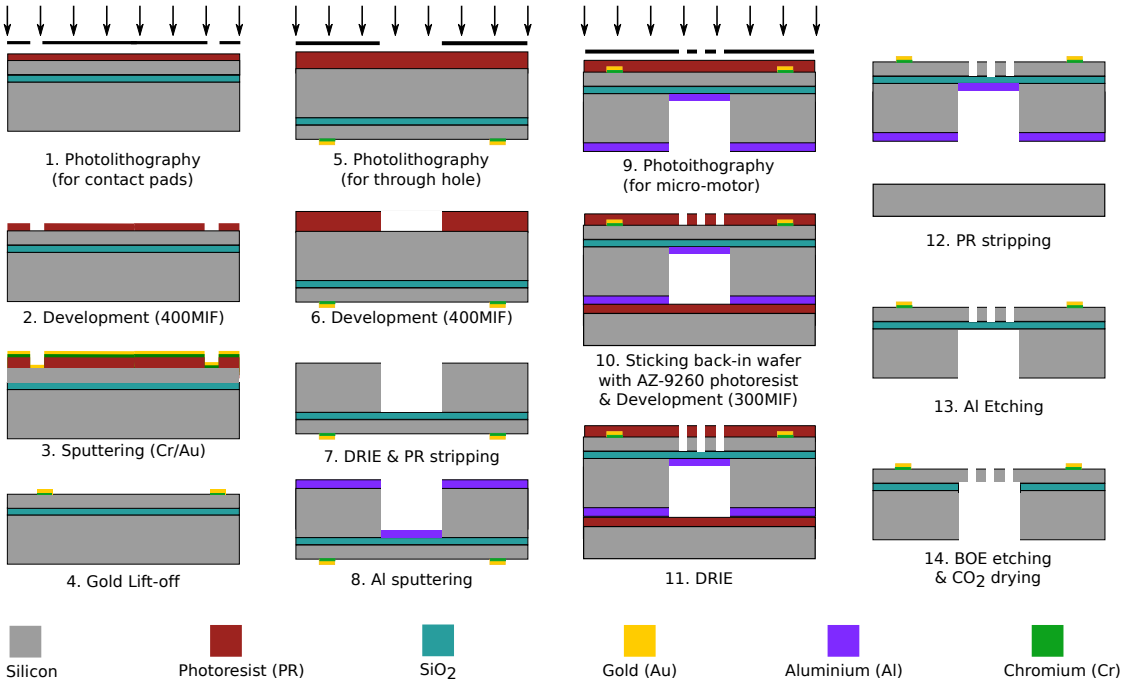

Figure 5.6: Microfabrication steps in realizing micro-stepper motor.

Fabrication involves 4-mask process . The first mask for fabricating contact pads employed similar steps described in PTG fabrication. The wafer was spin coated with AZ-9260 (MicroChem) positive photoresists at 5000 rpm for 30 s obtaining a uniform layer of 4.2 µm. The wafer was pre-baked on an iron hotplate at 110 °C for 4 min to improve adhesion and to remove the solvent content of the resist. Subsequently, photolithography was performed with Karl Suss MA-6 mask aligner under a UV light of 365 nm wavelength having a lamp power of 8 mW cm^{-2} with hard contact mode for 20 s. The exposed regions were removed by 400 MIF developer (MicroChem). The wafer was sputtered with Cr/Au of thickness 20/400 nm followed by lift-off (steps 1-4 in figure 5.6). These contact pads provide electrical connections for driving the micromotor.

The second mask was designed for handle layer etching of the wafer. Pre-preparation steps, which involve piranha cleaning, baking, and HMDS primer treat-

ment were carried out on the wafer. Thereafter, the wafer was spin coated with AZ-9260 photoresists with 2000 rpm to obtain a uniform thickness of 11 µm. The wafer was soft baked for 6 min at 110 °C and slowly ramped down to room temperature. The formation of cracks has been observed while performing photolithography with thick resists (more than 7 µm thickness). The slow ramping down of temperature after soft bake prevents cracking of the photoresist. UV-lithography was performed subsequently for 40 s and the exposed regions were developed away by the 400 MIF developer. The wafer was post baked for 4 min at 110 °C before performing deep reactive ion etching (DRIE), Bosch process, which produces a nearly vertical profile. Etching was continued till the oxide layer, that acts as an etch stop layer. The remaining photoresists were stripped by immersing the wafer in acetone (steps 5-7 in figure 5.6).

Further, an intermediate thick Aluminium (Al) layer of 2 µm was sputtered on the etched handle layer of the wafer before proceeding to device layer patterning (step 8 in figure 5.6). It has been observed that this intermediate sputtering of Al was crucial before performing the photolithography for the micromotor. This coating provides uniform heat conduction in the wafer while baking the photoresists, without which the air in the hole (that was created by DRIE process) prevents uniform transfer of heat. This non-uniformity in heat transfer affects the photolithography process, which is depicted in figure 5.7a-b. The Al coating avoids non-uniformity in baking to a large extent and thus significantly improves the photolithographic resolution, as depicted in figure 5.7c-d.

The photolithography was performed with the third mask involving the device layer pattern of the microactuator. The wafer was spin-coated with a low

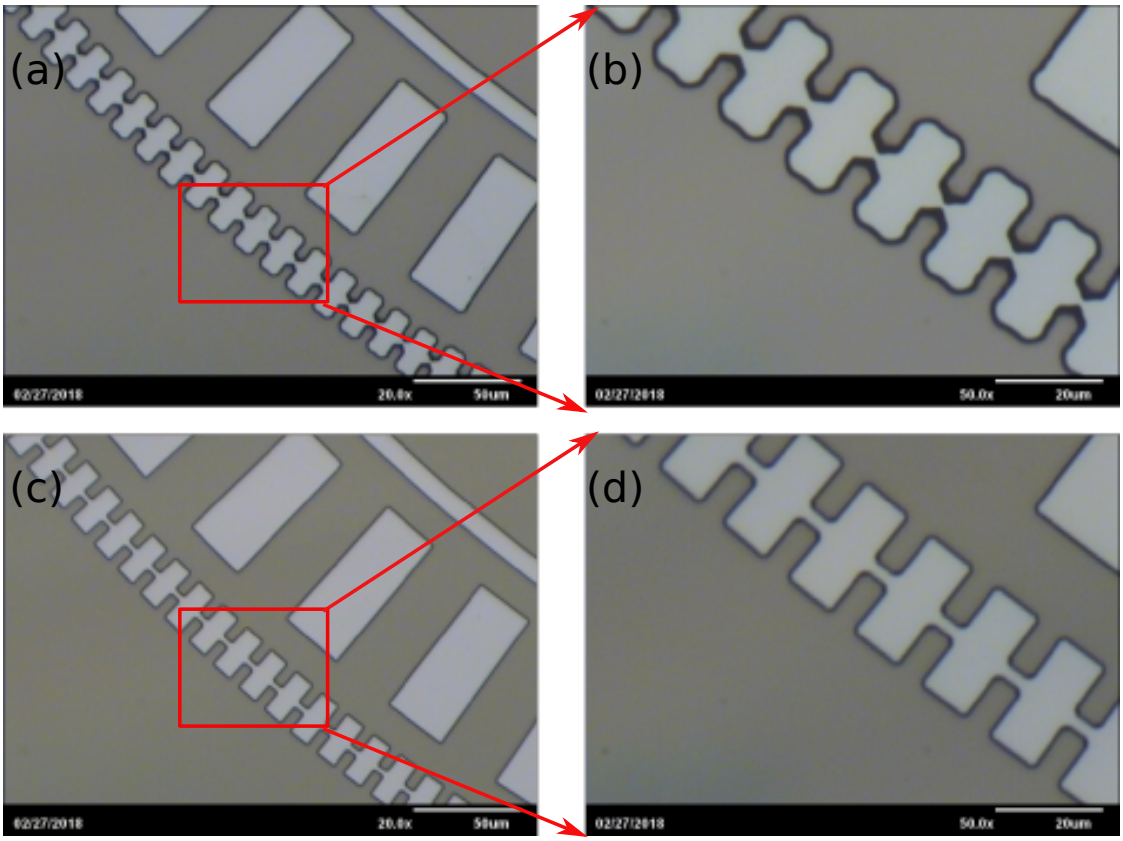

Figure 5.7: (a)-(b) Poor photolithographic resolution at the edges of the poles arises due to the non-uniformity in photoresist baking. (c)-(d) Improvement on lithography, obtaining 90° at the corners of electrode poles after Al coating on the backside.

viscosity resist, AZ-7217 (MicroChem), preceded by piranha cleaning and HMDS treatment. Soft baking of 90 s was performed at 110 °C and allowed to cool to room temperature. Subsequently, UV-lithography was performed in vacuum mode for 3.4 s, after which post baking was performed for 60 s at 110 °C. Before developing, another silicon wafer was spin coated with AZ-9260 photoresist and manually bonded with the SOI wafer. This is an important process because the developer contains hydroxide ions, which react with Al. Bonding with the protecting wafer, avoids contact of the developer with the Al coating. The wafer was immersed in

the 300 MIF developer (MicroChem) solution with a gentle agitation for 2 min, to remove the exposed regions (steps 9-10 in figure 5.6).

The resist was hard-baked for a further 2 min at 110 °C and DRIE was performed for 22 min 19 s till it reaches the etch-stop oxide layer. Further, the aluminum was removed by the aluminum etchant. Finally, the sacrificial oxide layer was removed by buffered oxide etchant and dried in a supercritical CO_2 dryer (Automegasamdri Model: 915B) (steps 11-14 in figure 5.6). The SEM images of the fabricated actuator are shown in figure 5.8

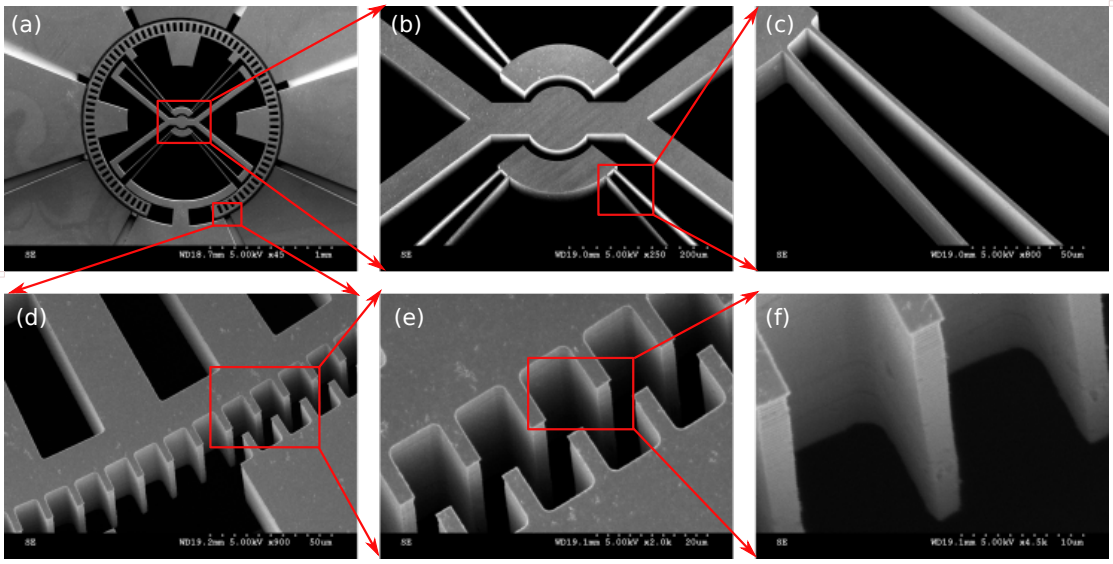

Figure 5.8: SEM image of the (a) rotary actuator, (b) flexural pivot bearing, (c) flexure springs, (d) high aspect ratio electrostatic poles; (e) close-up view of the poles that are misaligned by $(1/3)^{rd}$ of the pitch; and (f) scalloping effects occurred by the Bosch process in the etched profile.

5.3.4 Static measurements of rotary actuator

5.3.4.1 Half-stepping motion measurements

The micro stepper motor was tested by applying half-stepping voltage waveform. The half-stepping voltage sequence was generated by a Raspberry-Pi module. The Python code for the generation of such voltage waveform is described in appendix C.3. Initially, the half-stepping time interval was set to 1 s in the experiment. It can be adjusted based on the camera frame rate and the applications. The generated timing sequence was fed to a low noise voltage amplifier (Piezo Drive - PDu150). The voltage amplifier amplifies the voltage generated from pins 11, 12, and 13 of the Raspberry-Pi module from an amplitude of 3.3 V to 33 V. The half-stepping voltage sequence generated is depicted in figure 5.9a-b. The amplified output signal was fed to the device through contact pads. Successful stepping motion was obtained by the micro-stepper motor with the applied voltage sequence. It has been verified that the stepper motor rotates in reverse direction by swapping the phase-1 and phase-3 voltage waveforms. Each half-step produced an angular step equivalent to one-half of the pole-width.

The images of stepping motion of the micromotor were captured with a CCD camera for all the half-steps. The equivalent sub-pixel shift in the rotor poles was measured by image analysis. The angular information calculated from image analysis is plotted in figure 5.9c-d. Each step in the rotation produced approximately 0.2° which matches with the theoretical predictions. It was observed that the measurements were consistent with each steps showing good repeatability in the angular step control. By applying a higher voltage, a larger rotational range can be obtained.

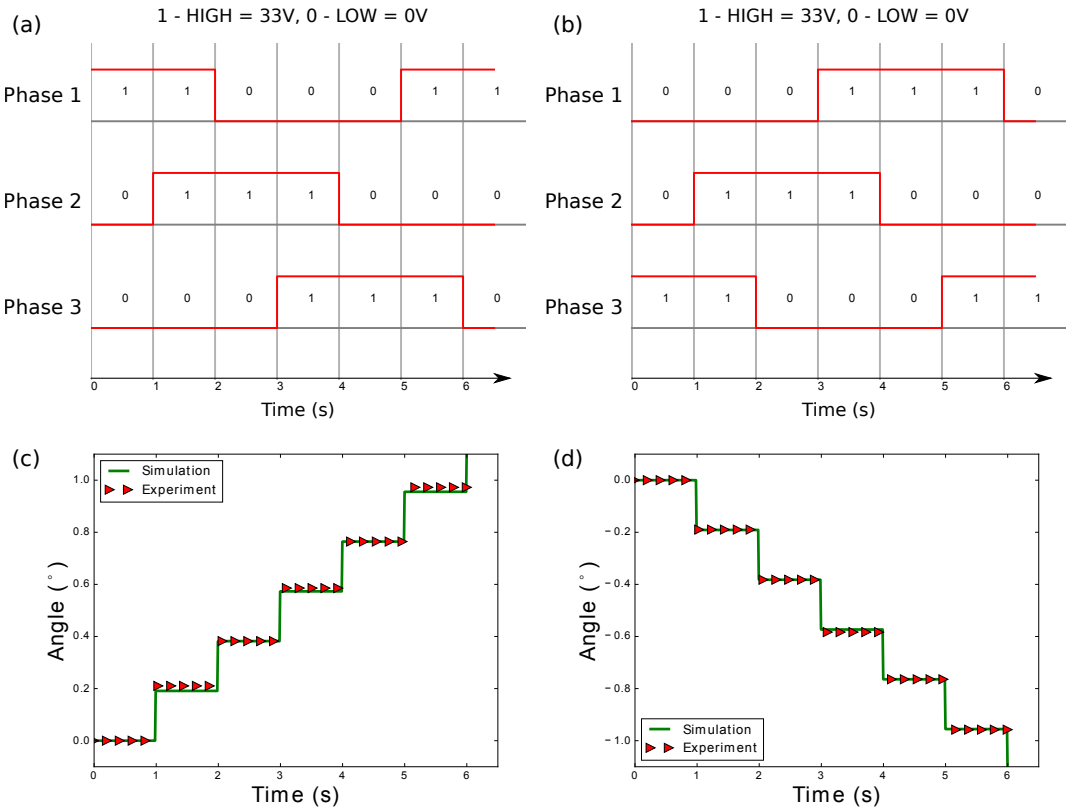

Figure 5.9: Illustration of stepper motor driving principle: driving half-stepping voltage waveform for (a) counter clockwise rotational motion; (b) clockwise rotational motion. Experimental plots showing rotation of 0.2° per step in (c) counter clockwise rotation; (d) clockwise rotation mode.

5.3.4.2 Measurement by time delay variation

The rotary actuator was also tested by varying the time delay of the 3-phase half-stepping voltage waveform. The stepping signal resulted in a realignment of the movable poles achieves the desired rotation. The plot showing angular displacement as a function of time is depicted in figure 5.10. The actuator was tested for a two-step delay ($t_s = 1\,s$ and $t_s = 2\,s$). This controlled stepping motion allows a precise orientation of grating and can be used with conventional CCD

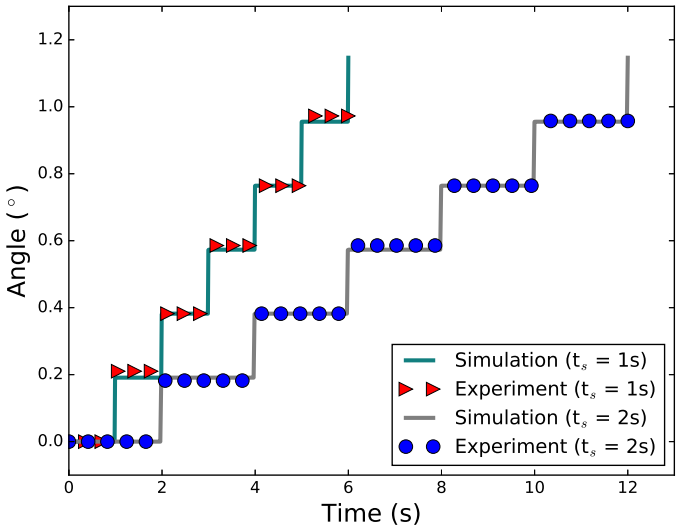

Figure 5.10: Experimental plot showing angular change with respect to time steps (t_s) in half-stepping voltage.

camera for imaging.

5.4 SU-8 diffraction grating realization

5.4.1 Microfabrication techniques

The process is divided into two steps: the first step involves fabrication of the mold. Here, an off-the-shelf diffraction grating was used for mold preparation. In the next step, the generated mold was used for the replication process. The detailed experimental procedure is described below.

5.4.1.1 Mold preparation

The fabrication of the diffraction grating involved preparation of a soft mold using polydimethylsiloxane (PDMS), a soft material, which was used for replication on SU-8 photoresists. PDMS is a widely used material for molding or prototyping

because it is chemically stable after it is cured and possess weak adhesion. For mold preparation, the PDMS base and the curing agent (Sylgard 184 Silicone Elastomer - Dow Corning) were mixed in a 10:1 proportion and dispensed onto an off-the-shelf diffraction grating. The solution was then placed inside a degassing chamber for 30 min to remove the air bubbles generated in the solution during mixing. Further, the solution was cured in an oven at 75 °C for 2 h 30 min. The PDMS layer was peeled off from the off-the-shelf holographic diffraction grating, thus forming the negative of the master grating. This mold was used in later steps for the replication.

5.4.1.2 Replication methodology

The generic scheme of the proposed wafer-level fabrication technique of diffraction grating using SU-8 is described in figure 5.11. Initially, a 100 mm diameter silicon (Si) wafer was cleaned in piranha solution (3:1 mixture of sulfuric acid and hydrogen peroxide) at 120 °C for 20 min followed by rinsing with de-ionized (DI) water. For dehydration, the wafer was placed on hotplate at 110 °C for 30 min. Next, the wafer was spin coated with OmniCoat (MicroChem) at 3000 rpm for 30 s, which acts as a sacrificial layer and will be removed later. The wafer was then baked at 200 °C using a hotplate for 60 s and allowed to cool to room temperature. SU-8 2050 negative photoresist was dispensed on the wafer and spin coated at 3500 rpm for 30 s to obtain a uniform thickness of 40 µm. This was followed by soft-baking, that was performed on a leveled programmable hot plate for precise temperature control. Initially, the temperature was ramped up at the rate of 2 °C min^{-1} from room temperature to 65 °C at which it was maintained for 10 min. Then the temperature

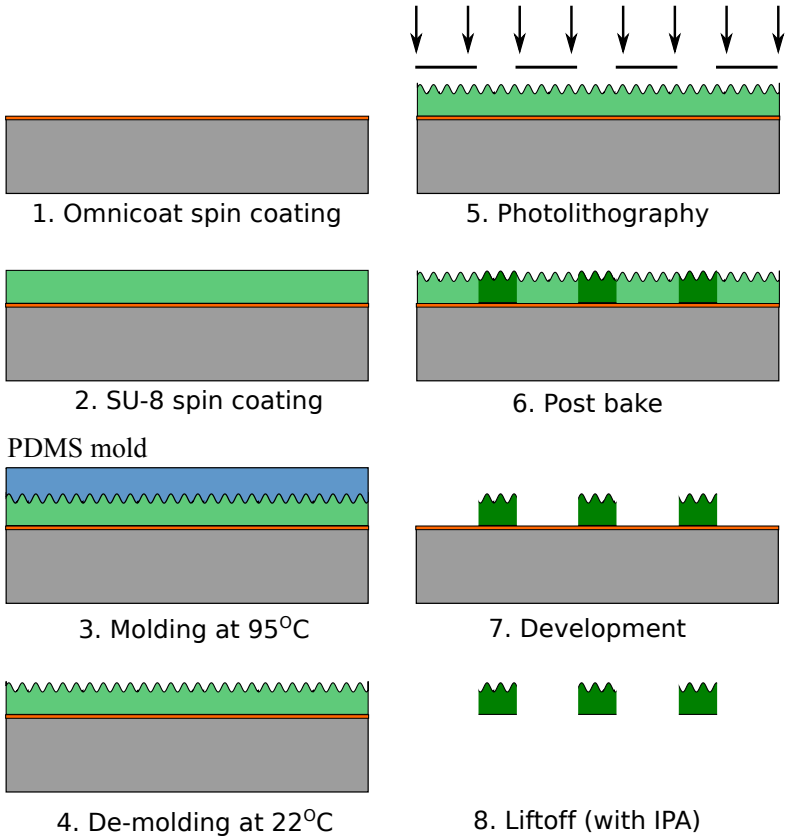

Figure 5.11: Fabrication process flow for replication followed by photolithography.

was again ramped up at $2\,^{\circ}\mathrm{C\,min^{-1}}$ to reach 95 °C and maintained at 95 °C for 20 min allowing the solvent content of the SU-8 to evaporate. The glass transition temperature (T_g) of uncured SU-8 is ∼65 °C [146]. Hence, the resist remains soft at 95 °C. The PDMS master mold was then placed on top of the resist, making sure that no voids were created between the mold and the resist. The temperature slowly ramped down at $4\,^{\circ}\mathrm{C\,min^{-1}}$ to reach the room temperature. The PDMS mold was then peeled off releasing the diffraction grating pattern on top of the resists.

The next step involves photolithography to obtain the desired pattern (footprint of the grating). The wafer was exposed to UV light (365 nm) using contact mask

lithography with a power of $8\,\mathrm{mW\,cm^{-2}}$ for 21 s, making the exposed region hard due to cross-linking of the polymer. Photolithography was performed in hard mode assuring a good contact between the mask and the wafer. After UV exposure, post baking was performed on a programmable hotplate by ramping up the temperature at $2\,^{\circ}\mathrm{C\,min^{-1}}$ from room temperature to 65 °C and maintained at 65 °C for 5 min. The temperature was again ramped up at a rate of $2\,^{\circ}\mathrm{C\,min^{-1}}$ to reach 95 °C, then maintained at 95 °C for 10 min. Further, it was brought back to the room temperature at a rate of $4\,^{\circ}\mathrm{C\,min^{-1}}$. The schematic temperature profile for the soft baking and the post baking SU-8 is depicted in figure 5.12. The wafer was

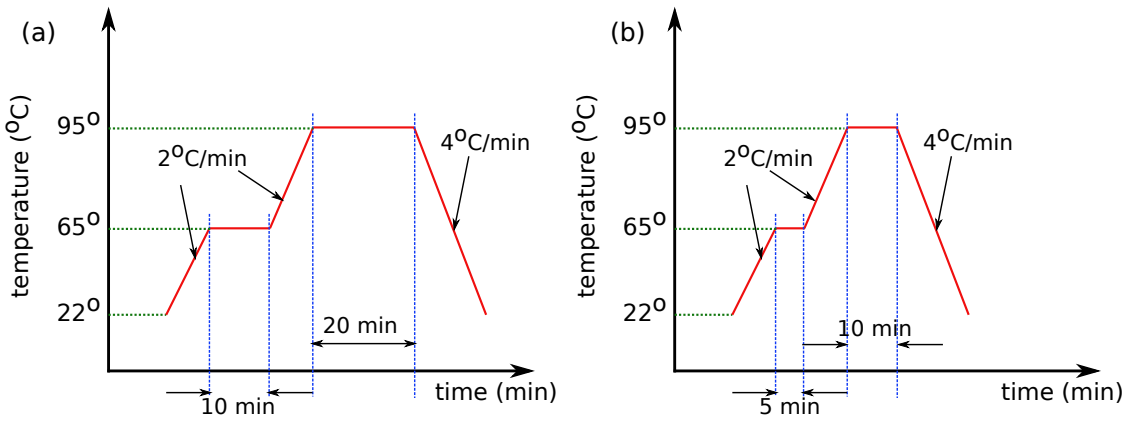

Figure 5.12: Schematic of baking temperature profile of SU-8 for (a) soft baking and (b) post baking.

immersed in the SU-8 developer solution for 10 min with gentle agitation, where the unexposed part of SU-8 was removed. Finally, the wafer was cleaned with isopropanol (IPA) solution and dried with a nitrogen gun.

Figure 5.13 shows the array of diffraction grating fabricated, both on silicon and fused silica wafer. The baking steps and the UV exposure time of SU-8 on glass substrate are 1.5 times longer than in the case of the silicon wafer.

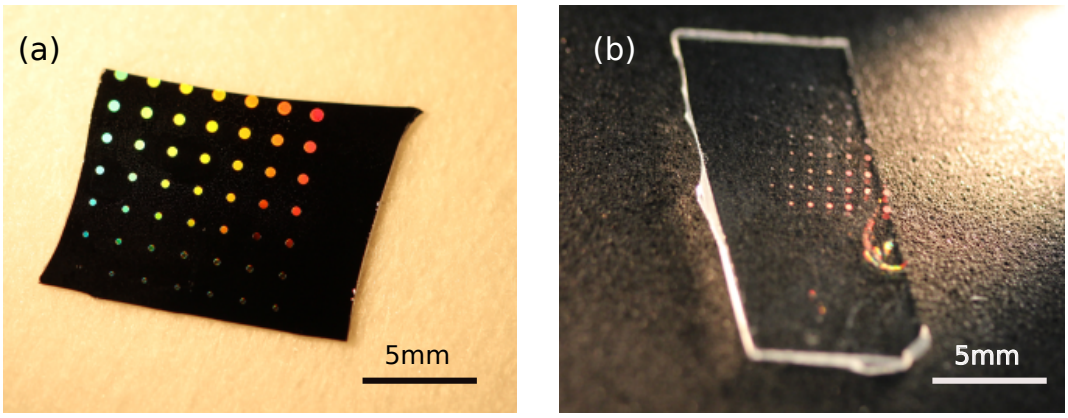

Figure 5.13: Micro-patterned diffraction grating fabricated on (a) silicon wafer (b) glass wafer.

5.4.2 Optical characterization

The two parameters that determine the optical quality of a material are transmittance and refractive index. To study optical transmittance, the SU-8 resist was spin-coated on a fused silica, was illuminated by broadband light source coupled with an optical fiber. The output light was collected by a fiber optic coupled spectrometer (Avantez Ava Spec EDU UV/VIS). The optical transmittance was investigated by measuring the light received by the spectrometer. The transmittance measurements were conducted at different stages in the course of fabrication. Figure 5.14a shows the comparison of transmittance spectra of the fused silica wafer, uncured SU-8 and fully cured SU-8 coated wafer. The plot indicates that SU-8 has relatively low optical absorption in the visible range. The deviation of transparencies between cured and uncured SU-8 is calculated to be 1.1 %. The mean percentage difference between crosslinked SU-8 and fused silica in the visible range is found out to be 2.44 % proving good transmittance.

To investigate the dielectric property of the material, SU-8 2002 was spin coated on a silicon wafer obtaining a uniform thin layer (1.3 µm). The complex reflectance

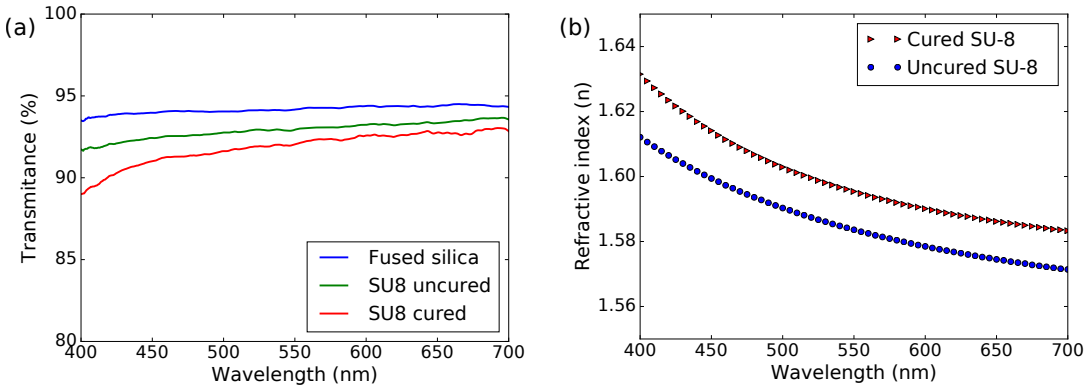

Figure 5.14: (a) Comparison of optical transparencies of fused-silica and SU-8 on fused-silica in the visible spectral range, (b) refractive index plot for the cured and uncured SU-8 polymer in the visible wavelength range measured by a spectroscopic ellipsometer.

ratio was derived using spectroscopic ellipsometer (VASE, J.A. Woollam Co.) for the visible range of wavelengths. The refractive index was measured from the complex reflectance ratio. The data obtained was fitted against Cauchy's empirical relation given by Eq. (5.4), with Cauchy's coefficients A = 1.5516, B = 0.0092, C = 0.0001 for cured SU-8, and A = 1.5681, B = 0.0062, C = 0.0006 for uncured SU-8.

$$n(\lambda) = A + (B/\lambda^2) + (C/\lambda^4) \tag{5.4}$$

The plot showing the refractive index variation for 400 nm to 700 nm for un-cross-linked and fully cross-linked SU-8 polymer is depicted in figure 5.14b. The refractive index of fully cross-linked SU-8 is slightly higher than that of the un-cross-linked SU-8. The difference in the index is expected as it is evident from the transmittance measurement that cross-linked SU-8 has slightly lower transmission than the un-cross-linked polymer.

5.4.2.1 SEM and AFM measurements

The fabricated device was characterized both by scanning electron microscope (SEM) and by atomic force microscope (AFM). The SEM images of the fabricated diffraction gratings on top of the patterned SU-8 is depicted in figure 5.15. This technique allows a reliable, wafer-level integration of complex micro/nano structures within MOEMS using tools and processes, that are compatible with standard micro-fabrication.

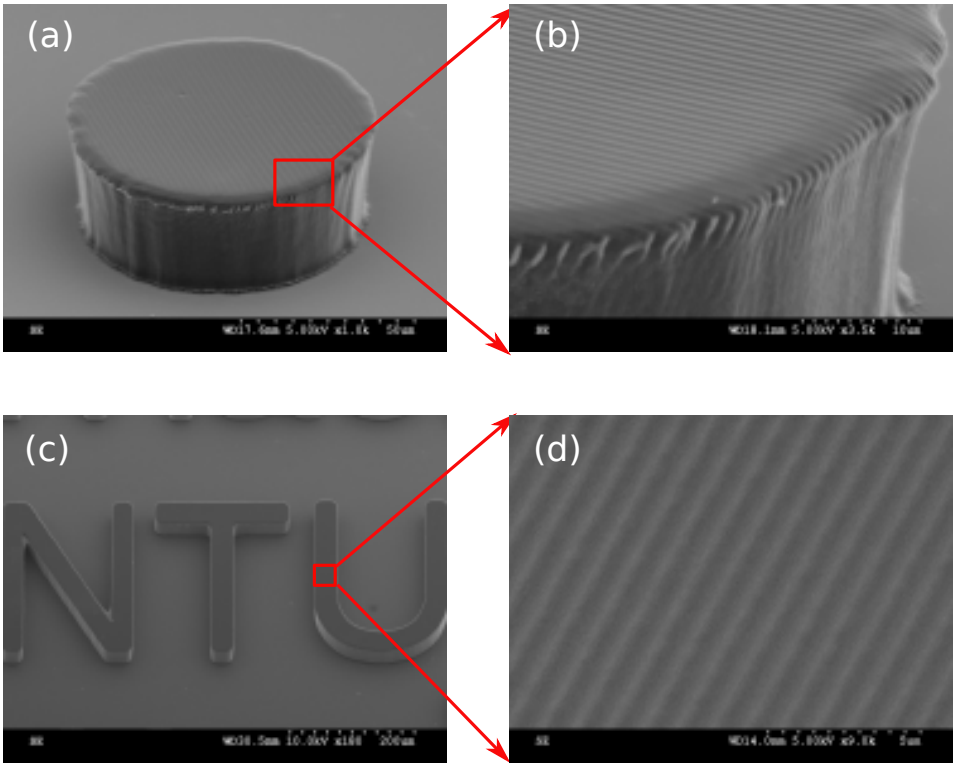

Figure 5.15: SEM images of the replicated diffraction grating imprinted on (a)-(b) disc of diameter 50 µm, (c)-(d) on block with name "NTU" patterned on SU-8 using photolithography.

To test the quality of the replication, the period and the height of the diffraction grating need to be investigated. The period of the grating determines the diffraction angle of the incident light and the shape of the period determines the

efficiency of the diffraction grating. To characterize the shape and the period of the grating, AFM was used to obtain the surface profile. The scanning of the sample with AFM was performed by so-called *tapping mode*. Although the tip of the AFM is in the range of few nm, it would be difficult to obtain the exact-replica of the sample if it posses steep features. However, it is a good choice of measurement for comparison purposes. Figure 5.16 shows the AFM measurements, and the line profile measured from both the original master and the replicated SU-8 grating. It was found that the period of the diffraction grating almost remains the same.

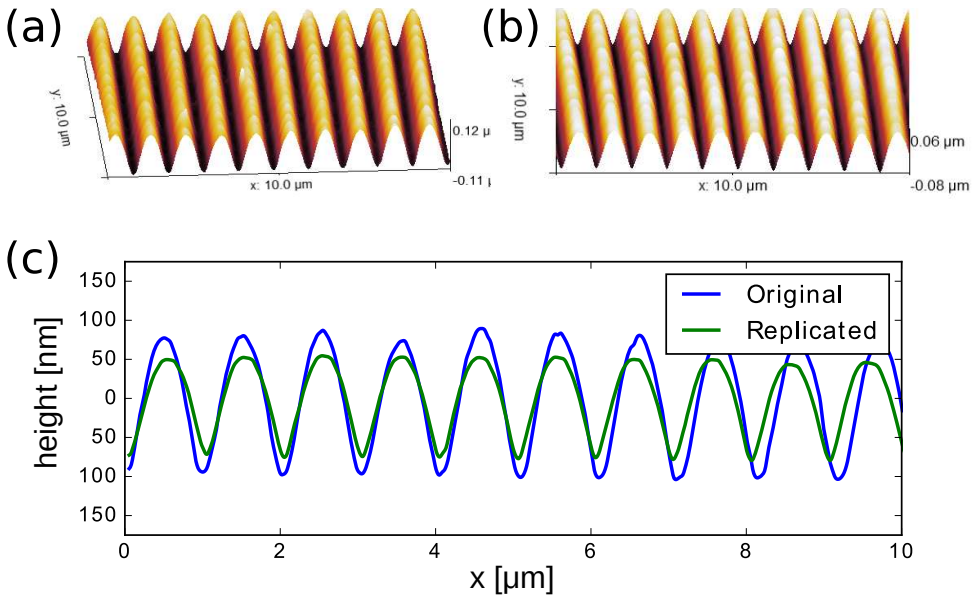

Figure 5.16: Surface profile measured by AFM on (a) master grating, (b) SU-8 replicated grating, (c) line profile showing the comparison of original with replicated grating.

However, the amplitude of the replicated diffraction grating was slightly smaller than the original structure. This difference could be probably due to the polymer shrinkage/expansion during the thermal processing. To obtain the desired replicated structure, this tolerance needs to be considered for replication, and needs

to be incorporated into the mold design. This replication technique was also performed for fabricating blazed angle diffraction gratings. Figure 5.17 depicts the surface profile obtained by AFM for a blazed angle grating having 600 lines/mm. A similar trend of reduced amplitude was found in the blazed angle SU-8 replicated grating.

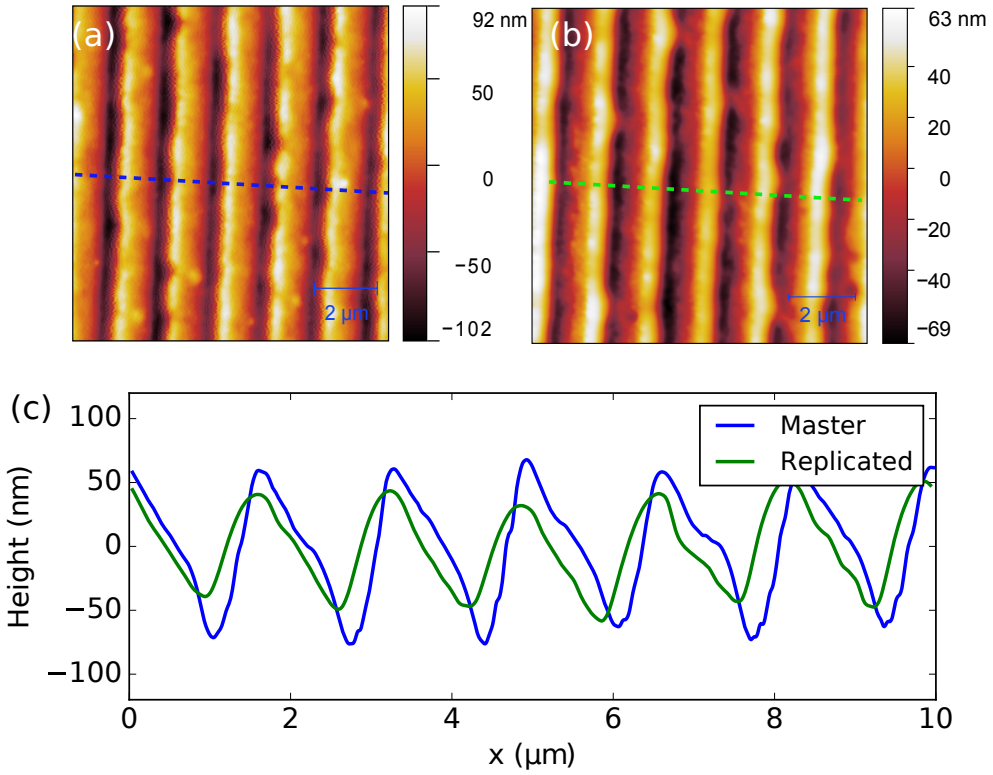

Figure 5.17: Surface profile of blazed angle diffraction grating (600 lines/mm) on (a) PDMS mold, (b) SU-8, and (c) line profile comparing the quality of replication.

The SU-8 replicated blazed angle diffraction grating was optically tested by shining a laser light of 532 nm wavelength onto the grating, and the diffraction pattern obtained was projected onto a dark screen that is depicted in figure 5.18. It was found that intensity of first-order diffraction pattern (m = 1) was higher than the negative order (m = -1). This higher intensity distribution of light is due

to the blazed angle profile.

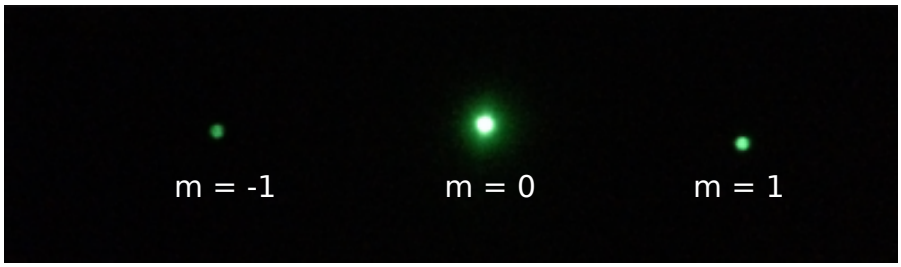

Figure 5.18: Diffraction pattern obtained by the grating is illuminated with a LASER source of 532 nm wavelength.

5.4.2.2 Diffraction efficiency measurements

The diffraction efficiency of replicated holographic (sinusoidal) grating was calculated both theoretically and experimentally. The efficiency (η) of sinusoidal grating can be calculated from [122] as:

$$\eta = T J_m^2 \left(\frac{q}{2}\right), \tag{5.5}$$

where, J_m is the Bessel function of the first kind, m is the diffraction order, T is the percentage of transmittance for the incident wavelength , q is the phase constant defined by $2\pi(n_{su8} - 1)h/\lambda$, where, h is amplitude of grating groves, λ is the incident wavelength, n_{su8} is refractive index of SU-8 (figure 5.14b).

The efficiency of the diffraction grating was computed experimentally by shining coherent light sources of multiple wavelengths. The power of the diffracted light was measured by a power meter. The 0^{th} order and the 1^{st} order diffraction efficiencies were measured for three sets of wavelength and are listed in table 5.2. It was found that values of measured efficiencies matched with the theoretical predictions. The efficiency of the 1^{st} order diffraction grating can be further improved by

fabricating the master mold, and by taking into account of the polymer shrinkage and the replication tolerances, as the efficiency mostly depends on the height of the diffraction groves.

Table 5.2: Diffraction efficiency measurements. (h=0.15 µm)

Wavelength	**Measured (Calculated, Eq. (5.5))** η (%)	
(nm)	$m = \mathbf{0}$	$m = \mathbf{1}$
488	78.1 (73.7)	5.1 (6.7)
532	79.4 (77.6)	3.7 (5.6)
637	83.3 (82.2)	2.7 (3.9)

5.4.2.3 Dispersion effects of replicated grating

The dispersion of the grating was also investigated optically. To study the dispersion properties, an optical slit was illuminated with a broadband light source (halogen lamp). The illuminated slit was re-projected on to a detector using a standard 4-F imaging configuration. The experimental demonstration for dispersion measurement is depicted in figure 5.19. The focal lengths of the imaging lenses were 50 mm, thus obtaining a magnification of unity. A camera was placed on the imaging plane to get the image of the slit. The fabricated grating was placed on the Fourier plane (2-F plane) of the 4-F imaging system. The grating produced an angular dependent wavelength shift of the optical slit at the detector plane. The camera was re-adjusted to capture the 1^{st} order wavelength information in the visible range. The dispersed image of the optical slit was captured by a camera, which is shown in figure 5.20. The change in the dispersion orientation was also

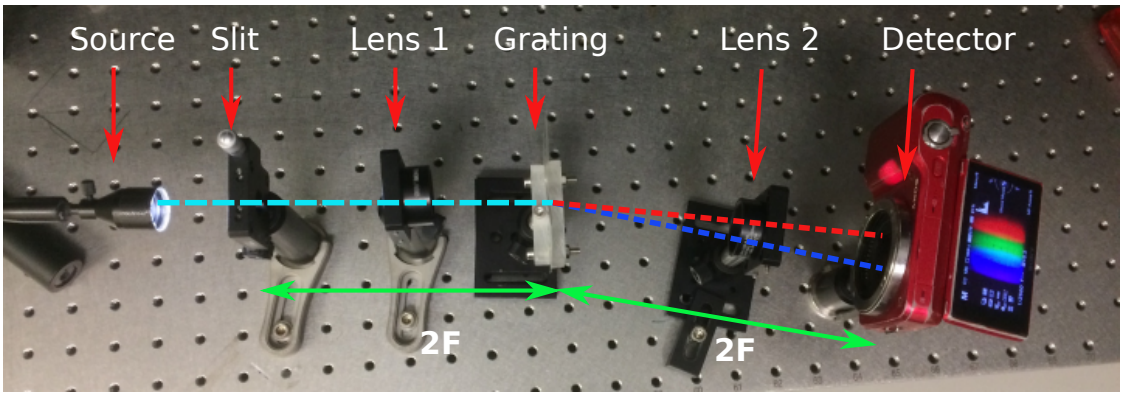

Figure 5.19: Experimental realization of 4-F imaging optical system to study the dispersion effects of replicated grating.

investigated by rotating the diffraction grating in the same optical configuration. The grating was rotated in both clockwise and anti-clockwise directions. The corresponding change in the dispersion direction at the detector plane was captured by the camera. The change in the dispersion direction corresponding to 13°, 0°, −13° are depicted in figure 5.20a-5.20c. This changes in the dispersion direction can be utilized for optical transfer function diversity in quasi-snapshot imaging spectrometer.

Replicated gratings with different grating parameters were characterized to study the dispersion spread. Dispersion spread depends on the grating period. A smaller grating period has a large diffraction angle, which causes wide dispersion spread. Figure 5.21 shows the comparison of dispersion spread when two different periods of grating are tested. It was verified that dispersion due to the 600 lines/mm grating shows a smaller dispersion spread, and was almost doubled when the grating parameter was increased to 1200 lines/mm.

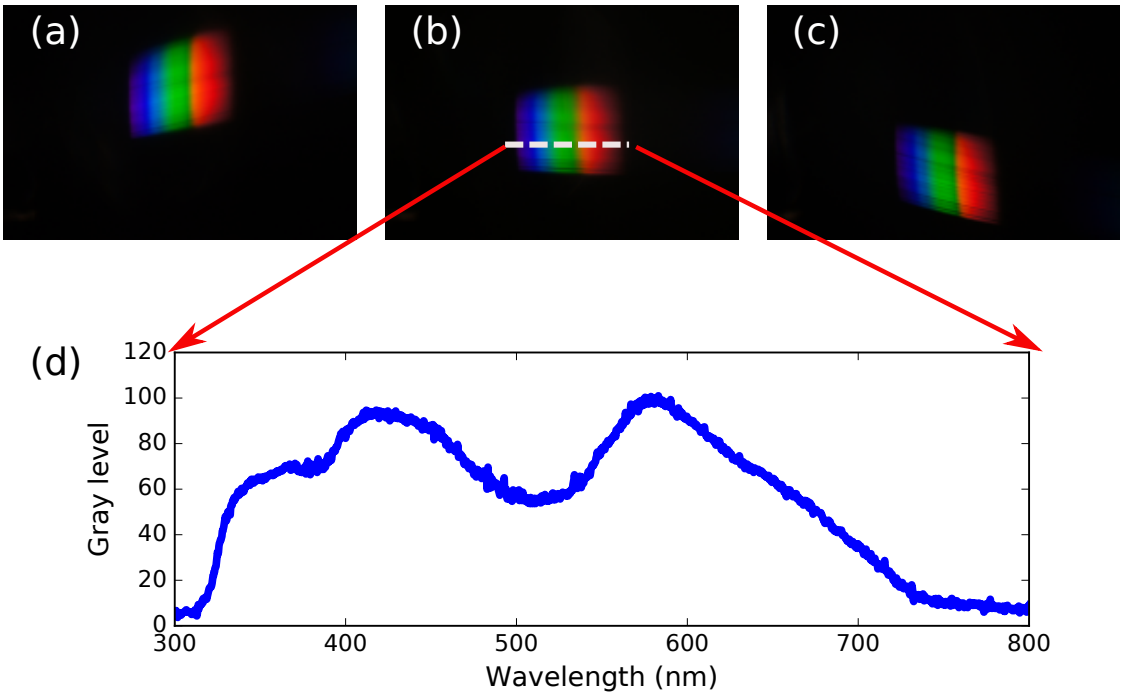

Figure 5.20: Dispersion measured by rotating diffraction grating by (a) 13°, (b) 0°, (c) −13°; (d) spectral profile of the dispersed light of a halogen lamp used as the illumination source for 0° case.

5.5 Towards the integration of diffraction grating on to the microactuator

The fabrication procedure for an array of diffraction gratings by means of replication followed by photolithography was described in section 5.4.1. The fabricated disc-shaped structures were removed for integration by immersing the wafer into diluted isopropanol at room temperate for 24 h. Isopropanol dissolves the omnicoat sacrificial layer, resulting in lift-off of the disc-shaped SU-8 diffraction grating. The devices were filtered out and dried in an ambient environment. The diffraction grating is to be bonded on to the microactuator using UV curable polymer glue via a pick and place mechanism.

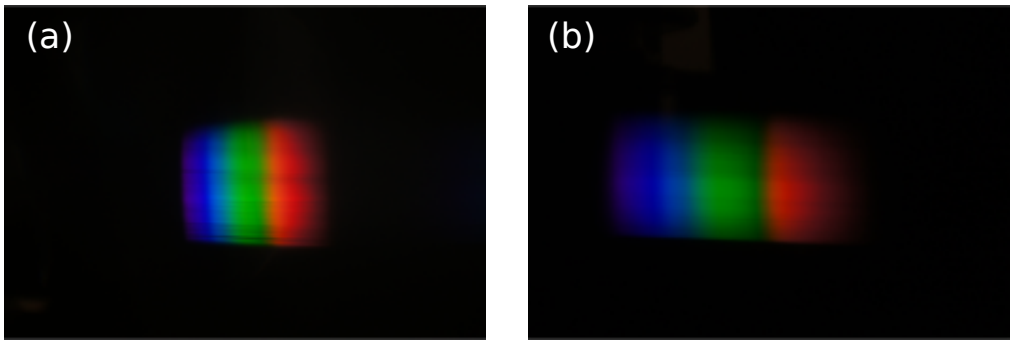

Figure 5.21: (a) Dispersion due to 600 lines/mm grating showing smaller dispersion spread, and (b) larger dispersion spread when the grating parameter is increased to 1200 lines/mm.

5.5.1 Micropipette fabrication

Optical glue, Norland Optical Adhesive - 65 (NOA-65), was used for bonding the diffraction grating onto the microactuator. For precise dispensing of the optical adhesive on to the actuator, a glass micropipette was used, which can dispense limited volume of glue. For the experiment, size of the pads for dropping the glue is approximately 100 µm × 100 µm. Hence, the micropipette diameter has to be as small as possible to avoid the formation of big droplet. A micropipette of the desired diameter was fabricated by a micropipette puller on the glass pipette, having an outer diameter of 1 mm and an inner diameter of 0.5 mm. The diameter was carefully controlled by the pipette puller (Flaming/Brown Micropipette Puller P-97) to obtain a micropipette that has a dispensing diameter of 10 µm. The dispensing length of such custom made micropipettes are generally long and not suitable for the experiments. The long protruding length was shortened by a microforge (MF-900 Narishige). The experimental set-up for making a micropipette with a short and blunt tip is shown in figure 5.22a. A glass bead attached to the microforge is heated to a high temperature to shorten the long tip. The tip

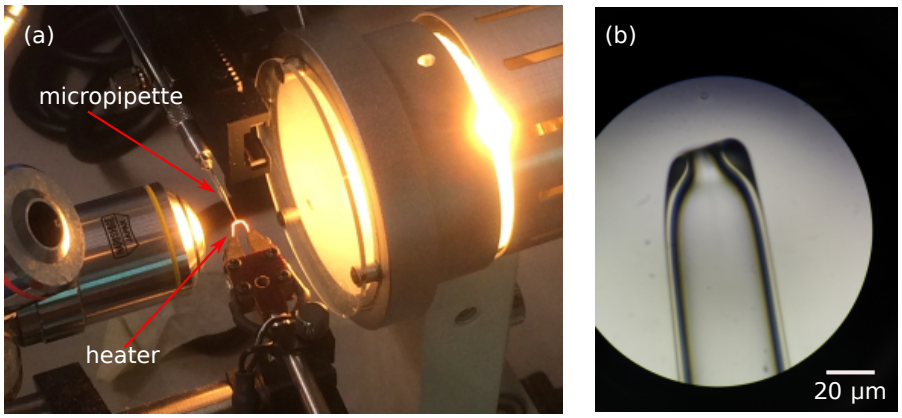

Figure 5.22: (a) Experimental set-up for making blunt-micropipette with micro forge (b) the fabricated micropipette observed under transmissive microscope.

was also made blunt (figure 5.22b) by carefully controlled movement of the pipette towards the glass beed.

5.5.2 Dispensing methodology

The micropipette was filled with the optical adhesive using a syringe and attached to a 27 G needle. Prior filling of the glue inside the micropipette was crucial for precise dispensing of liquid. Also special care was taken to avoid bubble formation inside the solution, as it affects the volume of the drop. Figure 5.23 shows NOA-65 that was filled inside the micropipette.

5.5.3 Droplet generation

The micropipette was then connected to a pneumatic dispensing system. A small volume syringe of 15 µL (NanoFil^{TM}, Prime Bioscience) was used to push the liquid by means of a computer controlled motor that enables precise step movement of the syringe, thereby controlling the volume to be dispensed. Both, the dispensing unit

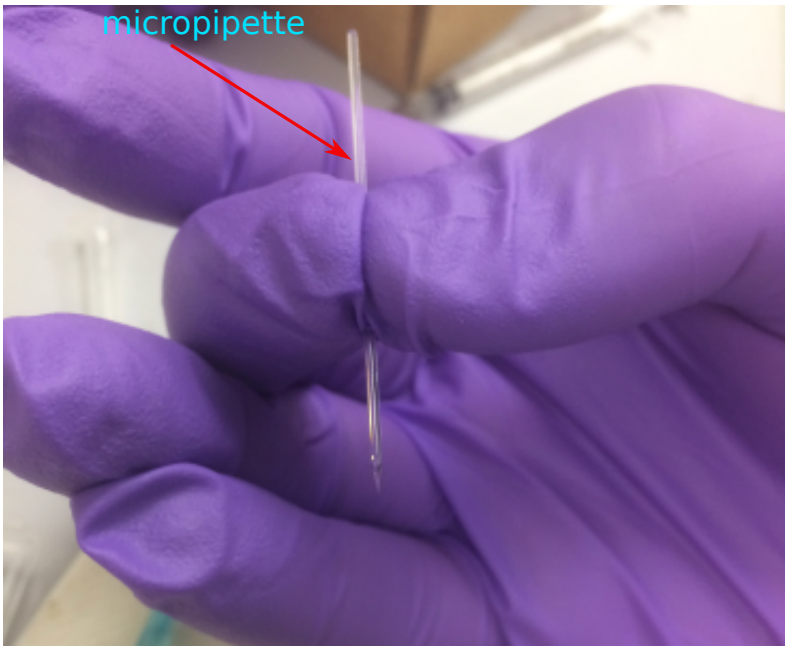

Figure 5.23: Optical curable adhesive (NOA-65) filled in the micropipette.

and the sample stage, were attached on top of a precise x-y-z piezo stage controller. Two sets of microscope (on top and bottom) were connected in the arrangement for aligning samples with the pipette. It enables dropping the glue at the exact location of the actuator. The experimental set-up of the dispensing system is shown in figure 5.24. While dispensing the liquid through the micropipette, it was observed that the drop wobbles around the pipette rather than being pulled by gravity. It could be due to the surface tension of the liquid, which holds the drop around the pipette. To circumvent this, before filling the optical adhesive, the micropipette was treated with atmospheric plasma and followed by silanization for 3 h.

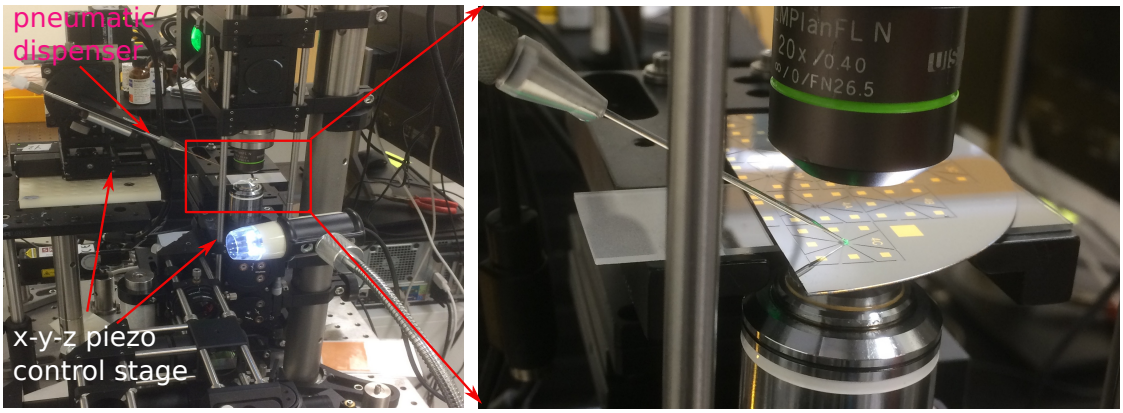

Figure 5.24: Experimental set-up for dispensing pico-liter droplets of NOA-65 for integrating the diffraction grating on the rotary actuator.

5.5.4 Diffraction grating integration

Silanization helped in generating the desired shape of the drop to dispense on the pads. In the initial attempt, it was found that glue spreads out of the holding pads and gets filled between the electrode poles, resulted in damage to the micromotor. To avoid this, stepper motor was again fabricated as described in section 5.3.3 with a gold ring electrode on the dropping pad. The refabricated motor is shown in figure 5.25. The gold ring was able to block the optical glue, thereby preventing

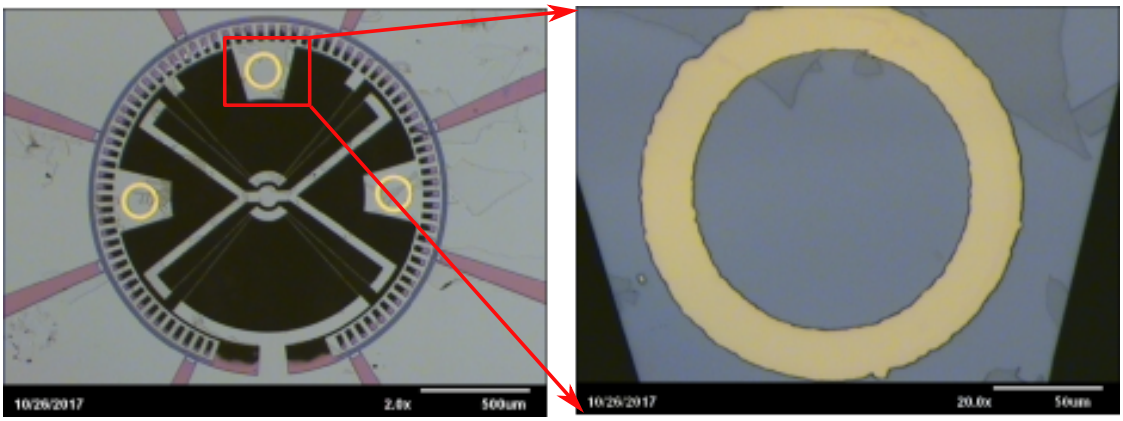

Figure 5.25: Micro steppermotor re-fabricated by with a gold ring on the glue deposition pads.

spreading due to hydrophobic behavior. Figure 5.26 shows the surface behavior of gold preventing NOA-65 from spreading. The gold ring, not only limits the

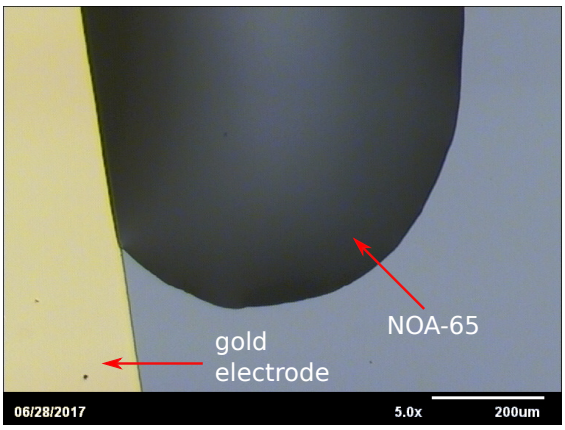

Figure 5.26: Gold electrode stopping the overflow of NOA-65 on silicon surface.

spreading of the glue, but also helps in acting as a spacer between the optical element and the microactuator. Extra care was taken by silanizing the wafer to make the surface hydrophobic in nature. This process also helped in acting the optical glue to form a spherical shape avoiding spreading.

The surface behavior of the wafer before and after silanization was studied by dropping 7 µL of DI water on a side of the wafer without destroying the microactuators. The surface interaction of the DI water before and after the silanization is compared in figure 5.27. The contact angle was measured from the images captured that is analyzed using Fiji-ImageJ with 'contact angle' plugin. The contact angle measured before and after silanization was found to be 39.8° and 112.4° respectively, clearly showing hydrophobic nature.

Finally, the micropipette was brought into focus by the bottom microscope in the experimental set-up. In the subsequent step, the bottom illumination was turned off and the sample was carefully placed beneath the micropipette. Fine

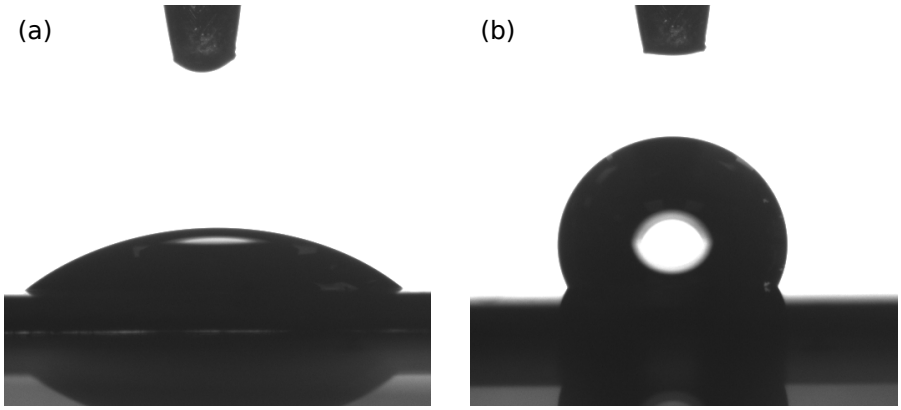

Figure 5.27: The measurement scheme in determining the contact angle of DI water on the silicon surface (a) before silanization, and (b) after silanization.

movement of the sample was precisely controlled by the x-y-z piezo stage with a computer. A small drop of optical glue was dispensed inside the gold ring (figure 5.28a). The SU-8 diffraction grating was then bonded on top by pick and place mechanism. The diffraction grating was precisely placed using a vacuum pick-up tool (HAKKO, H394-01) with a nozzle having a diameter of 0.4 mm (HAKKO-H392NA1164). The diffraction grating integrated on the microactuator is depicted in figure 5.28b. Later, the optical adhesive between the grating and the actuator

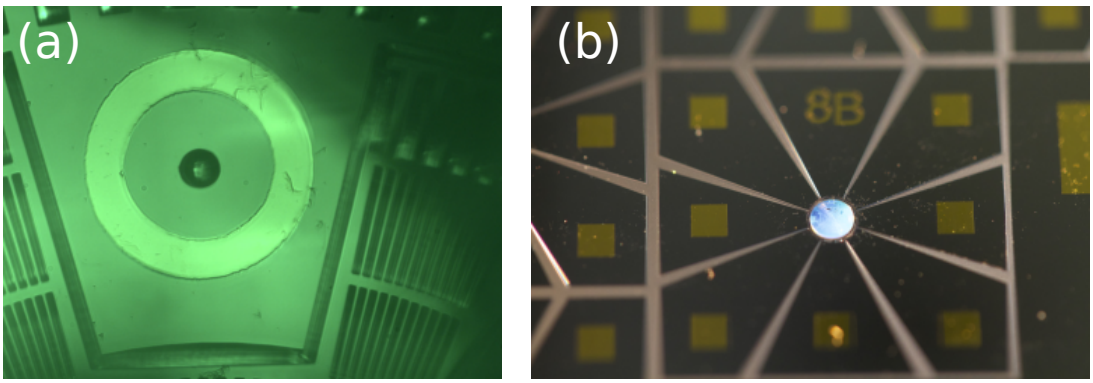

Figure 5.28: (a) Drop of NOA-65 dispensed on the center of gold ring, (b) diffraction grating bonded on the micro-stepper motor.

was cured using a UV lamp of $8\,\mathrm{mW\,cm^{-2}}$ for 15 min. The curing time was slightly longer than the theoretical value of 10 min 30 s. This is because the SU-8 layer covering the glue, which limits the incoming power of light.

5.6 Summary and discussions

An electrostatic rotary MEMS stepper motor was demonstrated using SOI technology. Precise stepping motion of 0.2 °/step was achieved with the half-stepping voltage. Six distinct steps of the micromotor were experimented with an actuation voltage of 33 V. However, with the application of higher voltage, a larger angular tuning can be obtained. The device was also tested by varying the delay of the voltage sequence and a highly repeatable stepping sequence was observed. Stepper motor based actuation serves better advantages over comb drive designs, since displacement relation of the comb drive based device is vulnerable to fabrication tolerance, where as displacement from stepper motor depends mostly on the width of the electrode poles.

In the later part of the report, an array of variable size diffraction gratings was fabricated by combining replication and photolithography patterning on SU-8 photoresists. By this method, fabrication of both holographic and blazed angle grating were successfully demonstrated. An in-depth characterization of the optical device was conducted to obtain the transmittance function, and the refractive index of the material. The shape and surface profile were extracted and analyzed from SEM and AFM, respectively, and they showed a good indication in terms of the proof of concept in fabrication. The diffraction efficiencies of the grating were calculated and compared with the theoretical value. The 1^{st} order diffraction efficiency of the replicated grating was found to be slightly lower than that of the master grating. This reduction in efficiency is due to the multiple replication process (*i.e.* mold preparation and transfer to the SU-8 resists) and polymer shrinkage eventually leading to reduction in height profile. However, it could be rectified by taking into

consideration the tolerance during the preparation of the mold. This technology has huge potential in the applications where optical elements need to be imprinted on the desired patterns along with alignment and integrations.

Finally, the method of integrating the optical element with the actuator was demonstrated by pick and place mechanism. One of the major challenges faced during the integration process was about the precise control of the volume of glue, which often resulted in dispensing large volume of optical adhesive on to the actuator. The system can be further improved by using a low volume syringe with a piezo actuation dispensing system. In this study, the integration was performed manually, which can be further improved by automated systems by programming the motor controlled x-y-z stage and dispensing system. The process of making a dedicated actuator for driving optical elements opens up the possibility of future deployment and mass production of dedicated devices. In addition to diversity in imaging spectroscopy, the device has significant potential in scanning systems, spectral sensing, and display technologies.

Chapter 6

Conclusion and future work

6.1 Conclusions and discussions

A detailed study of hyperspectral imaging systems and state-of-the-art implementation schemes was discussed by geometrical optics. Various optical configurations were analyzed for snapshot imaging systems to capture the spatial-spectral 3D datacube. Most flavors of snapshot technology face a trade-off between spatial-spectral resolution, and this work was an attempt to counter this challenge employing computational algorithms and optical diversity techniques. It resulted in the improvement of spatial resolution by close packing of microlens and preserving the snapshot advantage at the same time.

For implementing robust computational algorithm schemes, diverse measurement schemes were adopted in the design. Based on the ray tracing simulation results, it was concluded that tuning of the diffraction grating ensures optical transfer function diversity, which was utilized together with reconstruction algorithm. Ray tracing analysis demonstrated by tuning pitch or rotation of grating produces

the desired outcome in the optical transfer function of integral field spectroscopy (IFS).

Pitch tunable diffraction grating for diversity implementation in IFS is realized by micromachining technology. The design, fabrication, and testing of the pitch tunable grating (PTG) were performed on an SOI wafer. The design was optimized for a relatively large resolving power that is very significant for high spectral resolution if the number of measurements captured are limited. However, a larger resolving power requires a bigger grating with more number of grating groves, which leads to a decline in the tuning range. Since the tuning range of the electrostatic actuation was limited, another possibility could be the fabrication of grating with a smaller period, which was difficult from technological perspective. Due to the fabrication tolerance and limitations in the photolithographic resolution, the PTG is difficult to fabricate with sufficiently high fill factor and possessing a broad tuning range at the same time.

Concerning fabrication feasibility, tuning of the diffraction grating utilizing rotation was found to have an advantage over the PTG in obtaining the desired optical diversity. Fabrication of the diffraction grating and rotary actuator separately retains the benefit of obtaining a high quality actuator and a highly optically efficient diffraction grating. The rotary actuator fabricated with stepping motion, was designed, fabricated on an SOI wafer, characterized and tested. The stepping motion sequence of the rotor using electrostatic actuation was obtained with the application of a 3-phase half stepping voltage sequence. This provides an excellent advantage over most comb-drive devices, where the device operates at high-frequency resonant modes, which are difficult to be captured by conventional

CCD/CMOS imaging cameras. The diffraction grating was fabricated using replication techniques. The proof of concept showing technological development was demonstrated by fabricating the diffraction grating on an SU-8 photoresist and later patterned as required. Replication allows making a blazed angle grating that is difficult to achieve by conventional photolithographic techniques. Finally, an integrating procedure of the actuator with the optical element was demonstrated. Integration of optics with MEMS could possibly open up a new pathway of carving MOEMS devices for their future deployment in imaging spectroscopic systems.

6.2 Major contributions

- This work gave an entry into the quasi-snapshot imaging spectrometer with diversity techniques and computational imaging by overcoming detector size limitation, and hence the spatial-spectral tradeoff that was faced by the conventional hyperspectral imager.

- The work also explored the possibilities of deployment of MEMS technology in imaging, which would be a reality in the future development of a miniaturized imaging spectrometer. Two methods of tuning the optical element were presented, and the tunable diffraction grating was designed and fabricated.

- A pitch tunable diffraction grating with relatively large fill factor was fabricated by silicon micromachining, and performance analyses were carried out.

- A rotary micro stepper motor for driving the diffraction grating was designed and fabricated, which was compatible with imaging systems that use conven-

tional CCD/CMOS cameras.

- Proof of concept validation of fabrication of optical elements by replication on top of SU-8 photoresists followed by lithography patterning to achieve desired footprint was demonstrated.

- Technological development perspectives of the integration of the MEMS device with optical elements were explored.

6.3 Future perspectives

6.3.1 Plenoptic imaging spectrometer

The imaging spectrometer that is discussed in this report is designed for obtaining a 3-dimensional dataset (2 spatial and one spectral information). However, in case of light field or plenoptic imaging, with the introduction of the lenslet array, it is also possible to obtain angular information. In the present optical system, the angular information is suppressed as it leads to complexity in computation. Hence, by proper optics together with efficient reconstruction algorithms, it would be possible to extract 5D information $I(x, y, \alpha_x, \alpha_y, \lambda)$. This might provide the depth information, along with the refocusing mechanism of the object similar to a light field photography [68, 147].

6.3.2 Spatial resolution improvement with diffusive structures

Imaging spectrometer specifications are related to a number of spatial-spectral band requirements. Based on this, the optical configuration can be designed or modified. In the present IFS system, number of microlenses in the MLA defines number of spatial samples in the datacube. However, for applications such as medical imaging, larger number of spatial samples is desirable, that would provide larger field of view (FOV) for the system. Larger FOV would allow fast imaging of large areas of tissue in vivo that could be used in ophthalmology for retinal imaging in order to diagnose hypertension or diabetic-related disorders [148]. Hence, another future perspective could be an improvement in the spatial resolution of the 3D dataset.

One of the possibilities to address this issue is by replacing the regular microlens array by engineered diffusive structures, which is a middle ground between an optical diffuser and a microlens array. This could be used to randomly sample the spatial part of the spectral datacube. A similar approach was employed by Antipa *et al.* [149] for obtaining compressive measurements of 3D (x, y, z) scenes.

Instead of getting a circular-spot as the point-spread-function (PSF), engineered diffusive structures produce complex extended PSF. This assures that each point is measured at several places on the detector and a high level of compressiveness can be obtained. The spectral data can be separated out effectively owing to the multiple mixing of the dispersion between neighboring spatial pixels. Such structures of desired shape could be realized by MEMS technology, and can be replicated on hard materials. Preliminary results of a sparse array of elements for

an engineered diffuser are shown in figure 6.1a-c.

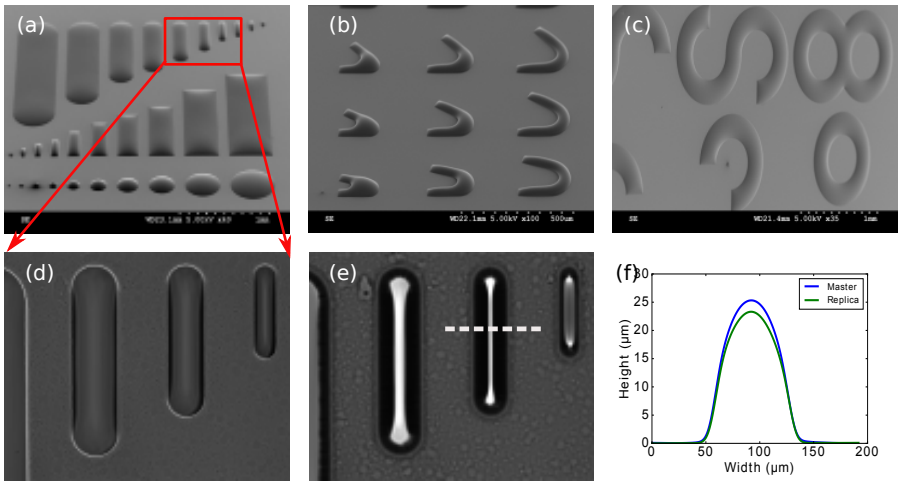

Figure 6.1: (a)-(c) Sparse structures for engineered diffusers fabricated by resist reflow technique, (d)-(e) structures replicated on top of the SU-8, measured with Olympus IX73 microscope in transmissive mode, (f) surface cross-sectional profile showing a comparison between the mold and the fabricated lens.

The desired structures were patterned by AZ-9260 photoresist by contact photolithography and shaped into a lens like structure by geometry guided reflow technique. The reflow technique, followed by etching is a well experimented and successful technology for microlens fabrication at wafer level [150, 151]. Here the reflow technique was employed for obtaining lens profiles for various shapes. Later, a soft polymer mold was fabricated with PDMS and used for replicating these structures on top of the SU-8 resist. The fabrication procedure on SU-8 is similar to the method described in section 5.4.1 for realizing the diffraction grating. One of the challenges faced in fabricating deep structured devices was formation of the voids during replication. It was prevented by spin coating a thin layer of resist on the soft mold and baking it in a convection oven before molding. The fabricated structures

were viewed under a transmissive microscope and depicted in figure 6.1d-e. The focusing effect of the lenses was also observed on the replicated structure. Replication quality was investigated by measuring the surface cross-sectional profile of the mold and the replicated structure using a confocal microscope. The result obtained was plotted in figure 6.1f shows that deep, smooth shape was well replicated. By reducing the dimensions of such structures and with close packing, the diffusive surface can be realized.

Another way of making the diffusive surface is by surface modification, followed by a replication technique, results in formation of highly ordered diffusive micro-patterns. Preliminary results of fabrication of the diffusive surface on top of the polymer microlenses, to further refine the spatial resolution, are shown in figure 6.2. Testing, characterization and optical experiments will be performed in the future course of time for such structures.

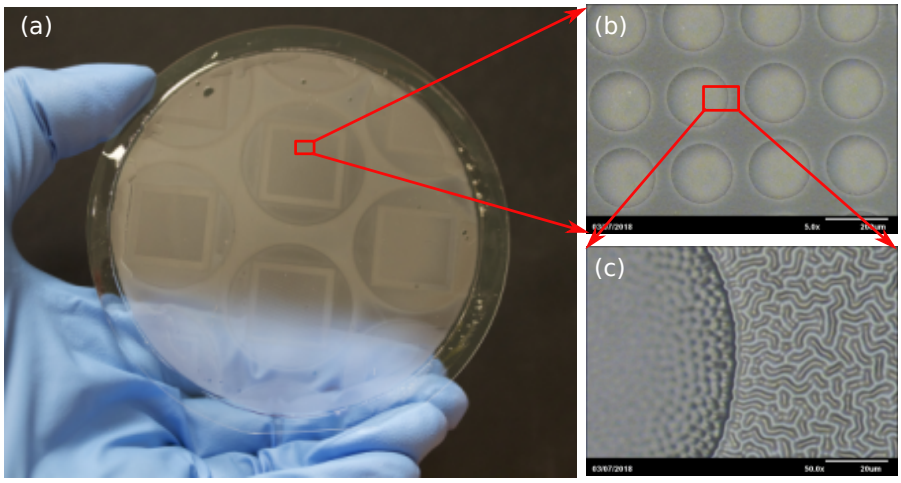

Figure 6.2: (a) Diffusive surface formed on top of the polymer lens, (b) microscopic image of an array of microlens, and (c) quasi-random diffusive micro structures.

6.3.3 Application specific optical design for IFS

The optical analysis carried out in chapter 3 discussed the design of IFS using geometrical ray tracing. The simulations were carried with paraxial approximation without considering the aberrations. However, for the hardware realization, the aberration in the lens is one of the main problems that degrade the imaging quality. For example, chromatic aberration is the inability to focus all the wavelength to a common point due to the change in the refraction angle at the curvature of the lens for multiple wavelengths. Besides that, while considering a broad spectrum, there could be the cases where the wavelength that has larger refraction angle, may produce non-circular spot at the detector. Hence, imaging conditions have to be taken care while carrying out the experimental demonstrations. Designing custom-made lenses or adding additional optics to the system would minimize the aberrations of the IFS.

Additionally, the conventional CCD/CMOS camera responds only to VIS-NIR wavelength and may not be suitable for FIR wavelengths. Hence, the camera also needs to be selectively chosen based on the materials that are of interest (by looking into the unique spectral signatures in the electromagnetic spectrum). Hardware realization of IFS for a specific wavelength range will also be carried out in the future.

Bibliography

[1] E. Betzig and J. K. Trautman, "Near-field optics: microscopy, spectroscopy, and surface modification beyond the diffraction limit," *Science*, vol. 257, no. 5067, pp. 189–195, 1992.

[2] F. Eisenhauer and W. Raab, "Visible/infrared imaging spectroscopy and energy-resolving detectors," *Annual Review of Astronomy and Astrophysics*, vol. 53, pp. 155–197, 2015.

[3] B. E. Bayer, "Color imaging array," July 20 1976. US Patent 3,971,065.

[4] A. Rissanen, A. Akujärvi, J. Antila, M. Blomberg, and H. Saari, "Moems miniature spectrometers using tuneable fabry-perot interferometers," *Journal of Micro/Nanolithography, MEMS, and MOEMS*, vol. 11, no. 2, pp. 023003–1, 2012.

[5] T. S. Rappaport *et al.*, *Wireless communications: principles and practice*, vol. 2. prentice hall PTR New Jersey, 1996.

[6] I. Katzela and M. Naghshineh, "Channel assignment schemes for cellular mobile telecommunication systems: A comprehensive survey," *IEEE personal communications*, vol. 3, no. 3, pp. 10–31, 1996.

[7] S. M. Alamouti, "A simple transmit diversity technique for wireless communications," *IEEE Journal on selected areas in communications*, vol. 16, no. 8, pp. 1451–1458, 1998.

[8] H. Hourani, "An overview of diversity techniques in wireless communication systems," *IEEE ISAC, pp-1200-5*, 2004.

[9] R. L. Kendrick, D. S. Acton, and A. Duncan, "Phase-diversity wave-front sensor for imaging systems," *Applied Optics*, vol. 33, no. 27, pp. 6533–6546, 1994.

[10] L. Waller, L. Tian, and G. Barbastathis, "Transport of intensity phase-amplitude imaging with higher order intensity derivatives," *Optics express*, vol. 18, no. 12, pp. 12552–12561, 2010.

[11] A. Rissanen, U. Kantojärvi, M. Blomberg, J. Antila, and S. Eränen, "Monolithically integrated microspectrometer-on-chip based on tunable visible light mems fpi," *Sensors and Actuators A: Physical*, vol. 182, pp. 130–135, 2012.

[12] Y. Wang, S. Bish, J. W. Tunnell, and X. Zhang, "Mems scanner enabled real-time depth sensitive hyperspectral imaging of biological tissue," *Optics express*, vol. 18, no. 23, pp. 24101–24108, 2010.

[13] A. F. Goetz, G. Vane, J. E. Solomon, and B. N. Rock, "Imaging spectrometry for earth remote sensing," *science*, vol. 228, no. 4704, pp. 1147–1153, 1985.

[14] M. D. King, Y. J. Kaufman, W. P. Menzel, and D. Tanre, "Remote sensing of cloud, aerosol, and water vapor properties from the moderate resolution

imaging spectrometer (modis)," *IEEE Transactions on Geoscience and Remote Sensing*, vol. 30, no. 1, pp. 2–27, 1992.

[15] J. Burrows, E. Hölzle, A. Goede, H. Visser, and W. Fricke, "Sciamachy—scanning imaging absorption spectrometer for atmospheric chartography," *Acta Astronautica*, vol. 35, no. 7, pp. 445–451, 1995.

[16] P. J. Curran, "Remote sensing of foliar chemistry," *Remote sensing of Environment*, vol. 30, no. 3, pp. 271–278, 1989.

[17] P. Zarco-Tejada, J. Miller, G. Mohammed, T. Noland, and P. Sampson, "Vegetation stress detection through chlorophyll+ estimation and fluorescence effects on hyperspectral imagery," *Journal of environmental quality*, vol. 31, no. 5, pp. 1433–1441, 2002.

[18] J. Clevers, "The use of imaging spectrometry for agricultural applications," *ISPRS Journal of Photogrammetry and Remote sensing*, vol. 54, no. 5-6, pp. 299–304, 1999.

[19] D. Wu and D.-W. Sun, "Advanced applications of hyperspectral imaging technology for food quality and safety analysis and assessment: A review—part i: Fundamentals," *Innovative Food Science & Emerging Technologies*, vol. 19, pp. 1–14, 2013.

[20] D. Wu and D.-W. Sun, "Advanced applications of hyperspectral imaging technology for food quality and safety analysis and assessment: A review—part ii: Applications," *Innovative Food Science & Emerging Technologies*, vol. 19, pp. 15–28, 2013.

[21] C. Brekke and A. H. Solberg, "Oil spill detection by satellite remote sensing," *Remote sensing of environment*, vol. 95, no. 1, pp. 1–13, 2005.

[22] S. R. Arridge, "Optical tomography in medical imaging," *Inverse problems*, vol. 15, no. 2, p. R41, 1999.

[23] B. Khoobehi, J. M. Beach, and H. Kawano, "Hyperspectral imaging for measurement of oxygen saturation in the optic nerve head," *Investigative ophthalmology & visual science*, vol. 45, no. 5, pp. 1464–1472, 2004.

[24] M. E. Martin, M. B. Wabuyele, K. Chen, P. Kasili, M. Panjehpour, M. Phan, B. Overholt, G. Cunningham, D. Wilson, R. C. DeNovo, *et al.*, "Development of an advanced hyperspectral imaging (hsi) system with applications for cancer detection," *Annals of biomedical engineering*, vol. 34, no. 6, pp. 1061–1068, 2006.

[25] R. T. Kester, N. Bedard, L. S. Gao, and T. S. Tkaczyk, "Real-time snapshot hyperspectral imaging endoscope," *Journal of biomedical optics*, vol. 16, no. 5, p. 056005, 2011.

[26] G. Lammel, S. Schweizer, S. Schiesser, and P. Renaud, "Tunable optical filter of porous silicon as key component for a mems spectrometer," *Journal of microelectromechanical systems*, vol. 11, no. 6, pp. 815–828, 2002.

[27] R. F. Wolffenbuttel, "Mems-based optical mini-and microspectrometers for the visible and infrared spectral range," *Journal of Micromechanics and Microengineering*, vol. 15, no. 7, p. S145, 2005.

[28] J. Antila, M. Tuohiniemi, A. Rissanen, U. Kantojärvi, M. Lahti, K. Viherkanto, M. Kaarre, and J. Malinen, "Mems-and moems-based near-infrared spectrometers," *Encyclopedia of Analytical Chemistry*, 2014.

[29] M. Kraft, A. Kenda, A. Frank, W. Scherf, A. Heberer, T. Sandner, H. Schenk, and F. Zimmer, "Single-detector micro-electro-mechanical scanning grating spectrometer," *Analytical and bioanalytical chemistry*, vol. 386, no. 5, pp. 1259–1266, 2006.

[30] S. C. Truxal, K. Kurabayashi, and Y.-C. Tung, "Design of a mems tunable polymer grating for single detector spectroscopy," *International Journal of Optomechatronics*, vol. 2, no. 2, pp. 75–87, 2008.

[31] Ximea, *50 Megapixels Monochrome CMOS camera with CMOSIS CMV50000.*

[32] Kodak, *KAF-50100 Image Sensor, in: Kodak Products.*

[33] R. Robucci, J. D. Gray, L. K. Chiu, J. Romberg, and P. Hasler, "Compressive sensing on a cmos separable-transform image sensor," *Proceedings of the IEEE*, vol. 98, no. 6, pp. 1089–1101, 2010.

[34] S. Svanberg, *Atomic and molecular spectroscopy: basic aspects and practical applications*, vol. 6. Springer Science & Business Media, 2012.

[35] B. R. Judd, *Operator techniques in atomic spectroscopy.* Princeton University Press, 2014.

[36] C. N. Banwell, E. M. McCash, *et al.*, *Fundamentals of molecular spectroscopy*, vol. 851. McGraw-Hill New York, 1994.

[37] Ucdavis-ChemWiki-Spectrophotometry, *http://chemwiki.ucdavis.edu/Core/Physical-Chemistry/Kinetics/Reaction-Rates/Experimental-Determination-of-Kinetcs/ Spectrophotometry/*.

[38] Imaging Spectroscopy, *http://www.apex-esa.org/content/imaging-spectroscopy*.

[39] A. F. Goetz and M. Herring, "The high resolution imaging spectrometer (hiris) for eos," *Geoscience and Remote Sensing, IEEE Transactions on*, vol. 27, no. 2, pp. 136–144, 1989.

[40] S. E. Dunagan, R. Johnson, J. Zavaleta, P. B. Russell, B. Schmid, C. Flynn, J. Redemann, Y. Shinozuka, J. Livingston, and M. Segal-Rosenhaimer, "Spectrometer for sky-scanning sun-tracking atmospheric research (4star): Instrument technology," *Remote Sensing*, vol. 5, no. 8, pp. 3872–3895, 2013.

[41] R. D. McPeters, P. Bhartia, A. J. Krueger, J. R. Herman, B. M. Schlesinger, C. G. Wellemeyer, C. J. Seftor, G. Jaross, S. L. Taylor, T. Swissler, *et al.*, "Nimbus-7 total ozone mapping spectrometer (toms) data products user's guide," tech. rep., NASA; Greenbelt, MD United States, 1996.

[42] C. G. Wellemeyer, P. K. Bhartia, S. L. Taylor, W. Qin, and C. Ahn, "Version 8 total ozone mapping spectrometer (toms) algorithm," in *Proceedings of the XX Quadrennial Ozone Symposium*, vol. 1, 2004.

[43] J. P. Burrows, M. Buchwitz, V. Rozanov, M. Weber, a. Richter, a. Ladstätter-Weiß enmayer, and M. Eisinger, "The Global Ozone Monitoring Experiment (GOME): Mission, instrument concept, and first scientific results," *European Space Agency, (Special Publication) ESA SP*, vol. 1, pp. 585–590, 1997.

[44] C. Leue, M. Weing, and T. Wagner, "Quantitative analysis of NO(x) emissions from Global Ozone Monitoring Experiment satellite image sequences," *Journal of Geophysical Research*, vol. 106, pp. 5493–5505, 2001.

[45] H. Bovensmann, J. P. Burrows, M. Buchwitz, J. Frerick, S. Noël, V. V. Rozanov, K. V. Chance, and a. P. H. Goede, "SCIAMACHY: Mission Objectives and Measurement Modes," *Journal of the Atmospheric Sciences*, vol. 56, pp. 127–150, 1999.

[46] Tropospheric Emission Monitoring Internet Service, *http://www.temis.nl/airpollution/no2.html*.

[47] G. Lu and B. Fei, "Medical hyperspectral imaging: a review," *Journal of biomedical optics*, vol. 19, no. 1, p. 010901, 2014.

[48] A. Gowen, C. O'Donnell, P. Cullen, G. Downey, and J. Frias, "Hyperspectral imaging–an emerging process analytical tool for food quality and safety control," *Trends in Food Science & Technology*, vol. 18, no. 12, pp. 590–598, 2007.

[49] D.-W. Sun, *Hyperspectral imaging for food quality analysis and control*. Elsevier, 2010.

[50] L. M. Dale, A. Thewis, C. Boudry, I. Rotar, P. Dardenne, V. Baeten, and J. A. F. Pierna, "Hyperspectral imaging applications in agriculture and agro-food product quality and safety control: a review," *Applied Spectroscopy Reviews*, vol. 48, no. 2, pp. 142–159, 2013.

[51] D. Lorente, N. Aleixos, J. Gómez-Sanchis, S. Cubero, O. L. García-Navarrete, and J. Blasco, "Recent advances and applications of hyperspectral imaging for fruit and vegetable quality assessment," *Food and Bioprocess Technology*, vol. 5, no. 4, pp. 1121–1142, 2012.

[52] Rebellion Photonics, *https://rebellionphotonics.com*.

[53] H. Liang, "Advances in multispectral and hyperspectral imaging for archaeology and art conservation," *Applied Physics A*, vol. 106, no. 2, pp. 309–323, 2012.

[54] C. M. Stellman, F. M. Olchowski, and J. V. Michalowicz, "War horse (wide-area reconnaissance: hyperspectral overhead real-time surveillance experiment)," in *Automatic Target Recognition XI*, vol. 4379, pp. 339–347, International Society for Optics and Photonics, 2001.

[55] C. Fischer and I. Kakoulli, "Multispectral and hyperspectral imaging technologies in conservation: current research and potential applications," *Studies in Conservation*, vol. 51, no. sup1, pp. 3–16, 2006.

[56] H. Sagberg, M. Lacolle, I.-R. Johansen, O. Lvhaugen, R. Belikov, O. Solgaard, and A. Sudb, "Micromechanical gratings for visible and near-infrared spectroscopy," *IEEE Journal of Selected Topics in Quantum Electronics*, vol. 10, no. 3, pp. 604–613, 2004.

[57] T. Egloff, J. Knobbe, S. Sinzinger, and H. Grüger, "Design of a micro-opto-electro-mechanical-system-based near-infrared hyperspectral imager.," *Applied optics*, vol. 48, no. 34, pp. 6583–6593, 2009.

[58] R. Mannila, A. Näsilä, K. Viherkanto, C. Holmlund, I. Näkki, and H. Saari, "Spectral imager based on fabry-perot interferometer for aalto-1 nanosatellite," in *SPIE Optical Engineering+ Applications*, pp. 887002–887002, International Society for Optics and Photonics, 2013.

[59] H. Saari, V.-V. Aallos, C. Holmlund, J. Mäkynen, B. Delauré, K. Nackaerts, and B. Michiels, "Novel hyperspectral imager for lightweight uavs," in *SPIE Defense, Security, and Sensing*, pp. 766805–766805, International Society for Optics and Photonics, 2010.

[60] J. Antila, A. Miranto, J. Mäkynen, M. Laamanen, A. Rissanen, M. Blomberg, H. Saari, and J. Malinen, "Mems and piezo actuator-based fabry-perot interferometer technologies and applications at vtt," in *SPIE Defense, Security, and Sensing*, pp. 76800U–76800U, International Society for Optics and Photonics, 2010.

[61] N. Gupta and R. Dahmani, "Multispectral and hyperspectral imaging with aotf for object recognition," in *The 27th AIPR Workshop: Advances in Computer-Assisted Recognition*, pp. 128–135, International Society for Optics and Photonics, 1999.

[62] P. J. Miller and C. C. Hoyt, "Multispectral imaging with a liquid crystal tunable filter," in *Photonics for Industrial Applications*, pp. 354–365, International Society for Optics and Photonics, 1995.

[63] Q. Li, X. He, Y. Wang, H. Liu, D. Xu, and F. Guo, "Review of spectral imaging technology in biomedical engineering: achievements and challenges," *Journal of biomedical optics*, vol. 18, no. 10, pp. 100901–100901, 2013.

[64] G. Lippmann, "La photographic integrale," *CR Acad. Sci.*, vol. 146, pp. 446–451, 1908.

[65] Lytro, *https://www.lytro.com/*.

[66] Pelican Imaging, *http://lightfield-forum.com/tag/pelican-imaging/*.

[67] Adobe, *http://lightfield-forum.com/light-field-camera-prototypes/adobelightfield-camera- protypes/*.

[68] R. Ng, M. Levoy, M. Brédif, G. Duval, M. Horowitz, and P. Hanrahan, "Light field photography with a hand-held plenoptic camera," *Computer Science Technical Report CSTR*, vol. 2, no. 11, pp. 1–11, 2005.

[69] M. Levoy, "Light fields and computational imaging," *Computer*, vol. 39, pp. 46–55, 2006.

[70] A. Côté, S. Levasseur, S. Boudreau, and J. Genest, "Light field camera as a fourier transform spectrometer sensor: instrument characterization and passive spectral ranging," *Applied optics*, vol. 53, no. 19, pp. 4327–4333, 2014.

[71] M. Bertero and P. Boccacci, *Introduction to inverse problems in imaging*. CRC press, 1998.

[72] M. Bertero, C. De Mol, and E. R. Pike, "Linear inverse problems with discrete data: Ii. stability and regularisation," *Inverse problems*, vol. 4, no. 3, p. 573, 1988.

[73] E. Candes and M. Wakin, "An Introduction To Compressive Sampling," *IEEE Signal Processing Magazine*, vol. 25, no. March 2008, pp. 21–30, 2008.

[74] D. Brady and M. Gehm, "Compressive imaging spectrometers using coded apertures," *Defense and ...*, vol. 6246, pp. 62460A–62460A–9, 2006.

[75] D. Kittle, K. Choi, A. Wagadarikar, and D. J. Brady, "Multiframe image estimation for coded aperture snapshot spectral imagers," *Applied optics*, vol. 49, no. 36, pp. 6824–6833, 2010.

[76] M. F. Duarte, M. A. Davenport, D. Takhar, J. N. Laska, T. Sun, K. E. Kelly, R. G. Baraniuk, *et al.*, "Single-pixel imaging via compressive sampling," *IEEE Signal Processing Magazine*, vol. 25, no. 2, p. 83, 2008.

[77] A. Wagadarikar, R. John, R. Willett, and D. Brady, "Single disperser design for coded aperture snapshot spectral imaging.," *Applied optics*, vol. 47, pp. B44–B51, 2008.

[78] P. Jacquinot, "The luminosity of spectrometers with prisms, gratings, or fabry-perot etalons," *JOSA*, vol. 44, no. 10, pp. 761–765, 1954.

[79] J. E. Jaskie, "Tunable diffraction grating," May 19 1992. US Patent 5,115,344.

[80] R. Jung and E. Hellerich, "Tunable diffraction grating," Mar. 1 2018. US Patent App. 15/247,307.

[81] J. Strong, "New johns hopkins ruling engine," *JOSA*, vol. 41, no. 1, pp. 3–15, 1951.

[82] H. D. Babcock and H. W. Babcock, "The ruling of diffraction gratings at the mount wilson observatory," *JOSA*, vol. 41, no. 11, pp. 776–786, 1951.

[83] T. L. Koch, F. W. Ostermayer Jr, D. M. Tennant, and J.-M. Verdiell, "Grating fabrication using electron beam lithography," May 9 1995. US Patent 5,413,884.

[84] G. P. Behrmann and M. T. Duignan, "Excimer laser micromachining for rapid fabrication of diffractive optical elements," *Applied optics*, vol. 36, no. 20, pp. 4666–4674, 1997.

[85] O. J. a. Schueller, D. C. Duffy, J. a. Rogers, S. T. Brittain, and G. M. Whitesides, "Reconfigurable diffraction gratings based on elastomeric microfluidic devices," *Sensors and Actuators, A: Physical*, vol. 78, no. 2, pp. 149–159, 1999.

[86] M. Aschwanden and A. Stemmer, "Polymeric, electrically tunable diffraction grating based on artificial muscles," *Optics letters*, vol. 31, no. 17, pp. 2610–2612, 2006.

[87] M. Aschwanden, M. Beck, and A. Stemmer, "Diffractive transmission grating tuned by dielectric elastomer actuator," *Photonics Technology Letters, IEEE*, vol. 19, no. 14, pp. 1090–1092, 2007.

[88] C. W. Wong, Y. Jeon, G. Barbastathis, and S.-G. Kim, "Analog piezoelectric-driven tunable gratings with nanometer resolution," *Journal of microelectromechanical systems*, vol. 13, no. 6, pp. 998–1005, 2004.

[89] C. W. Wong, Y. Jeon, G. Barbastathis, and S.-G. Kim, "Analog tunable gratings driven by thin-film piezoelectric microelectromechanical actuators.," *Applied optics*, vol. 42, no. 4, pp. 621–626, 2003.

[90] S. D. Senturia, D. R. Day, M. a. Butler, and M. C. Smith, "Programmable diffraction gratings and their uses in displays, spectroscopy, and communications," *Journal of Microlithography, Microfabrication, and Microsystems*, vol. 4, no. 4, p. 041401, 2005.

[91] Y.-S. Yang, Y.-H. Lin, Y.-C. Hu, and C.-H. Liu, "A large-displacement thermal actuator designed for mems pitch-tunable grating," *Journal of Micromechanics and Microengineering*, vol. 19, no. 1, p. 015001, 2008.

[92] W. C. Shih, S. G. Kim, and G. Barbastathis, "High-resolution electrostatic analog tunable grating with a single-mask fabrication process," *Journal of Microelectromechanical Systems*, vol. 15, no. 4, pp. 763–769, 2006.

[93] Y.-T. Yu, W.-Z. Yuan, T.-P. Li, and B. Yan, "Development of a micromechanical pitch-tunable grating with reflective/transmissive dual working modes," *Journal of Micromechanics and Microengineering*, vol. 20, no. 6, p. 065002, 2010.

[94] Sandia Laboratory Group, *http://mems.sandia.gov/scripts/index.asp*.

[95] T.-S. Lim, C.-H. Ji, C.-H. Oh, H. Kwon, Y. Yee, and J. U. Bu, "Electrostatic mems variable optical attenuator with rotating folded micromirror," *Selected Topics in Quantum Electronics, IEEE Journal of*, vol. 10, no. 3, pp. 558–562, 2004.

[96] J. A. Yeh, C.-N. Chen, and Y.-S. Lui, "Large rotation actuated by in-plane rotary comb-drives with serpentine spring suspension," *Journal of Micromechanics and Microengineering*, vol. 15, no. 1, p. 201, 2004.

[97] J. A. Yeh, S.-S. Jiang, and C. Lee, "Moems variable optical attenuators using rotary comb drive actuators," *IEEE photonics technology letters*, vol. 18, no. 9-12, pp. 1170–1172, 2006.

[98] H. Yu, G. Zhou, S. K. Sinha, and F. S. Chau, "Scanning grating based in-plane movement sensing," *Journal of Micromechanics and Microengineering*, vol. 20, no. 8, p. 085007, 2010.

[99] E. Sarajlic, C. Yamahata, M. Cordero, L. Jalabert, T. Iizuka, and H. Fujita, "Single mask 3-phase electrostatic rotary stepper micromotor," in *Solid-State Sensors, Actuators and Microsystems Conference, 2009. TRANSDUCERS 2009. International*, pp. 1505–1508, IEEE, 2009.

[100] A. A. Yasseen, S. W. Smith, F. L. Merat, and M. Mehregany, "Diffraction grating scanners using polysilicon micromotors," *IEEE Journal of selected topics in quantum electronics*, vol. 5, no. 1, pp. 75–82, 1999.

[101] S. Henein, P. Spanoudakis, S. Droz, L. I. Myklebust, and E. Onillon, "Flexure pivot for aerospace mechanisms," in *10th European Space Mechanisms and Tribology Symposium, San Sebastian, Spain*, pp. 285–288, 2003.

[102] E. Sarajlic, C. Yamahata, M. Cordero, and H. Fujita, "Three-Phase Electrostatic Rotary Stepper Micromotor With a Flexural Pivot Bearing," *Journal of Microelectromechanical Systems*, vol. 19, no. 2, pp. 338–349, 2010.

[103] M. Stranczl, E. Sarajlic, H. Fujita, M. a. M. Gijs, and C. Yamahata, "High-angular-range electrostatic rotary stepper micromotors fabricated with SOI technology," *Journal of Microelectromechanical Systems*, vol. 21, no. 3, pp. 605–620, 2012.

[104] N. Hagen, R. T. Kester, L. Gao, and T. S. Tkaczyk, "Snapshot advantage: a review of the light collection improvement for parallel high-dimensional measurement systems," *Optical Engineering*, vol. 51, no. 11, pp. 111702–1, 2012.

[105] P.-J. Lapray, X. Wang, J.-B. Thomas, and P. Gouton, "Multispectral filter arrays: Recent advances and practical implementation," *Sensors*, vol. 14, no. 11, pp. 21626–21659, 2014.

[106] M. Levoy, R. Ng, A. Adams, M. Footer, and M. Horowitz, "Light field microscopy," in *ACM Transactions on Graphics (TOG)*, vol. 25, pp. 924–934, ACM, 2006.

[107] K. Klementev, "Deconvolution problems in x-ray absorption fine structure spectroscopy," *Journal of Physics D: Applied Physics*, vol. 34, no. 15, p. 2241, 2001.

[108] E. Candes and J. Romberg, "Sparsity and incoherence in compressive sampling," *Inverse problems*, vol. 23, no. 3, p. 969, 2007.

[109] D. J. Brady, *Optical imaging and spectroscopy*. John Wiley & Sons, 2009.

[110] S. P. Kim and W.-Y. Su, "Recursive high-resolution reconstruction of blurred multiframe images," *IEEE Transactions on Image Processing*, vol. 2, no. 4, pp. 534–539, 1993.

[111] A. Gerrard and J. M. Burch, *Introduction to matrix methods in optics*. Courier Corporation, 1975.

[112] M. Baranski, *Optical design and developent of building blocks for a new generation of vertically integrated on-chip confocal microscopes.* PhD thesis, Université de Franche-Comté, 2013.

[113] B. C. Platt and R. Shack, "History and principles of shack-hartmann wavefront sensing," *Journal of Refractive Surgery*, vol. 17, no. 5, pp. S573–S577, 2001.

[114] J. Schwiegerling and D. R. Neal, "Historical development of the shack-hartmann wavefront sensor," *Robert Shannon and Roland Shack: Legends in Applied Optics, edited by JE Harvey and RB Hooker—SPIE, Bellingham, WA*, pp. 132–139, 2005.

[115] Zemax, *https://www.zemax.com/*.

[116] J. Antichi, K. Dohlen, R. G. Gratton, D. Mesa, R. U. Claudi, E. Giro, A. Boccaletti, D. Mouillet, P. Puget, and J.-L. Beuzit, "Bigre: A low cross-talk integral field unit tailored for extrasolar planets imaging spectroscopy," *The Astrophysical Journal*, vol. 695, no. 2, p. 1042, 2009.

[117] M. Tormen, Y.-A. Peter, P. Niedermann, A. Hoogerwerf, H. Shea, and R. Stanley, "Deformable mems grating for wide tunability and high operating speed," in *MOEMS-MEMS 2006 Micro and Nanofabrication*, pp. 61140C–61140C, International Society for Optics and Photonics, 2006.

[118] W.-M. Zhang, H. Yan, Z.-K. Peng, and G. Meng, "Electrostatic pull-in instability in mems/nems: A review," *Sensors and Actuators A: Physical*, vol. 214, pp. 187–218, 2014.

[119] W.-C. Shih, C. Hidrovo, S.-G. Kim, and G. Barbastathis, "Optical diversity by nanoscale actuation," in *Nanotechnology, 2003. IEEE-NANO 2003. 2003 Third IEEE Conference on*, vol. 2, pp. 892–895, IEEE, 2003.

[120] M. Elad and A. Feuer, "Restoration of a single superresolution image from several blurred, noisy, and undersampled measured images," *IEEE transactions on image processing*, vol. 6, no. 12, pp. 1646–1658, 1997.

[121] Y. Wu, I. O. Mirza, G. R. Arce, and D. W. Prather, "Development of a digital-micromirror-device-based multishot snapshot spectral imaging system," *Optics letters*, vol. 36, no. 14, pp. 2692–2694, 2011.

[122] J. W. Goodman, *Introduction to Fourier optics*. Roberts and Company Publishers, 2005.

[123] J. W. Goodman and S. C. Gustafson, "Introduction to fourier optics," *Optical Engineering*, vol. 35, no. 5, pp. 1513–1513, 1996.

[124] J. Wu, S. Wang, and J. Miao, "A mems device for studying the friction behavior of micromachined sidewall surfaces," *Journal of Microelectromechanical Systems*, vol. 17, pp. 921–933, Aug 2008.

[125] J. Wu, S. Wang, and J. Miao, "Friction characteristics of the curved sidewall surfaces of a rotary mems device in oscillating motion," *Journal of Micromechanics and Microengineering*, vol. 19, no. 6, p. 065020, 2009.

[126] D. J. Bell, T. Lu, N. A. Fleck, and S. M. Spearing, "Mems actuators and sensors: observations on their performance and selection for purpose," *Journal of Micromechanics and Microengineering*, vol. 15, no. 7, p. S153, 2005.

[127] R. Legtenberg, A. Groeneveld, and M. Elwenspoek, "Comb-drive actuators for large displacements," *Journal of Micromechanics and microengineering*, vol. 6, no. 3, p. 320, 1996.

[128] S. D. Senturia, *Microsystem design*. Springer Science & Business Media, 2007.

[129] J. M. Cowley, *Diffraction physics*. Elsevier, 1995.

[130] Y. Yu, W. Yuan, R. Sun, D. Qiao, and B. Yan, "A strategy to efficiently extend the change rate of period for comb-drive micromechanical pitch-tunable gratings," *Journal of Microelectromechanical Systems*, vol. 19, no. 5, pp. 1180–1185, 2010.

[131] K. R. Williams, K. Gupta, and M. Wasilik, "Etch rates for micromachining processing-part ii," *Journal of microelectromechanical systems*, vol. 12, no. 6, pp. 761–778, 2003.

[132] J. Gao, L. Yeo, M. B. Chan-Park, J. Miao, Y. Yan, J. Sun, Y. Lam, and C. Yue, "Antistick postpassivation of high-aspect ratio silicon molds fabricated by deep-reactive ion etching," *Journal of Microelectromechanical systems*, vol. 15, no. 1, pp. 84–93, 2006.

[133] L. Fu, J. Miao, X. Li, and R. Lin, "Study of deep silicon etching for micro-gyroscope fabrication," *Applied Surface Science*, vol. 177, no. 1–2, pp. 78 – 84, 2001.

[134] J. Li, A. Liu, and Q. Zhang, "Tolerance analysis for comb-drive actuator using drie fabrication," *Sensors and Actuators A: Physical*, vol. 125, no. 2, pp. 494–503, 2006.

[135] C. Iliescu and J. Miao, "One-mask process for silicon accelerometers on pyrex glass utilising notching effect in inductively coupled plasma drie," *Electronics Letters*, vol. 39, no. 8, pp. 658–659, 2003.

[136] B. Chen and J. Miao, "Influence of deep rie tolerances on comb-drive actuator performance," *Journal of Physics D: Applied Physics*, vol. 40, no. 4, p. 970, 2007.

[137] T. Shaw, J. Corliss, D. Gundo, G. Mulenburg, G. Breit, and J. Griffith, "Simulation of shuttle launch g forces and acoustic loads using the nasa ames research center 20g centrifuge," in *18th Space Simulation Conference on Space Mission Success Through Testing*, 1994.

[138] S. Yi, S. Kim, and J. Song, "Analysis of the effect of space radiations on the nematode, caenorhabditis elegans, through the simulated space radiation," *International Journal of Astronomy and Astrophysics*, vol. 2013, 2013.

[139] C. A. Palmer and E. G. Loewen, *Diffraction grating handbook*. Newport Corporation New York, 2005.

[140] T. Aoyagi, Y. Aoyagi, and S. Namba, "High-efficiency blazed grating couplers," *Applied physics letters*, vol. 29, no. 5, pp. 303–304, 1976.

[141] E. Loewen, M. Nevière, and D. Maystre, "Grating efficiency theory as it applies to blazed and holographic gratings," *Applied optics*, vol. 16, no. 10, pp. 2711–2721, 1977.

[142] S. Henein, *Conception des structures articulées à guidages flexibles de haute précision*. PhD thesis, École polytechnique fédérale de Lausanne, 2000.

[143] X. Pei, J. Yu, G. Zong, and S. Bi, "A family of butterfly flexural joints: Q-litf pivots," *Journal of Mechanical Design*, vol. 134, no. 12, p. 121005, 2012.

[144] M. Stranczl, E. Sarajlic, G. J. Krijnen, H. Fujita, M. A. Gijs, and C. Yamahata, "Modal analysis and modeling of a frictionless electrostatic rotary stepper micromotor," in *Micro Electro Mechanical Systems (MEMS), 2011 IEEE 24th International Conference on*, pp. 1257–1260, IEEE, 2011.

[145] S. Henein, *Conception des guidages flexibles*. PPUR presses polytechniques, 2001.

[146] C. Chung and M. Allen, "Uncrosslinked su-8 as a sacrificial material," *Journal of Micromechanics and Microengineering*, vol. 15, no. 1, p. N1, 2004.

[147] R. Ng, *Digital light field photography*. stanford university California, 2006.

[148] W. R. Johnson, D. W. Wilson, W. Fink, M. S. Humayun, and G. H. Bearman, "Snapshot hyperspectral imaging in ophthalmology," *Journal of biomedical optics*, vol. 12, no. 1, p. 014036, 2007.

[149] N. Antipa, G. Kuo, R. Heckel, B. Mildenhall, E. Bostan, R. Ng, and L. Waller, "Diffusercam: lensless single-exposure 3d imaging," *Optica*, vol. 5, no. 1, pp. 1–9, 2018.

[150] P. Nussbaum, R. Voelkel, H. P. Herzig, M. Eisner, and S. Haselbeck, "Design, fabrication and testing of microlens arrays for sensors and microsystems," *Pure and applied optics: Journal of the European optical society part A*, vol. 6, no. 6, p. 617, 1997.

[151] A. Schilling, R. Merz, C. Ossmann, and H. P. Herzig, "Surface profiles of reflow microlenses under the influence of surface tension and gravity," *Optical Engineering*, vol. 39, no. 8, pp. 2171–2177, 2000.

Appendix A

ABCD-EF formalism

A.1 Design description

The optical system behavior of different elements or interfaces are described by:

- Free space propagation (or medium with constant refractive index)

$$P_z = \begin{bmatrix} 1 & z & 0 \\ 0 & 1 & 0 \\ 0 & 0 & 1 \end{bmatrix} \tag{A.1}$$

- Refraction at a flat interface with refractive index of medium (n_1) and medium (n_2)

$$R_{1-2} = \begin{bmatrix} 1 & 0 & 0 \\ 0 & \frac{n_1}{n_2} & 0 \\ 0 & 0 & 1 \end{bmatrix} \tag{A.2}$$

- Thin lens (*i.e.* focal length (f) >> thickness of the lens)

$$L_f = \begin{bmatrix} 1 & 0 & 0 \\ -\frac{1}{f} & 1 & 0 \\ 0 & 0 & 1 \end{bmatrix} \tag{A.3}$$

- Tilt

$$T_\gamma = \begin{bmatrix} 1 & 0 & 0 \\ 0 & 1 & \gamma \\ 0 & 0 & 1 \end{bmatrix} \tag{A.4}$$

- Coordinate shift

$$C_{x_0} = \begin{bmatrix} 1 & 0 & x_0 \\ 0 & 1 & 0 \\ 0 & 0 & 1 \end{bmatrix} \tag{A.5}$$

- MLA with focal length (f_0) and with coordinate shift (x_0) can be expressed by ABCD-EF system as a product of three matrices

$$M_{mla(f,x_0)} = M_{x_0}.C_{x_0}.M_{-x_0} \tag{A.6a}$$

$$M_{mla(f,x_0)} = \begin{bmatrix} 1 & 0 & 0 \\ -\frac{1}{f} & 1 & \frac{x_0}{f} \\ 0 & 0 & 1 \end{bmatrix} \tag{A.6b}$$

Appendix B

Performance deviation analysis due to DRIE tolerances

The etching by Bosch process produces tapered profiles that depends on the machine and etching conditions. Schematic depiction of negatively etched profile in comb-drive fingers is shown in figure B.1. It results in a drop in electrostatic force generated between comb-drive fingers due to the larger gap separation at the bottom ($F \propto (1/g)$). If the etching angle is θ, the equivalent capacitance for such

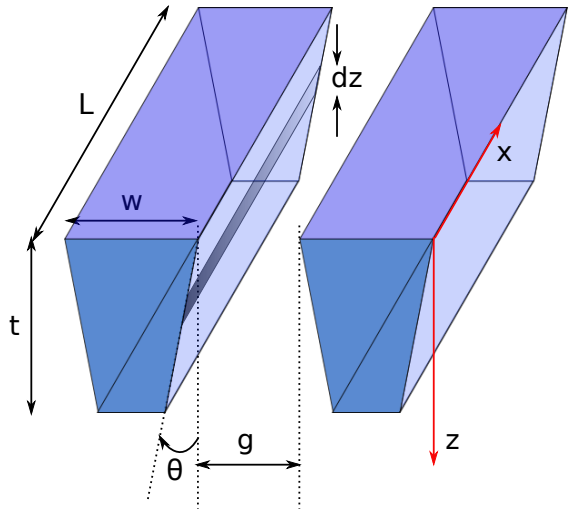

Figure B.1: Schematic depiction of negatively etch profile.

profile (figure B.1) can be computed by

$$C = 2n \int_0^t \frac{\epsilon_0 x}{g + 2z\tan\theta} dz = \frac{n\epsilon_0 x}{\tan\theta} \ln\left(1 + \frac{t}{g} \cdot 2\tan\theta\right) \tag{B.1}$$

The drop in the capacitance value manifest the electrostatic force generated between the comb drive fingers given by

$$F_{(new)} = \frac{1}{2}\frac{\partial C}{\partial x}V^2 = \frac{n\epsilon_0 V^2}{2\tan\theta} \ln\left(1 + \frac{t}{g} \cdot 2\tan\theta\right) \tag{B.2}$$

In case of positively etched profile, the 'θ' is replaced by '$-\theta$' which results in

$$F_{(new)} = -\frac{n\epsilon_0 V^2}{2\tan\theta} \ln\left(1 - \frac{t}{g} \cdot 2\tan\theta\right) \tag{B.3}$$

The etching brings positive tapered profile where the gap separation is small. In case of actuation springs, it leads to an increase in spring stiffness as the width of the beam becomes wider when it goes deeper. Figure B.2 shows the positively tapered etched profile with the etching angle ϕ. Inertial momentum for such trapezoidal cross sectional profile can be obtained by integration. The cross sectional area for such profile is obtained from figure B.2, calculated by

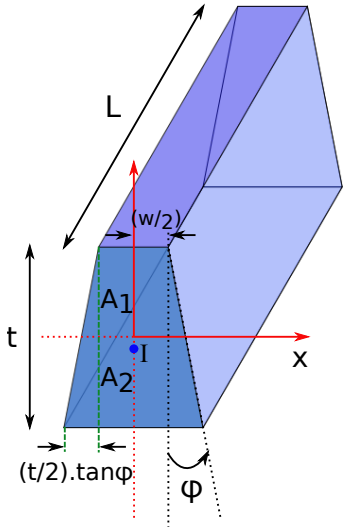

Figure B.2: Schematic of positively tapered etch profile.

$$A = A_1 + A_2 = \left(x + x - \frac{t}{2}\tan\phi\right) \cdot \frac{t}{2} + \left(x + x + \frac{t}{2}\tan\phi\right) \cdot \frac{t}{2} = 2xt \tag{B.4}$$

With reference to structural mechanics, the areal moment of inertia can be calculated by

$$I = \int_A x^2 dA = \int_0^{\frac{w}{2}+\frac{t}{2}\tan\phi} 2t \cdot x^2 dx = \frac{t}{12}\left(w + t \cdot \tan\phi\right)^3 \tag{B.5}$$

The spring stiffness in this regard is

$$k_{new}^x = 12\frac{EI}{L^3} = \frac{Et}{L^3}\left(w_a + t \cdot \tan\phi\right)^3 \tag{B.6}$$

Again, if in case of negatively etched profile, the equivalent stiffness is calculated by replacing ϕ by $-\phi$

$$k_{new}^x = \frac{Et}{L^3}\left(w_a - t \cdot \tan\phi\right)^3 \tag{B.7}$$

Appendix C

Programming codes

C.1 Wiener deconvolution for spectrum recovery (Python)

```
# Spectrum retrieval from spots


import cv2
import numpy as np
from matplotlib import pyplot as plt
import matplotlib.image as im
import scipy
from scipy.signal import convolve2d
from skimage import color, data, restoration
psf = im.imread('/Users/sanathananms/Dropbox/PhD Works/Simulation
   Files/Zemax Simulations/2016 03 31 LFIS Geometric Image analysis
   /MLA analysis/psf_wave2.png') #PSF
```

```
11 plt.figure(1)
12 plt.imshow(psf)
13
14 croppsf = psf[315:465, 575:725]          # Cropping PSF
15 gpsf = cv2.cvtColor(croppsf, cv2.COLOR_BGR2GRAY)
16 plt.figure(2)
17 plt.imshow(gpsf,'hot')                   # Kernal psf
18 plt.show()
19
20 I = im.imread('/Users/sanathananms/Dropbox/PhD Works/Simulation
      Files/Zemax Simulations/2016 03 31 LFIS Geometric Image analysis
      /MLA analysis/Image_MLA_1.png')
21 I = cv2.cvtColor(I, cv2.COLOR_BGR2GRAY)
22 Icrop = I[275:525, 575:725]              # Cropping bigimage for ease
       in computation
23 plt.figure(3)
24 plt.imshow(Icrop,'hot')
25 plt.show()
26
27 img = Icrop
28 psf =gpsf
29 deconvolved_img = restoration.wiener(img, psf, 500) #Wiener
      filtering operation with SNR= 500
30 plt.figure(4)
```

```
31 plt.imshow(deconvolved_img,'hot')
32 plt.show()
33
34 ## Line profile extraction
35 line = deconvolved_img[:,75]*10000                    ## Normalization
36 N = len(line)
37 lambd = np.linspace(471, 643, num=N)                  ## Prior
      knowledge of wavelength
38 plt.figure(5)
39 plt.plot(lambd,line,'-')
40 plt.ylim((-30,300))
41 plt.xlim((500,600))
42 plt.ylabel('Intensity')
43 plt.xlabel('Wavelength (nm)')
44 plt.show()
45 #plt.savefig('/Users/sanathananms/Dropbox/PhD Works/Simulation Files
      /Zemax Simulations/2016 03 31 LFIS Geometric Image analysis/MLA
      analysis/lineprofile.eps', format='eps', dpi=300)
```

C.2 Eigen value solutions (MATLAB)

```
1 %% Program to find the Eigen values of the mass-spring systems in
      PTG
2
```

```
3  clc;
4  clear all;
5  close all;
6
7  format long;
8  N = 84;                 % Number of Grating groves
9  ka = 0.2816;            % Spring stiffness of single element actuation
       spring
10 kh = 5.7274;            % Spring stiffness of single element holding
       spring
11
12 mh = 1.6347e-10;        % Sum of the mass of the grating beam and the
       four supporting holding beams
13 ma = 5.5926e-10         % Sum of the mass of the actuating arm and the
       mass of comb-fingers
14
15 %% Stiffness matrix generation
16
17 K = zeros(N+2,N+2);
18 for i = 1:N+2
19     for j = 1:N+2
20         if i == j
21             K(i,j)=2*kh;
22         else if abs(i-j)==1
```

```
23                K(i,j) = -kh;
24            end
25        end
26    end
27 end
28 K(1,1) = (2*ka)+kh;
29 K(N+2,N+2) = kh+(2*ka);
30
31 %% Mass matrix generation
32
33 M = zeros(N+2,N+2);
34 for i = 1:N+2
35     for j = 1:N+2
36         if i == j
37             M(i,j)=mh;
38         end
39     end
40 end
41 M(1,1) = ma;
42 M(N+2,N+2) = ma;
43
44 %% Modal analysis
45
46 [V,D] = eig(K,M);              % Eigen value calculation
```

```
47 for i = 1:N+2
48     freqs(i) = sqrt(D(i,i)); % Angular Resonant frequency
49 end
50 modes = V;
51
52 freqs = freqs/(2*pi)          % Resonant frequency (Hz)
```

C.3 Raspberry-Pi code for half-stepping motion (Python)

```
1 import RPi.GPIO as GPIO  ## Import GPIO Library
2 import time              ## Import'time' library. (Allows us to use
      sleep)
3
4 GPIO.setmode(GPIO.BOARD)                          ## Use board pin
     numbering
5 GPIO.setup(7,GPIO.IN, pull_up_down = GPIO.PUD_DOWN) ## Set-Up GPIO
     pin to OUT
6 GPIO.setup(15,GPIO.IN, pull_up_down = GPIO.PUD_DOWN) ## Set-Up GPIO
     pin to OUT
7 GPIO.setup(16,GPIO.IN, pull_up_down = GPIO.PUD_DOWN) ## Set-Up GPIO
     pin to OUT
```

```
8  GPIO.setup(18,GPIO.IN, pull_up_down = GPIO.PUD_DOWN) ## Set-Up GPIO
       pin to OUT
9  GPIO.setup(11,GPIO.OUT)                              ## Set-Up GPIO
       pin to OUT
10 GPIO.setup(12,GPIO.OUT)                              ## Set-Up GPIO
       pin to OUT
11 GPIO.setup(13,GPIO.OUT)                              ## Set-Up GPIO
       pin to OUT
12
13 speed = 1                                ## Setting timestep to 1s
14
15 ## Defining function name blink()
16
17 while 1:                                  ## Condition for infinite loop
18     if GPIO.input(7) == True:             ## Condition for clockwise
           rotation
19         print "CW step"                   ## Print current loop
20         GPIO.output(11,True)              ## Switch ON pin 11
21         GPIO.output(12,False)             ## Switch ON pin 12
22         GPIO.output(13,False)             ## Switch OFF pin 13
23         time.sleep(speed)                 ## Wait
24         print "CW step"                   ## Print current loop
25         GPIO.output(11,True)              ## Switch ON pin 11
26         GPIO.output(12,True)              ## Switch ON pin 12
```

```
27          GPIO.output(13,False)          ## Switch OFF pin 13
28          time.sleep(speed)              ## Wait
29          print "CW step"                ## Print current loop
30          GPIO.output(11,False)          ## Switch ON pin 11
31          GPIO.output(12,True)           ## Switch ON pin 12
32          GPIO.output(13,False)          ## Switch OFF pin 13
33          time.sleep(speed)              ## Wait
34          print "CW step"                ## Print current loop
35          GPIO.output(11,False)          ## Switch ON pin 11
36          GPIO.output(12,True)           ## Switch ON pin 12
37          GPIO.output(13,True)           ## Switch OFF pin 13
38          time.sleep(speed)              ## Wait
39          print "CW step"                ## Print current loop
40          GPIO.output(11,False)          ## Switch ON pin 11
41          GPIO.output(12,False)          ## Switch ON pin 12
42          GPIO.output(13,True)           ## Switch OFF pin 13
43          time.sleep(speed)              ## Wait
44          print "CW step"                ## Print current loop
45          GPIO.output(11,True)           ## Switch ON pin 11
46          GPIO.output(12,False)          ## Switch ON pin 12
47          GPIO.output(13,True)           ## Switch OFF pin 13
48          time.sleep(speed)              ## Wait
49      if GPIO.input(15) == True:         ## Condition for anticlockwise
            rotation
```

```
50        print "ACW step"              ## Print current loop
51        GPIO.output(11,True)          ## Switch ON pin 11
52        GPIO.output(12,False)         ## Switch ON pin 12
53        GPIO.output(13,True)          ## Switch OFF pin 13
54        time.sleep(speed)             ## Wait
55        print "ACW step"              ## Print current loop
56        GPIO.output(11,False)         ## Switch ON pin 11
57        GPIO.output(12,False)         ## Switch ON pin 12
58        GPIO.output(13,True)          ## Switch OFF pin 13
59        time.sleep(speed)             ## Wait
60        print "ACW step"              ## Print current loop
61        GPIO.output(11,False)         ## Switch ON pin 11
62        GPIO.output(12,True)          ## Switch ON pin 12
63        GPIO.output(13,True)          ## Switch OFF pin 13
64        time.sleep(speed)             ## Wait
65        print "ACW step"              ## Print current loop
66        GPIO.output(11,False)         ## Switch ON pin 11
67        GPIO.output(12,True)          ## Switch ON pin 12
68        GPIO.output(13,False)         ## Switch OFF pin 13
69        time.sleep(speed)             ## Wait
70        print "ACW step"              ## Print current loop
71        GPIO.output(11,True)          ## Switch ON pin 11
72        GPIO.output(12,True)          ## Switch ON pin 12
73        GPIO.output(13,False)         ## Switch OFF pin 13
```

```
74          time.sleep(speed)              ## Wait
75          print "ACW step"               ## Print current loop
76          GPIO.output(11,True)           ## Switch ON pin 11
77          GPIO.output(12,False)          ## Switch ON pin 12
78          GPIO.output(13,False)          ## Switch OFF pin 13
79          time.sleep(speed)              ## Wait
80      if GPIO.input(16) == True:         ## Condition to clear all pins
81          GPIO.output(11,False)          ## Switch OFF pin 11
82          GPIO.output(12,False)          ## Switch OFF pin 12
83          GPIO.output(13,False)          ## Switch OFF pin 13
84          time.sleep(speed)              ## Wait
85          print "All Clear"              ## Print clear status
86      if GPIO.input(18) == True:         ## To exit from the rotation
            loop
87          GPIO.output(11,False)          ## Switch OFF pin 11
88          GPIO.output(12,False)          ## Switch OFF pin 12
89          GPIO.output(13,False)          ## Switch OFF pin 13
90          time.sleep(speed)              ## Wait
91          print "Leaving from the loop" ## Print loop leaving status
92          break                          ## Exiting from the loop
93
94  GPIO.cleanup()
```

List of publications

Journals

1. **Sanathanan S. Muttikulangara**, Maciej Baranski, George Barbastathis, and Jianmin Miao, "Wafer-level integration of replicated polymer micro-optics with micro-mechanical systems," *IEEE Photonics Technology Letters*, vol. 30, no. 23, pp. 2017-2020, 1 Dec.1, 2018.

2. **Sanathanan S. Muttikulangara**, Maciej Baranski, Shakil Rehman, Liangxing Hu, and Jianmin Miao, "MEMS tunable diffraction grating for spaceborne imaging spectroscopic applications," *Sensors* 17, no. 10 (2017): 2372.

3. Maciej Baranski, Shakil Rehman, **Sanathanan S. Muttikulangara**, George Barbastathis, and Jianmin Miao, "Computational integral field spectroscopy with diverse imaging," *JOSA A* vol. 34, no. 9 (2017): 1711-1719.

4. **Sanathanan S. Muttikulangara**, Maciej Baranski, George Barbastathis, and Jianmin Miao, "Electrostatic MEMS steppermotor actuation based rotational diffraction grating for miniaturized imaging spectroscopic applications," (*to be submitted*).

5. Maciej Baranski, **Sanathanan S. Muttikulangara**, George Barbastathis,

and Jianmin Miao, "Computational Integral Field Spectroscopy: Experimental Demostration," (*in preparation*)

Conferences

1. Maciej Baranski, **Sanathanan S. Muttikulangara**, George Barbastathis, and Jianmin Miao, "Highly crosstalked integral field spectrometer with computational inversion," *Imaging and Applied Optics Congress*, Orlando, Florida United States, June 2018.

2. **Sanathanan S. Muttikulangara**, Maciej Baranski, Shakil Rehman, Liangxing Hu and Jianmin Miao, "Diffraction grating integrated on micromachined stepper motor for diversity implementation in imaging spectroscopy," *31st IEEE International Conference on Micro Electro Mechanical Systems (IEEE MEMS)*, Belfast, Northern Ireland, January 2018.

3. **Sanathanan S. Muttikulangara**, Maciej Baranski, Shakil Rehman, Liangxing Hu, and Jianmin Miao, "Inplane rotational tuning of polymer diffraction grating for diverse imaging spectroscopy," *8th IEEE International Nano Electronics Conference (INEC): Nanoelectronics for IoT*, Kuala Lumpur, Malaysia, January 2018.

4. Maciej Baranski, **Sanathanan S. Muttikulangara**, Shakil Rehman, George Barbastathis, and Jianmin Miao, "Diversity technique in computational integral field spectroscopy," *8th IEEE International Nano Electronics Conference (INEC): Nanoelectronics for IoT*, Kuala Lumpur, Malaysia, January 2018.

5. **Sanathanan S. Muttikulangara**, Maciej Baranski, Shakil Rehman, George Barbastathis, and Jianmin Miao, "Tunable diffraction grating for imaging spectrometer," *10^{th} NAMIS International Autumn School on Micro/nano Technologies for Future Health, Environment and Sustainability*, IIS/The University of Tokyo, Japan, September 2016.

Patent

1. Maciej Baranski, **Sanathanan S. Muttikulangara**, Shakil Rehman, George Barbastathis, and Jianmin Miao, "Light field imaging dispersive spectrometer," Ref: PAT/277/16/17/SGProv.